



**EFFECTS OF BOUNDARY LAYER FLOW CONTROL USING PLASMA
ACTUATOR DISCHARGES**

THESIS

Jeffrey M. Newcamp
Lieutenant, USAF

AFIT/GAE/ENY/05-S05

**DEPARTMENT OF THE AIR FORCE
AIR UNIVERSITY**

AIR FORCE INSTITUTE OF TECHNOLOGY

Wright-Patterson Air Force Base, Ohio

APPROVED FOR PUBLIC RELEASE; DISTRIBUTION UNLIMITED

The views expressed in this thesis are those of the author and do not reflect the official policy or position of the United States Air Force, Department of Defense, or the United States Government.

AFIT/GAE/ENY/05-S05

EFFECTS OF BOUNDARY LAYER FLOW CONTROL USING PLASMA
ACTUATOR DISCHARGES

THESIS

Presented to the Faculty

Department of Aeronautics and Astronautics

Graduate School of Engineering and Management

Air Force Institute of Technology

Air University

Air Education and Training Command

In Partial Fulfillment of the Requirements for the
Degree of Master of Science in Aeronautical Engineering

Jeffrey M. Newcamp, B.S.A.E.

Lieutenant, USAF

September, 2005

APPROVED FOR PUBLIC RELEASE; DISTRIBUTION UNLIMITED.

AFIT/GAE/ENY/05-S05

EFFECTS OF BOUNDARY LAYER FLOW CONTROL USING PLASMA
ACTUATOR DISCHARGES

Jeffrey M. Newcamp, B.S.A.E.
Lieutenant, USAF

Approved:

/signed/

1 Sept 2005

Dr. Milton E. Franke
(Committee Chairman)

date

/signed/

1 Sept 2005

Dr. Mark F. Reeder
(Committee Member)

date

/signed/

1 Sept 2005

Maj Richard J. McMullan
(Committee Member)

date

Abstract

This study addresses the usage and effects of atmospheric plasma discharges on the near wall flow conditions for a Pak-B low-pressure turbine blade. A plasma actuator was built normal to the freestream flow in a low-speed wind tunnel. The test section of the wind tunnel had a contoured upper wall geometry designed to mimic the suction side of a Pak-B turbine blade. A high frequency ac voltage source supplied three voltages in the kilovolt range at four Reynolds numbers in the experiment, between 10,000 and 103,000. The effect of the plasma on the near-wall boundary layer conditions was evaluated at each of the Reynolds numbers and each of the three voltage levels. The corresponding power levels were between 15 and 25 W. Particle image velocimetry (PIV) was used to determine the 2D boundary layer characteristics of the flow. This research showed that the plasma discharges were able to dramatically increase the flow velocity near the wall; however, the plasma was unable to reattach an already detached boundary layer. Boundary layer traces were taken to validate the PIV results. Additionally, multiple manufacturing techniques were evaluated in an effort to make the electrodes more usable in turbine blade applications.

Acknowledgements

Credit is due to the many wonderful people who have made this thesis possible. Support came from many sources, and thanking them all here would be improbable, save the very largest contributors to my efforts. For thesis guidance, I thank my advisor, Dr. Milton Franke. On many occasions, I showed up in his office with questions and concerns. He granted me the freedom to discover, and a gentle guiding hand. Dr. Richard Rivir, my surrogate thesis advisor and sponsor at the Air Force Research Lab Propulsion Directorate, provided constant motivation and helped me to understand the larger scope of my project. His knowledge and experience were greatly beneficial and allowed me to understand the purpose of my research. Lastly, I give thanks to Dr. Andrew Lethander, Dr. Shichuan Ou and Dr. Isaac Boxx, who shared their lab and workspace with me during my research.

Jeffrey M. Newcamp

Table of Contents

	Page
Abstract	iv
Acknowledgements	v
Table of Contents	vi
List of Figures	viii
List of Tables	xiii
List of Symbols	xiv
List of Abbreviations	xvi
I. Introduction	1
Background	1
Objective	2
Organization	3
II. Theory	4
Boundary Layers	4
Turbine Blades	5
Dielectric Barriers	6
Plasma Discharge	7
Magnetron Sputtering Technology	11
Particle Image Velocimetry	11
III. Experimental Setup and Procedure	13
Wind Tunnel	13
Test Section	13
Electrode Manufacturing Techniques	17
Photofabrication	17
Aluminum Electrode	20
Kapton Electrode	23
Glass Electrode	27
Plasma Production	28
Measurement Apparatuses	30
Druck Pressure Transducers	30
Boundary Layer Pitot Probe	31
Type T Thermocouple	32
Instrument Calibrations	32

	Page
Particle Image Velocimetry.....	33
Experimental Procedure	35
IV. Results and Analysis.....	37
Boundary Layer Effects	37
Velocity Vectors	42
Vorticity Effects	43
Plasma Generated Vortices	48
Plasma Actuator Durability.....	50
V. Conclusions and Recommendations	53
Research Objectives	53
Research Improvements	53
Appendix A: Plasma Generation Plots	55
Appendix B: Procedure for Calibrating a Hot Film Anemometer	74
Appendix C: Boundary Layer Profiles	76
Appendix D: Velocity Vector Plots	81
Appendix E: Vorticity Contour Plots.....	97
Bibliography	105
Vita.....	107

List of Figures

<u>Figure</u>	<u>Page</u>
1. Two stage LPT arrangement.....	6
2. Plasma actuator layout	7
3. Location of quenching and ignition phases of plasma generation.....	8
4. Oscilloscope trace showing voltage and current.....	9
5. Magnified view of current discharges.....	9
6. Example of PIV image pair and resulting velocity vectors	12
7. Relative shape of the polystyrene insert	14
8. Test section setup.....	15
9. Side-view of the electrode arrangement for plasma actuators	18
10. Electrode ready for use in the experiment	20
11. Aluminum mask.....	21
12. Denton RF magnetron sputtering system.....	22
13. Aluminum mask electrode arrangement	23
14. Kapton electrode arrangement	24
15. Kapton electrode plasma discharge	26
16. Kapton electrode after failure	26
17. Completed glass electrode	28
18. Voltage and current trace using a pure resistor.....	29
19. Voltage and current trace using the plasma actuator	29
20. PIV setup.....	34
21. Boundary layer comparison for hot film and PIV at $Re = 40,000$	38
22. Boundary layer comparison for hot film and PIV at $Re = 103,000$	38

Figure	Page
23. Seven boundary layer profiles with no plasma	39
24. Seven boundary layer profiles with 15 W plasma	40
25. Plasma's influence on freestream velocity for 7.1 mm case	41
26. Plasma's influence on freestream velocity for 12.7 mm case	42
27. Velocity vectors for $Re = 10,000$ with 25 W plasma.....	43
28. Vorticity plot for $Re = 10,000$ with no plasma	45
29. Vorticity plot for $Re = 10,000$ with 15 W plasma	45
30. Magnified vorticity plot for $Re = 10,000$ with 15 W plasma	46
31. Vorticity plot with velocity vectors for $Re = 23,500$ with 15 W plasma.....	47
32. Magnified vorticity plot for $Re = 23,500$ with 15 W plasma	47
33. Vortex above top electrode for $Re = 10,000$ and 25 W plasma.....	49
34. Instantaneous vortex associated with plasma generation; magnified	49
35. Surface plot of FR4 near electrode	50
36. Arcing on an FR4 plasma actuator.....	51
37. Voltage and current plots for $Re = 10,000$ and 15 W plasma.....	56
38. Voltage and current plots for $Re = 10,000$ and 25 W plasma.....	57
39. Voltage and current plots for $Re = 23,500$ and 15 W plasma.....	58
40. Voltage and current plots for $Re = 23,500$ and 20 W plasma.....	59
41. Voltage and current plots for $Re = 23,500$ and 25 W plasma.....	60
42. Voltage and current plots for $Re = 40,000$ and 15 W plasma.....	61
43. Voltage and current plots for $Re = 40,000$ and 20 W plasma.....	62
44. Voltage and current plots for $Re = 40,000$ and 25 W plasma.....	63
45. Voltage and current plots for $Re = 103,000$ and 15 W plasma.....	64

Figure	Page
46. Voltage and current plots for $Re = 103,000$ and 20 W plasma.....	65
47. Voltage and current plots for $Re = 103,000$ and 25 W plasma.....	66
48. Power plot for $Re = 10,000$ and 15 W plasma.....	67
49. Power plot for $Re = 10,000$ and 25 W plasma.....	67
50. Power plot for $Re = 23,500$ and 15 W plasma.....	68
51. Power plot for $Re = 23,500$ and 20 W plasma.....	68
52. Power plot for $Re = 23,500$ and 25 W plasma.....	69
53. Power plot for $Re = 40,000$ and 15 W plasma.....	70
54. Power plot for $Re = 40,000$ and 20 W plasma.....	70
55. Power plot for $Re = 40,000$ and 25 W plasma.....	71
56. Power plot for $Re = 103,000$ and 15 W plasma.....	72
57. Power plot for $Re = 103,000$ and 20 W plasma.....	72
58. Power plot for $Re = 103,000$ and 25 W plasma.....	73
59. Velocity profile for $Re = 10,000$ at 7.1 mm aft of the top electrode	77
60. Velocity profile for $Re = 10,000$ at 12.2 mm aft of the top electrode	77
61. Velocity profile for $Re = 23,500$ at 7.1 mm aft of the top electrode	78
62. Velocity profile for $Re = 23,500$ at 12.7 mm aft of the top electrode	78
63. Velocity profile for $Re = 40,000$ at 7.1 mm aft of the top electrode	79
64. Velocity profile for $Re = 40,000$ at 12.7 mm aft of the top electrode	79
65. Velocity profile for $Re = 103,000$ at 7.1 mm aft of the top electrode	80
66. Velocity profile for $Re = 103,000$ at 12.7 mm aft of the top electrode	80
67. Velocity vectors for $Re = 10,000$ with no plasma	82
68. Velocity vectors for $Re = 10,000$ with no plasma	83

Figure	Page
69. Velocity vectors for $Re = 10,000$ with 25 W plasma.....	84
70. Velocity vectors for $Re = 23,500$ with no plasma	85
71. Velocity vectors for $Re = 23,500$ with 15 W plasma.....	86
72. Velocity vectors for $Re = 23,500$ with 20 W plasma.....	87
73. Velocity vectors for $Re = 23,500$ with 25 W plasma.....	88
74. Velocity vectors for $Re = 40,000$ with no plasma	89
75. Velocity vectors for $Re = 40,000$ with 15 W plasma.....	90
76. Velocity vectors for $Re = 40,000$ with 20 W plasma.....	91
77. Velocity vectors for $Re = 40,000$ with 25 W plasma.....	92
78. Velocity vectors for $Re = 103,000$ with no plasma	93
79. Velocity vectors for $Re = 103,000$ with 15 W plasma.....	94
80. Velocity vectors for $Re = 103,000$ with 20 W plasma.....	95
81. Velocity vectors for $Re = 103,000$ with 25 W plasma.....	96
82. Contour plot of vorticity for $Re = 10,000$ with no plasma	97
83. Contour plot of vorticity for $Re = 10,000$ with 15 W plasma.....	98
84. Contour plot of vorticity for $Re = 10,000$ with 25 W plasma.....	98
85. Contour plot of vorticity for $Re = 23,500$ with no plasma	99
86. Contour plot of vorticity for $Re = 23,500$ with 15 W plasma.....	99
87. Contour plot of vorticity for $Re = 23,500$ with 20 W plasma.....	100
88. Contour plot of vorticity for $Re = 23,500$ with 25 W plasma.....	100
89. Contour plot of vorticity for $Re = 40,000$ with no plasma.....	101
90. Contour plot of vorticity for $Re = 40,000$ with 15 W plasma.....	101
91. Contour plot of vorticity for $Re = 40,000$ with 20 W plasma.....	102

<u>Figure</u>	<u>Page</u>
92. Contour plot of vorticity for $Re = 40,000$ with 25 W plasma.....	102
93. Contour plot of vorticity for $Re = 103,000$ with no plasma	103
94. Contour plot of vorticity for $Re = 103,000$ with 15 W plasma.....	103
95. Contour plot of vorticity for $Re = 103,000$ with 20 W plasma.....	104
96. Contour plot of vorticity for $Re = 103,000$ with 25 W plasma.....	104

List of Tables

<u>Table</u>	<u>Page</u>
1. Test matrix	35

List of Symbols

Symbol	Page
A	area..... 6
Al_2O_3	aluminum oxide 20
BaTiO_3	barium titanate 27
C	capacitance..... 6
$(\text{CH}_3)_2\text{CO}$	acetone 21
CH_3OH	methyl alcohol..... 21
$\text{C}_3\text{H}_8\text{O}$	isopropyl alcohol..... 21
I	current 10
Na_2CO_3	sodium carbonate 19
$\text{Na}_2\text{S}_2\text{O}_8$	sodium persulfate 19
P	power..... 10
R	resistance..... 10
Re	Reynolds number 4
R_{int}	internal probe resistance 74
t	distance between plates..... 6
U	velocity..... 37
U_∞	freestream velocity..... 4
V	voltage..... 10
x	downstream distance..... 4
y	vertical distance 37
Δp	change in pressure..... 30
δ	boundary layer thickness..... 4

Symbol		Page
$\delta_{.99}$	boundary layer thickness at 99% freestream velocity.....	37
ε	permittivity of free space	6
κ	dielectric constant	6
ν	kinematic viscosity of air	4
ϕ	phase shift	10

List of Abbreviations

<u>Abbreviation</u>	<u>Page</u>
AFRL	Air Force Research Laboratory..... 13
AWG	American Wire Gauge 19
CMOS	Complementary metal oxide semiconductor 33
DBD	dielectric barrier discharge..... 9
EDM	electrical discharge machining..... 20
HF	hydrofluoric acid 21
HP	horsepower 15
LPT	low pressure turbine..... 2
Nd:YAG	neodymium-doped yttrium aluminum garnet 33
OAUGDP	one atmosphere uniform glow discharge plasma..... 10
OHR	overheat ratio 74
OR	operating resistance..... 74
PIV	particle image velocimetry..... 2
PVC	polyvinyl chloride 15
RAM	random access memory..... 33
SEM	scanning electron microscope 23
TI	turbulence intensity..... 30
UV	ultraviolet 18

EFFECTS OF BOUNDARY LAYER FLOW CONTROL USING PLASMA ACTUATOR DISCHARGES

I. Introduction

Turbine blades are critical components in all turbine engines and are, at times, a source of great inefficiency due to aerodynamic stall. The technique of adding momentum to the boundary layer of a flow system is not unique, but can be applied to turbine blades to prevent blade stall and therefore increase engine efficiency. The core focus of this research is to use non-mechanical means, or plasma, to energize the boundary layer on turbine blades – including both the mechanisms behind the plasma and the physical nature of the actuator hardware.

Background

Plasma actuators have been studied in great detail in recent years and their application to modern aerospace problems continues to develop [12]. The underlying principle involves the use of two metal electrodes with a dielectric material sandwiched in-between. The electrodes are connected to an ac voltage source, which, when high enough, ionizes the air surrounding the electrodes to produce a plasma. Many varieties of this basic design have been tested, with several producing impressive results.

Post and Corke [7] have attached plasma actuators to oscillating and stationary airfoils and successfully delayed flow separation at high angles of attack for both. McLaughlin et al. [5] have proven that plasma actuators can be effective in controlling the vortex shedding frequency behind cylinders. In doing so, the actuators can affect flow separation, and either increase or decrease flow wakes. They concluded that plasma actuators could play the same roles as more traditional flow control mechanisms. Ramakumar and Jacob [9] have run tests in this area to demonstrate plasma actuators as ailerons and winglets, as well as to reduce separation on low pressure turbine (LPT) blades. Their findings suggest that the separation control effects are three-dimensional and have dramatic influence over the downstream flow conditions.

VanDyken et al. [13] conducted a study using a NACA 0015 airfoil with a plasma actuator affixed at 7% chord. They found that there is little difference in plasma generated at frequencies between 3 kHz and 10 kHz, but peak performance occurred at a frequency of 5 kHz. Also, thicker dielectrics were found to increase the plasma's effectiveness due to their ability to "withstand higher currents and voltages before catastrophic failure" [13]. They concluded that a well-placed plasma actuator can decrease drag and increase the stall angle of an airfoil.

Objective

This research project involved multiple objectives. First, previous experimental results were to be validated and improved upon using new particle image velocimetry (PIV) equipment to achieve higher resolution images. The second objective of this research was to acquire velocity field data using a plasma actuator arranged normal to the

flow direction. Comparison of these results with those using an existing plasma actuator with electrodes 30 degrees from normal to the flow was a requirement of the research. Identifying and understanding the vortical behavior of the flow surrounding the plasma actuators was another important goal. The third core objective was to investigate new fabrication techniques for plasma actuators in an attempt to make them more durable and increase the feasibility of fabricating the actuators directly on a Pak-B turbine blade or other surface subjected to austere conditions. Various materials and manufacturing techniques were to be used in order to accomplish this objective.

Organization

This document is organized in a top-down approach. First, theory will be discussed as it applies to the experiment conducted for this research. Following this will be a description of the experimental setup and the procedures used during data acquisition. The specialized equipment such as the PIV laser and camera will be discussed. Additionally, photofabrication, sputtering technology and other methods for producing plasma actuators will be addressed. The following section will contain the results of the experiment, followed then by conclusions of the research and recommendations for future research projects of this nature. Appendices contain supplementary data such as plots and additional details for the continuation of this research.

II. Theory

In any research project, immense knowledge of the subject matter and experience with the tools to be used are critical components for success. This research involved several topic areas that came together to produce working hardware and notable results. While the study of plasma actuators and their usage for Pak-B turbine blade applications are entire topics in themselves, only the basic theory is presented herein.

Boundary Layers

Fluid flow along an airfoil or flat plate will produce a boundary layer due to the inherent viscous forces and the no-slip condition at the wall. The boundary layer will continue to grow in thickness over the surface, beginning as a laminar boundary layer, but eventually transitioning to a turbulent one. Schlichting and Gersten [11] note that the critical Reynolds number (Re) for transition to turbulence is 500,000. In wind tunnel applications, a turbulence grid can be inserted upstream of a model to influence the turbulence levels experienced downstream. Further, boundary layers will grow on a model as well as on the tunnel walls or other surfaces and can substantially alter the flow characteristics over a model. The boundary layer thickness is the height the flow has been influenced due to the presence of the wall and is shown in equation (1):

$$\delta \sim \sqrt{\frac{\nu \cdot x}{U_{\infty}}} \quad (1)$$

where ν is the kinematic viscosity of air, x is the downstream distance from the leading edge, and U_∞ is the freestream velocity. This parameter is used extensively in analyzing boundary layer profiles.

The same viscous forces that cause boundary layer growth cause a shear stress in the boundary layer. For laminar flows with increasing Reynolds number, the skin-friction coefficient decreases. Accordingly, the wall shear stress approaches zero and the flow separates [11]. Separated flow results in increased drag called pressure drag. On a turbine blade, separated flow resulting in pressure drag can be a large contribution to the total drag.

Turbine Blades

A turbine engine is comprised of multiple sets of spinning and stationary blades. From the inlet to the exhaust, a turbine engine may have the following: fan blades, low pressure compressor blades, high pressure compressor blades, high pressure turbine blades and low pressure turbine blades. Both the compressor and turbine sections contain stators and rotors. Stators remain stationary and align the flow to the correct orientation for the rotating blades. The turbine section's rotors extract work from the flow to power the compressor and the auxiliary systems. Each disk of stators and rotors is called a stage and turbine engines may have varying numbers of them. A two-stage arrangement of low pressure turbine blades is shown in Figure 1. The second and fourth blades from the left are representative of the LPTs investigated in this research.



Figure 1. Two stage LPT arrangement.

Dielectric Barriers

Dielectric strength is the ability of a material to withstand a voltage field without breaking down. Dielectrics are used in the fabrication of capacitors, whereby it is the material sandwiched between two metal plates. Generally, capacitance (C) of a material is measured by equation (2), where κ is the dielectric constant, ϵ is the permittivity of free space, A is the area of the plates and t is the separation between the plates.

$$C = \kappa \epsilon \frac{A}{t} \quad (2)$$

The dielectric constant is merely a ratio of capacitance, with the numerator being the capacitance of the material in question and the denominator being the capacitance of a vacuum without the dielectric material being present. This gives all materials a dielectric constant greater than one, since a vacuum has the smallest permittivity possible.

Plasma Discharge

Aligning electrodes on either side of a dielectric material is the underlying necessity behind the operation of the plasma actuators in this study. When plasma is discharged, this arrangement adds momentum to the boundary layer in the near vicinity of the electrodes and acts to accelerate the flow near the wall. Font and Morgan [3] found that the momentum is mostly due to “collisional momentum transfer from the ions and electrons to the neutral molecules” when the surrounding air is ionized by the high voltage ac input. A plasma actuator and an associated plasma discharge are shown in Figure 2.

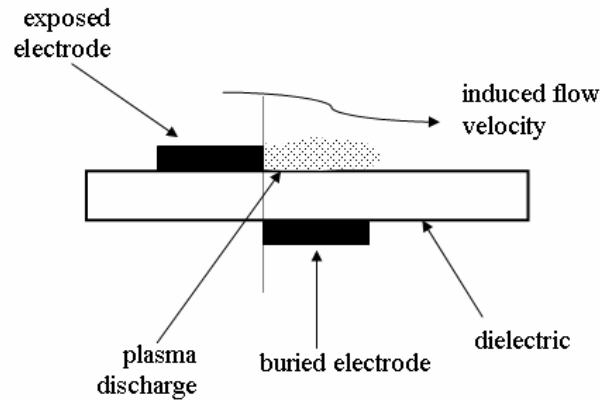


Figure 2. Plasma actuator layout.

Enloe et al. [2] discuss the structure of the plasma and show that it has two distinct phases: an ignition phase and a quenching phase. These represent the buildup of charge and consequently the quenching of the charge. Figure 3 shows what the phases look like – their signature is a disruption in the voltage of an ac cycle.

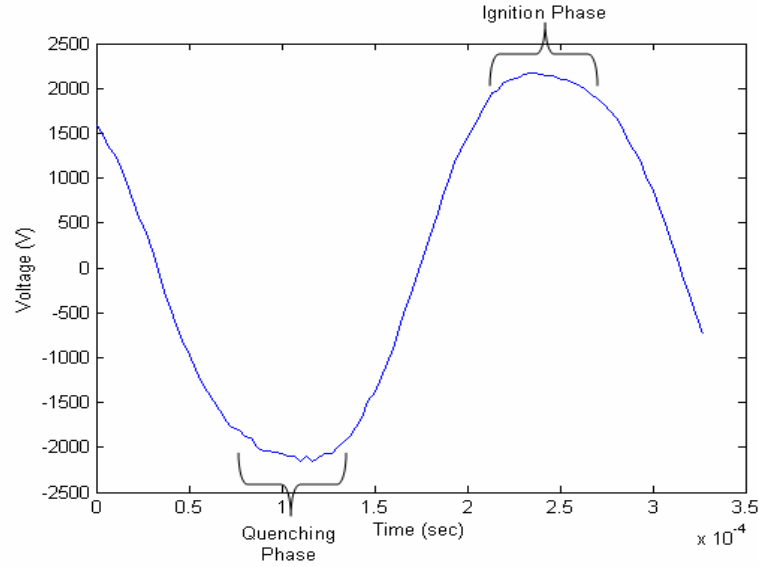


Figure 3. Location of quenching and ignition phases of plasma generation.

Another indicator of the production of plasma can be seen in an image of the voltage and current traces. Figure 4 shows two voltage and two current traces. The voltage traces are smooth, sinusoidal curves but the current traces exhibit erratic lines being emitted at the ignition and the quenching zones of the curves. These lines indicate the nature of the plasma generation. A magnified view of these regions is shown in Figure 5, where a scale has been added to indicate that peak plasma is emitted for periods of approximately 50 μ s.

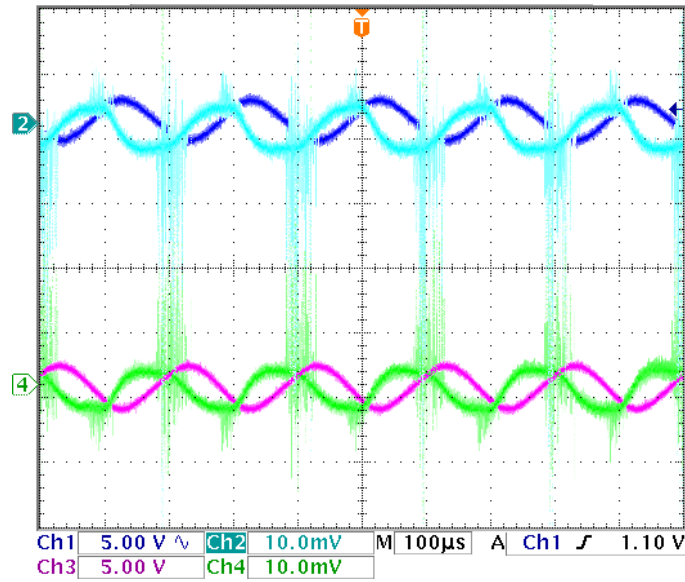


Figure 4. Oscilloscope trace showing voltage and current.

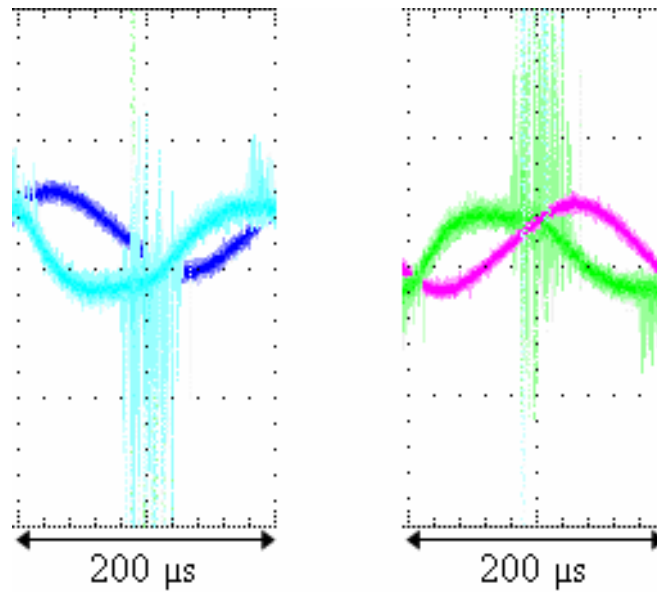


Figure 5. Magnified view of current discharges.

Enloe et al. [2] also noted that a plasma discharge is continually evolving and without a constantly changing voltage input, plasma cannot be maintained. This is a quintessential aspect of a dielectric barrier discharge (DBD). At each peak, whether high

or low, plasma is generated, therefore meaning that the existence of plasma is dependent on the slope of the voltage input. Therefore, plasma made in this form requires ac cycling, which produces the ignition and quenching phases the actuator requires to operate [2]. OAUGDP is the acronym for this phenomenon, which stands for one atmosphere uniform glow discharge plasma. It is explained in detail by Roth and Sherman [10].

The power is calculated using the known current and voltage in the ac system, as shown by equation (3):

$$P = IV \quad (3)$$

where I is the current and V is the voltage. A second equation for calculating power is shown in equation (4).

$$P = I^2 R \quad (4)$$

where R is the resistance, as calculated in equation (5). This second equation for the power could be used in conjunction with the first equation to validate results.

$$R = \frac{V}{I} (1 + \tan^2 \phi)^{\frac{1}{2}} \quad (5)$$

Here, ϕ is the phase shift, which is the radian measure of the angle between the current and the voltage [1]. Appendix A contains plots of the voltage and current as well as plots of the power for each case addressed in this research.

Magnetron Sputtering Technology

Magnetron sputtering is a technology that enables uniform deposition of materials onto virtually any substrate. It uses an evacuated chamber, which is flooded with pure argon. Disks of the deposition material, called targets, are placed into sputtering guns. While some systems consist of one gun, other systems use two guns oriented in a confocal arrangement where both guns are pointed towards the object to be sputtered. Each gun has a permanent magnet behind it and uses the resulting magnetic field to act as an electron trap in the near vicinity of the target. Meanwhile, plasma is produced on the target as a result. The argon atoms are stripped of an electron and become positively charged, which causes them to be pulled towards the target. This action results in target material being released from the target, which is then deposited onto the desired object.

Particle Image Velocimetry

PIV has several principles of operation, as outlined by Raffel et al. [8], to include seeding, illumination, image acquisition and data evaluation. For basic operation of PIV, a laser must produce two pulses of light in quick succession with a known delay in-between the pair of pulses. The laser beam must be converted to a laser sheet using a set of optics and focused on the area of interest. Then, a digital camera is positioned so that its field of view is focused at the light sheet. The camera acquires images during the pulses of laser light. Vaporized propylene glycol is used as a medium for the laser sheet to illuminate, which is then captured by the camera. A flow visualization software program then takes the images and processes each pair, as shown in Figure 6. The intensity of the particles in the first image (1) is compared to the intensity of the particles

in the second image (2). By breaking each image into many square interrogation areas, the software can compare each square from the first image to those in the second image. It shifts them in all directions to find matches. When the software finds matching light intensities, it knows that the particle moved a certain distance in a certain time (the time delay between the pulses). Therefore, speeds, velocity vectors (3) and other parameters can be obtained.

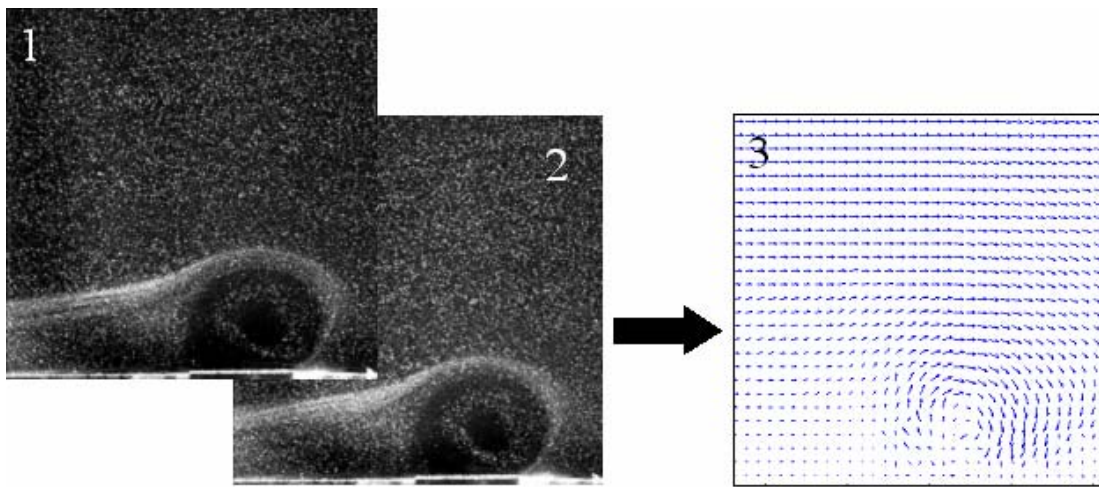


Figure 6. Example of PIV image pair and resulting velocity vectors.

One critical element of PIV involves the seed particle density. Too many particles may lead to poor correlation because the software is not able to determine where each particle moved to in the subsequent frame. Additionally, too few particles in the field of view would result in empty spots on the images, thus giving false vectors. Yet another concern is the distance traveled by the particles between the two images. If the distance is too small, the PIV software will be unable to correlate the images, and the same is true if the distance is too large. A typical distance is a 10-pixel displacement.

III. Experimental Setup and Procedure

Part of the experimental setup entailed bringing together multiple hardware systems and having each work in unison. In doing so, a great deal is learned about each system and its intricacies. This section focuses on the components that became a whole as well as the steps taken to acquire data.

Wind Tunnel

The AFRL/PRTT low-speed wind tunnel was used for this research. The wind tunnel has a compressor that feeds three separate pathways controlled by valves, but only one pathway was used in this experiment. While the tunnel is capable of much higher speeds, the velocity of this research varied between 0.5 m/s and 6 m/s. Tunnel velocity was adjusted using a control valve. Also, the main feed line was temperature controlled using a heater and chiller capable of reaching temperatures in excess of 50°C or as low as 15°C. This research was conducted at 80°F (26.6°C).

Test Section

The test section measured 36 cm wide by 23 cm tall. At the mid-height of the test section, a Plexiglas flat plate was mounted across the span of the tunnel by Balcer [1]. The flat plate had a length of 69.85 cm and a thickness of 1.27 cm. An elliptical leading edge with an aspect ratio of 4 to 1 was fabricated. Additionally, the flat plate had a 3 cm flap on the trailing edge that could be set to various angles of deflection, either positive or negative. This enabled better control over the amount of airflow that would travel over the top surface of the flat plate. A higher deflection angle resulted in more flow over the

top of the flat plate. At 12 cm behind the leading edge of the flat plate, a cavity was cut into the Plexiglas to accept the plasma actuator, with dimensions of 45 cm long and 14.5 cm wide. The plasma actuator was taped into place in the cavity.

In order to mimic the pressure distribution experienced by the suction side of a Pak-B turbine blade, Balcer [1] used a polystyrene insert to constrict the flow region above the flat plate, similar to the setup used by Hultgren and Ashpis [4], as well as Volino and Hultgren [14]. Figure 7 shows the relative shape of the insert, whereby the flow direction is left to right.

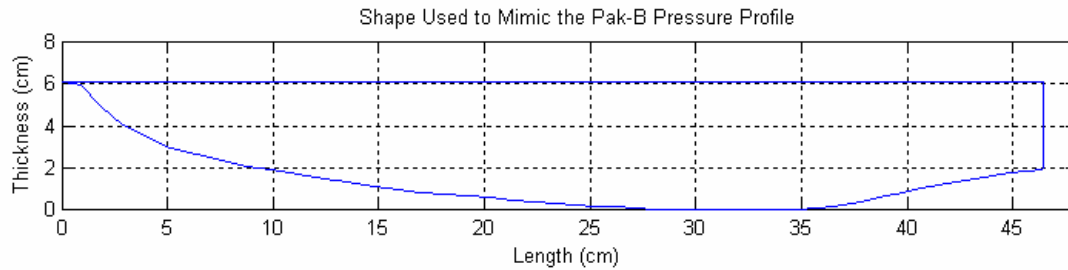


Figure 7. Relative shape of the polystyrene insert.

A 16-port pressure transducer was then used to acquire pressure readings at multiple locations along the flat plate to compare with the known pressure distribution on the suction side of a Pak-B turbine blade. The movable flap was deflected to different angles to match the Pak-B profile best. Using this setup, the flow over the flat plate experienced a freestream pressure distribution similar to that over a Pak-B blade, thus enabling a larger scale experiment and the flexibility to construct plasma actuators on circuit board material. The technology required to put a plasma actuator onto a turbine

blade however, was unavailable. For this experiment, the flap was not deflected. Figure 8 shows the flat plate, foam contour and plasma actuator.

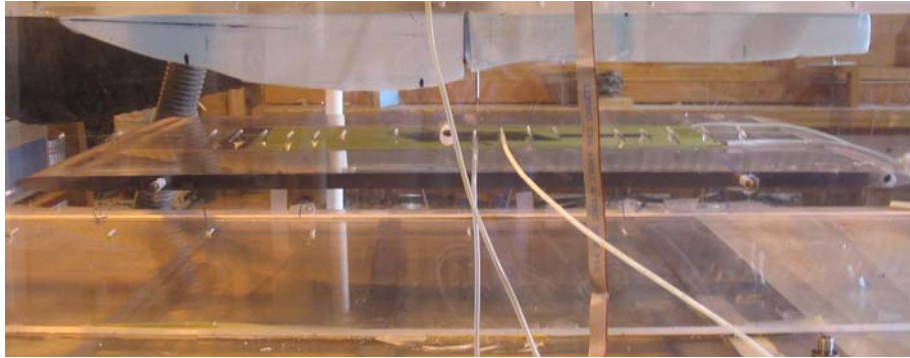


Figure 8. Test section setup.

The large contraction and then expansion of the polystyrene insert caused an area of flow separation on the top surface of the wind tunnel, downstream of the throat of the contraction. Therefore, a PVC fitting was constructed and affixed to the top of the test section and a width of the polystyrene insert was removed. This provided a channel for the suction, provided by a 2 HP vacuum, to keep the flow attached to the top surface of the test section. The level of suction applied was controlled using a butterfly valve. The suction not only kept the top side attached, but also resulted in a flow detachment on the flat plate.

A four-inch micro traverse was mounted to the top of the wind tunnel for use in acquiring boundary layer pitot probe and hot film traces. Care was taken to position the setup at the mid-span of the test section and in a location where an attached boundary layer pitot probe would rest 10.3 mm aft of the leading edge of the top plasma-emitting electrode. Placing the pitot probe in this position served two purposes. The first was to

maintain similarity to Balcer's previous study [1] and the second reason was to prevent accidental arcing between the electrodes and probes placed at this location. A LabVIEW program controlled the vertical position of the traverse and allowed the traverse distance between data acquisition points to be adjusted along the profile.

Electrode Manufacturing Techniques

Photofabrication

The previous study by Balcer [1] used the AFRL/PRTT facilities to test the boundary layer flow control using a plasma actuator situated 30° from normal to the flow. It was decided to validate those results and compare them with a plasma actuator situated normal to the flow. Doing so required the fabrication of a new plasma actuator, having similar material characteristics as the original but with its electrodes oriented differently.

To fabricate the plasma actuator, FR4 was used. It is a double-sided copper-clad board made of woven glass cloth and epoxy-resin. The thickness of the board was 62 mil, or 1.58 mm, and had a dielectric strength of 28 V/ μm . The copper clad thickness was 1 oz/ft², or approximately 0.036 mm thick. The board was cut to 14.9 cm wide by 45.1 cm long to fit the cavity already present in the wind tunnel setup. Then, a photoresist dry film laminator was used to laminate both sides of the board with a Dupont Riston FX 900 series photoresist, 30 μm thick. The electrode fabrication took place in the AFRL/PRTT Heat Flux Instrumentation Laboratory, which is a class 10,000 clean room.

A standard drawing package was used to draw the electrode design. Because the electrodes were required to withstand 5 kV, no sharp corners or imperfections could be tolerated in the design. Even the smallest anomaly, while undetectable to the unaided eye, could cause the electricity to arc and thus, destroy the board.

An electrode 34.6 cm long and 0.32 cm wide was drawn in the shape of an “L”. The shape was then mirrored and abutted to the first. Crosshairs were placed in two

corners of the drawing for alignment purposes. When printed, the first electrode would be on the top of the board and the second would be on the underside of the board. By aligning the crosshairs, the two electrodes would be on opposite sides of the board, but offset by exactly the width of the electrodes, as shown in Figure 9.

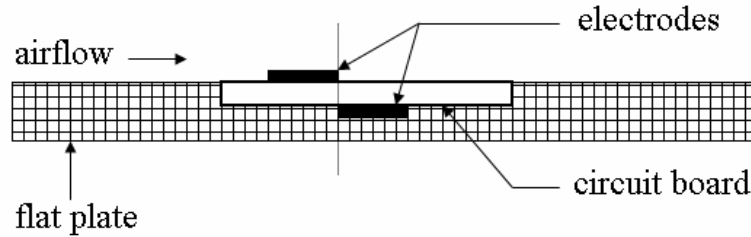


Figure 9. Side-view of the electrode arrangement for plasma actuators.

The drawings of the electrodes were then sent to a printer to be printed as high-resolution negatives on acetate paper. These masks were inspected for defects and then cleaned with isopropyl alcohol to remove fingerprints and dust particles. The FR4 board was also cleaned to ensure surface organics would not inhibit the fabrication process. The clean room's white lights and all ambient lights were turned off, leaving only the ultraviolet (UV) minimizing yellow lights.

The board was placed between the top and bottom electrode masks and the crosshairs were aligned. The orientation of each side was selected to ensure the print side of the masks would be in direct contact with the board. This prevented any shadow effects due to the thickness of the masks. Then the setup was placed on the exposure glass of a UV exposure unit containing a 3000 W metal halide bulb. First, the exposure unit created a 162 kPa vacuum seal of the chamber containing the board and masks. This ensured ideal contact between the two as well as prevented ambient light from exposing

other parts of the board. Second, the exposure glass was rotated to place the board and masks directly above the ultraviolet lamp, and then the unit exposed the mask. The board was flipped and the vacuum and exposure processes were repeated to expose the second side of the board. The UV light acted to harden the photoresist only in the areas where the masks were clear, thus leaving a protective layer in the exact shape of the electrodes. The unhardened areas could then be treated in chemical baths to remove the photoresist and copper in those locations.

In order to expose the copper on the board, the photoresist needed to be removed using a warm, 1% sodium carbonate solution (Na_2CO_3). The photoresist's protective release liner was removed from both sides of the board and then the sodium carbonate solution was poured onto the board until the photoresist was rinsed off. Then, an etching solution of 1% sodium persulfate ($\text{Na}_2\text{S}_2\text{O}_8$), commonly used in circuit board manufacturing, was prepared to etch off the unexposed copper. The etching solution was made in a 2-liter quantity and heated to 49°C for most efficient etching. The board was placed in the sodium persulfate bath and agitated to encourage contact between fresh solution and the board's surface. A small brush was also used to encourage the etching. An immersion heater was also placed in the bath to keep the sodium persulfate at an elevated temperature. When all the copper had been etched off, the board was placed in a stop bath of distilled water, and then hung to dry. A 12 mm section of photoresist at the ends of both electrodes was manually etched off to provide a location for soldering wires onto the electrodes. The 20 AWG (American Wire Gauge) wire was cut long enough to be soldered to the electrodes, fed through the tunnel's side wall and attached to the transformer. Matte black paint was airbrushed onto the circuit board in the vicinity of the

electrodes to lessen reflection from the laser pulses, which may cause image saturation in PIV images.

The dimensions of the electrodes normal to the flow direction and capable of emitting plasma were 95 mm in length and 3.2 mm in width, creating an electrode area of 302 mm². The distance between the electrodes, equal to the thickness of the circuit board, was 1.58 mm. The completed electrode is shown in Figure 10.



Figure 10. Electrode ready for use in the experiment.

Aluminum Electrode

Due to the time-intensive process of fabricating electrodes in the clean room, a more efficient method would be desirable. Therefore, it was decided to fabricate and test electrodes using aluminum as the substrate, aluminum oxide (Al₂O₃) for the dielectric and gold for the electrodes. First, a sheet of 1/8 in (0.32 cm) thick aluminum alloy 3003 was cut to 14.9 cm square to be used as a mask for depositing the electrodes. Then a drawing was made, which consisted of two electrodes running parallel, both normal to the flow direction. The parallel electrodes were 3.2 mm wide and were spaced 2 mm apart. A wire EDM (electrical discharge machining) unit used electrically energized thin

brass wire to cut the aluminum to the shape desired in the design. The mask is shown in Figure 11 and is oriented assuming a flow direction from left to right.

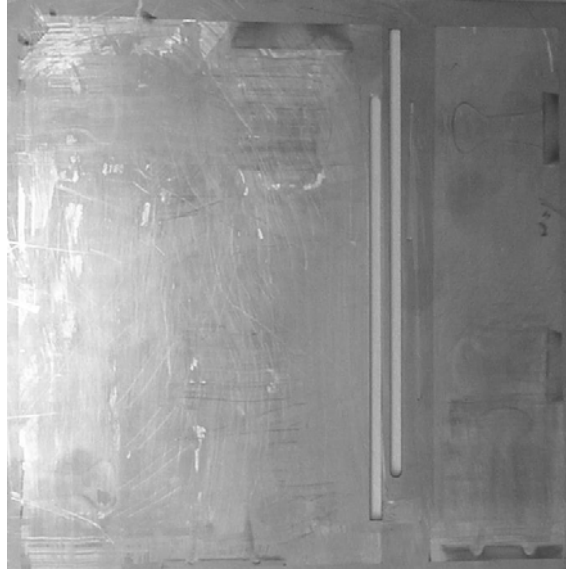


Figure 11. Aluminum mask.

With the mask completed, a 14.9 cm square of aluminum was cut to become the substrate. It was cleaned using one of two methods. The first used the series of chemicals, acetone ($(\text{CH}_3)_2\text{CO}$), methyl alcohol (CH_3OH) and isopropyl alcohol ($\text{C}_3\text{H}_8\text{O}$) to clean the surface of organics. The second method of cleaning used hydrofluoric acid (HF). Both were tested and appeared to prepare the aluminum surface equally well. Once cleaned, the aluminum was ready for its first layer of dielectric, or Al_2O_3 . It was originally thought that placing the cleaned aluminum into an oven at high temperature would encourage oxidation. However, various temperature bakes were tried and none encouraged uniform or thick oxidation. The final attempt at baking resulted in a

malformed aluminum square because the bake temperature approached the melting temperature of aluminum (660°C).

The second method for laying down a dielectric over the aluminum surface was through sputtering. Figure 12 shows the Denton RF magnetron sputtering system with its dual cathode confocal arrangement.



Figure 12. Denton RF magnetron sputtering system.

The plate was heated inside the machine and a 2/1 mixture of oxygen and argon gases was fed into the chamber to encourage oxidation of the aluminum. A small piece of aluminum, half covered by a small silicon wafer, was also put into the sputtering chamber during this procedure. It was used as a control for the thickness of dielectric on the aluminum substrate. Once the silicon piece was removed, a profilometer was used to measure the thickness of the aluminum oxide. A profilometer is a device that drags a

stylus across the surface of a material to measure any ridges and thus, can determine the thickness of a coating. After sputtering, a scanning electron microscope (SEM) was used to view the surface of the aluminum to inspect for defects. Additionally, an x-ray component of the SEM computed the elemental composition percentages of the plate. For aluminum oxide, a 3-to-2 ratio of oxygen to aluminum was desired. However, the electron microscopy revealed that manganese was present in the composition, due to impurities in the aluminum. Figure 13 shows how the completed plasma actuator was to look.

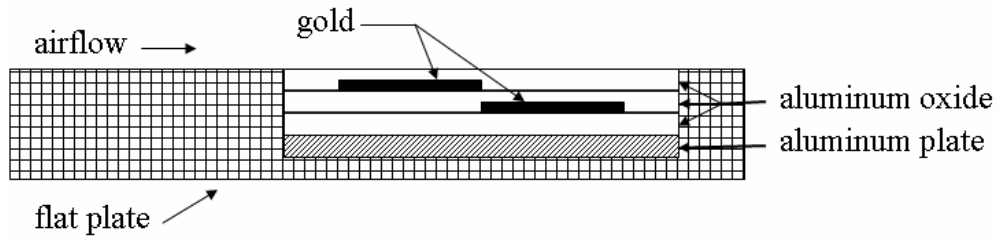


Figure 13. Aluminum mask electrode arrangement.

Because of the porous nature of aluminum, sputtering onto the surface was very inefficient and the actuator was not completed. It was too time-consuming to reach the required thickness of aluminum oxide. At the sputtering deposition rate attainable in the AFRL facilities, an actuator of the size described herein would require weeks of sputtering time – an expensive proposition. Smaller plasma actuators, however, may be feasible.

Kapton Electrode

Another fabrication technique uses Kapton film as both the substrate and the dielectric material, similar to those used by Ramakumar and Jacob [9] and Post and

Corke [6]. The dielectric strength of Kapton is 280 V/ μm . The Kapton used in this experiment, produced by 3M, was 50.8 μm thick and a piece was cut to 14.9 cm square. The aluminum mask used in the fabrication of the aluminum electrode was placed on the Kapton film to be sputtered. The Denton RF sputtering system was again used – and pure argon gas was injected into the sputtering chamber. In addition, the Kapton film was heated from underneath to foster deposition on the film. Gold was used as the sputtering metal for the electrodes because of its favorable resistance and ease of deposition.

After the top electrode was deposited, the Kapton was turned over, the aluminum mask realigned, and the bottom electrode was deposited. Each electrode was deposited to a thickness of 3 μm , which was the calculated thickness needed to carry the 25 W of power demanded by this research. Figure 14 shows the arrangement of the electrodes on the Kapton film, as situated in its position on the flat plate.

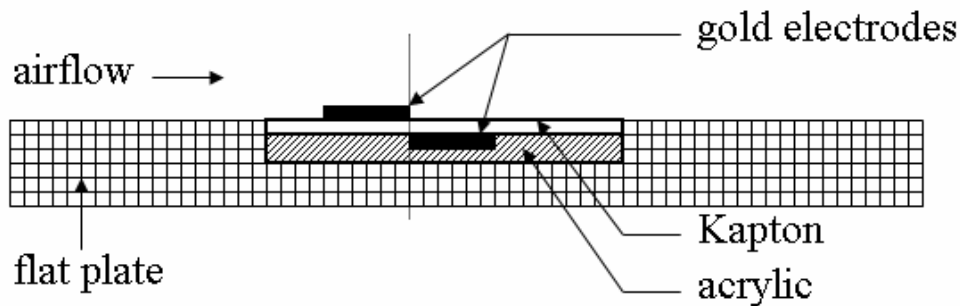


Figure 14. Kapton electrode arrangement.

Since the groove cut into the flat plate in the experimental setup was 1/16 in (0.156 cm) deep, the Kapton sheet was mounted on an acrylic piece exactly the same depth. In order to ensure proper bonding between the Kapton and acrylic, VHB adhesive

transfer tape from 3M was used. The tape was 0.05 mm thick and is made specifically for bonding in high heat environments. Two 20 AWG wires were soldered to pieces of copper tape, which were then adhered to each of the gold electrodes. This method ensured the solder points could be moved away from the plasma generating region, thus reducing the potential for arcing.

Since the Kapton electrode was fixed to a board the same width, but a smaller length than the groove in the flat plate, two filler pieces of acrylic were cut to fill the excess area in front of and behind the electrode. Using different sized pieces of acrylic, the position of the Kapton electrode on the flat plate could be varied. This gave the ability to position the plasma closer to the front or back of the Pak-B pressure distribution.

During testing, the Kapton electrode failed at a frequency of 3 kHz with an input voltage of 100 V. The failure mode was arcing from one electrode to the other, which burned the Kapton in the process. It was discovered that the dielectric strength was not great enough to withstand that needed to produce effective plasma in this study. A sequence of three images in Figure 15 illustrates the buildup of plasma and the subsequent arcing discharge. These images were taken in darkness, so the only light visible is the plasma discharge. The first image (1) shows that the plasma first discharges through the paths of least resistance. The middle image (2) shows a full discharge across the actuator, and the last image (3) shows a bright flash indicating the arcing discharge. Only a portion of the flash was captured. Figure 16 shows the failed Kapton electrode with the evidence of arcing between the electrodes at the top of the image.

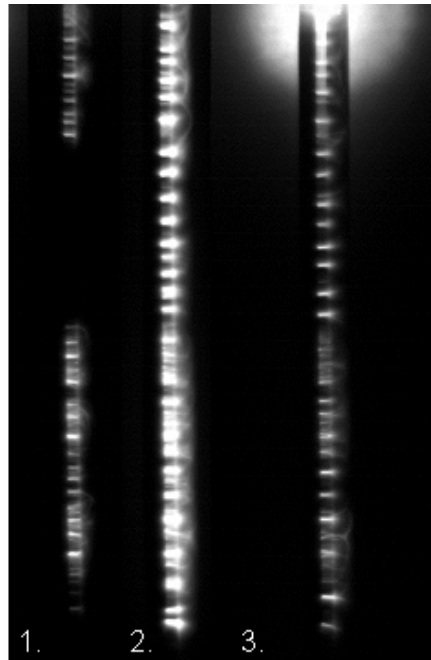


Figure 15. Kapton electrode plasma discharge.

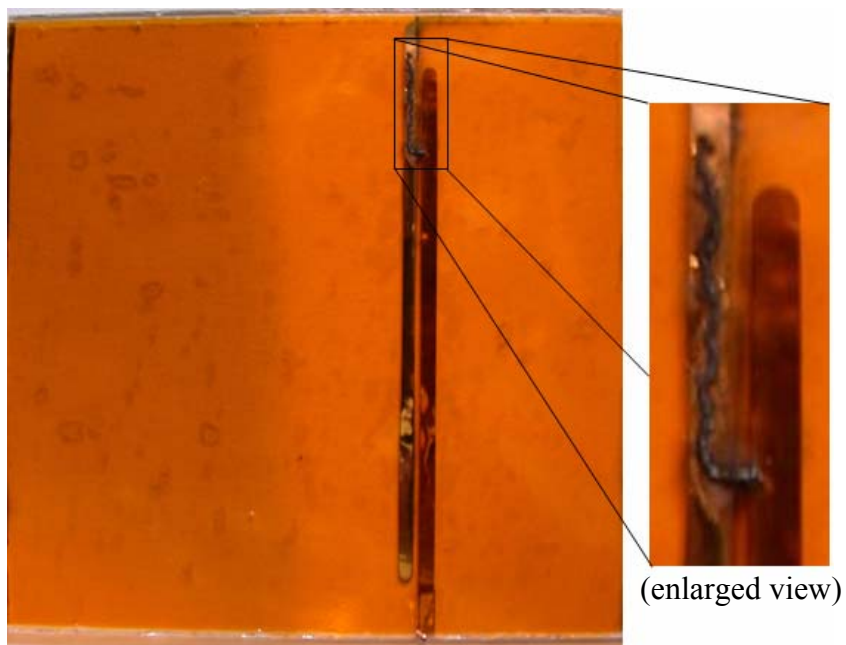


Figure 16. Kapton electrode after failure.

Glass Electrode

The photofabricated, aluminum and Kapton electrodes presented in this section are all attempts to transition plasma actuator technology to real-world turbine blades. In practice, a circuit board or sheet of Kapton would fail at the high temperatures and austere conditions in the turbine section of a jet engine. In order to make the use of plasma actuators on turbine blades feasible, materials that can withstand these conditions, such as titanium or ceramics must be used. One step closer to this goal is the use of electrodes deposited via sputtering onto optical quality borosilicate plate glass (Pyrex 7740) with a dielectric strength of $13.4 \text{ V}/\mu\text{m}$. Gold was sputtered onto 1/16 in (0.156 cm) thick plate glass using the aluminum mask detailed previously. Unlike the Kapton, however, the thickness of the glass prevented the use of both sides of the glass to deposit the electrodes. Instead, both electrodes were sputtered on the top surface of the glass, with a dielectric sputtered between them. The downstream electrode was sputtered first, directly onto the glass, to a thickness of $3 \mu\text{m}$. Then, a layer of barium titanate (BaTiO_3) was sputtered to a thickness of $3.32 \mu\text{m}$. At a deposition rate of $0.189 \mu\text{m/hr}$, this process required 17.5 hours of deposition time to obtain the thickness desired. Lastly, the second gold electrode was sputtered on the surface of the BaTiO_3 . The resulting plasma actuator was not tested for inclusion in this research, but is pictured in Figure 17. The thin film of BaTiO_3 is visible in this image due to the interference fringes.

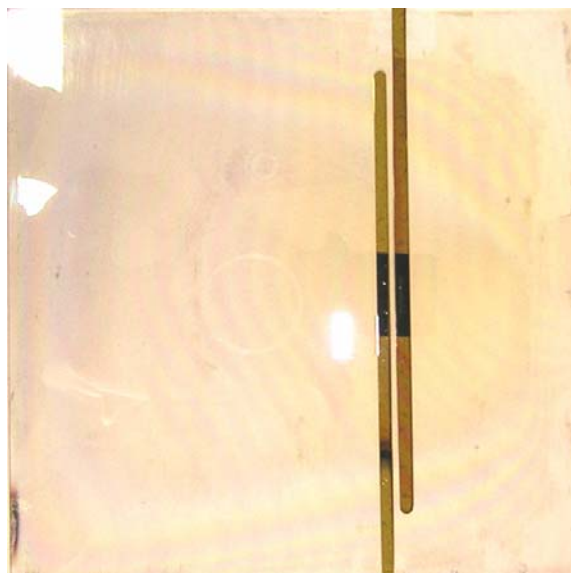


Figure 17. Completed glass electrode.

Plasma Production

The required power for the plasma discharges in this study varied from 15 to 25 W. A Titan power supply provided the necessary frequency and ac voltages required to achieve these power settings. The power supply was wired to a transformer built by the Industrial Test Equipment Company and capable of stepping up the output to a range of 6 kV to (-)6 kV. The transformer was wired directly to the plasma actuator. Two 1000X attenuator probes were hooked directly to the transformer in order to provide voltage readings to the oscilloscope. A 1000 μ H inductance coil was available to adjust the current, but it was not used during the data acquisition for the results presented herein. In order to calculate the power dissipated in the plasma actuator, the phase shift between the voltage and current applied to the electrode were calculated. This was done by applying power to a pure resistor and then applying power to the plasma actuator. The voltage and current were directly in phase when the transformer was hooked up to the pure resistor,

shown in Figure 18, but the current lagged the voltage by 90° when the transformer was hooked up to the plasma actuator. This was expected, and is shown in Figure 19. The magnitude of the lag was the critical value required to compute the power per equations (4) and (5). Appendix A shows voltage and current plots for each of the cases in this study.

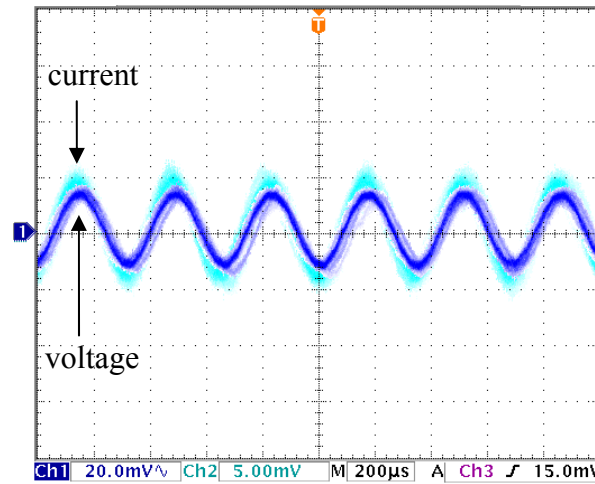


Figure 18. Voltage and current trace using a pure resistor.

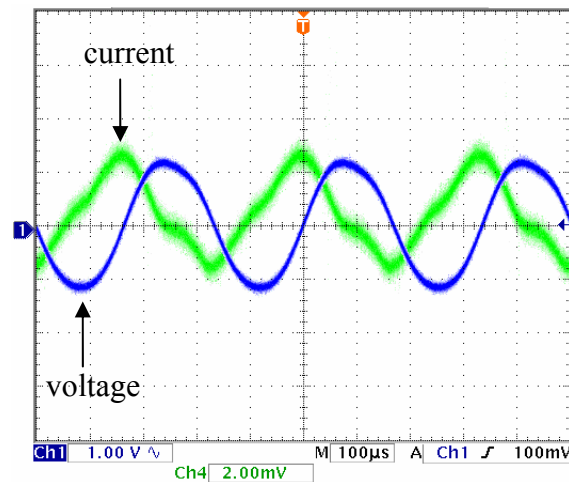


Figure 19. Voltage and current trace using the plasma actuator.

Measurement Apparatuses

Calibration and setup of the measuring devices was an important aspect to this study. When dealing with boundary layer sizes of 0.75 cm, two methods of measuring the effects of plasma were used for validation purposes. The first was PIV and the second was boundary layer probes, both pitot probes and hot films.

Druck Pressure Transducers

Two differential pressure transducers (series LPM 9000 GE-Druck) were used, one having a range of 0 – 0.2 inches of water and the other 0 – 0.8 inches of water. Both had a non-linearity of $\pm 0.1\%$. The first transducer ran using 16 – 30V DC, while the second ran using 10 – 30 V DC. Their power was supplied using two power supplies (Hewlett-Packard), both set to 20 V DC. The first transducer provided an output of 0 – 10 V DC and the second provided 0 – 5 V DC. At the set temperature for the experiment, 26.6°C, the range of the transducers was 0 – 10 m/s and 0 – 20 m/s, respectively. These values were computed using equation (6), where Δp is in inches of water and velocity is in feet per second. For the higher Reynolds number cases, the 0 – 0.8 inches of water transducer was used.

$$Velocity(fps) = 68.12\sqrt{\Delta p(inH_2O)} \quad (6)$$

The turbulence intensity, or TI, was calculated at the location of the electrodes using a hot film anemometer. Care was taken to align the film perpendicular to the flow to accurately measure the oncoming flow. The TI was used as an aid to characterize the

flow. Using a turbulence grid inserted upstream of the flat plate, the TI could have been increased. Procedures for calibrating the hot film are outlined in Appendix B.

Boundary Layer Pitot Probe

The pitot probe used for the boundary layer traces was connected to the total pressure side of a pressure transducer using rubber tubing. A static port on the side of the wind tunnel test section at the downstream location matching the pitot probe was connected to the static pressure side of the transducer. The transducer was connected to the data acquisition system and provided an output voltage corresponding to the differential pressure. A LabVIEW program was set to acquire this data. It took 1200 scans per second to eliminate any extraneous noise from the fluorescent lighting in the test cell given off at those frequencies. Data were taken for a length of 180 seconds for each scan, giving a total of 216,000 values to average for each scan location. Such long data sets were taken due to the $\pm 0.1\%$ output voltage drift inherent to the transducers. A full three minutes of data allowed for the averaging of the drift, since that amount of time is more than 2.5 times the period of the drift. The LabVIEW program provided data files listing the vertical location of the traverse, the velocity of the flow corresponding to the voltage output from the transducer and the root mean square for each data point. This data was used to plot boundary layer profiles.

It was found that the wind tunnel caused vibrations in the test cell strong enough to affect the transducers. Therefore, the transducers were placed in foam isolation units on a grounded optics table to distance them from the vibrations.

Type T Thermocouple

During calibration of the hot film anemometer, the temperature of the calibrator's flow jet was found to be a factor in the calibration. Therefore, a Type T thermocouple was used for measuring temperatures and was attached to the data acquisition system. Type T wire was chosen for its availability and robustness. It is good for use in mildly oxidizing environments in temperatures from 0° to 350°C, where moisture may be present. The calibrator had a port for the thermocouple midway up the flow column. This gave real-time measurements of the air temperature being used to calibrate the hot film. Additionally, a thermocouple gave the temperature of the flow inside the test section to adjust the tunnel chiller in order to run tests at uniform environmental conditions.

Instrument Calibrations

Both pressure transducers were calibrated using a dead-weight tester. The device uses a piston, an air supply and a series of known weights to produce calibration points. First, the pressure transducer is attached to the output of the dead-weight tester. Then, successively heavier weights are placed on a piston. The weight forces air through an outlet aperture, which then travels through a tube to the pressure transducer. The transducer then outputs a voltage. A calibration curve was derived from the test weights and corresponding voltages, thus giving an accurate representation of the sensitivity of the pressure transducer. The dead-weight tester used had an accuracy of 0.0004 in of water and repeatability of 0.001 in of water for the ranges tested.

A hot film calibrator air column was used to calibrate the boundary layer hot film. Various data points were taken for a range of air velocities to produce a calibration curve for the hot film. More data points were taken at low velocities because the hot film calibration curve was not linear in that regime. These calibrations were used in the data acquisition software in LabVIEW to produce accurate data output.

Particle Image Velocimetry

The PIV setup for this experiment utilized a frequency-doubled Nd:YAG laser (New Wave Solo), sheet-forming optics and camera equipment as well as a data analysis software suite. Nd:YAG is the acronym for neodymium-doped yttrium aluminum garnet. The laser emitted at a wavelength of 532 nm and was capable of a 15 Hz repetition rate at an energy of 120 mJ. The laser head was powered using a power system (New Wave). A laser light arm (Dantec Dynamics), attached to a traverse, was set up to transfer the beam into position. The traverse was set to a zero position, but could be moved out of the way to work on the test section. Sheet forming optics were used to create a light sheet, which was shone into the wind tunnel from the top through a hole cut into the polystyrene foam contour. A piece of plate glass was placed over the hole to prevent tunnel air leakage, but also to allow passage of the laser beam. Once in position, the laser sheet was focused at the mid-span location of the plasma actuator. This is the same location where the pitot and hot film traces were taken, therefore, only one form of data could be taken at a time.

A high frame-rate CMOS (complementary metal oxide semiconductor) imaging system (Photron APX) was used for image acquisition, and was outfitted with a 200 mm micro lens (Nikon AF-Nikkor). The camera had 6 gigabytes of onboard RAM for image

storage before downloading. The field of view of the camera was approximately 18 mm square and had 1024 pixels on a side. The camera was fixed to an optical table to avoid vibrations caused by the wind tunnel and was focused at the location of the laser light sheet, which was perpendicular to the electrodes. Additionally, a timing unit was used to sync the camera and the laser. Before data were taken, images of a fine ruler were taken to benchmark the camera's field of view. The data were then used in the DPIV software during image processing to give dimensioned vectors and true velocities of the flow. A fog machine (Rosco 4500) with a 1:1 mixture of propylene glycol and distilled water produced fog to seed the test section at a point far upstream of the flat plate. Figure 20 shows the PIV setup.

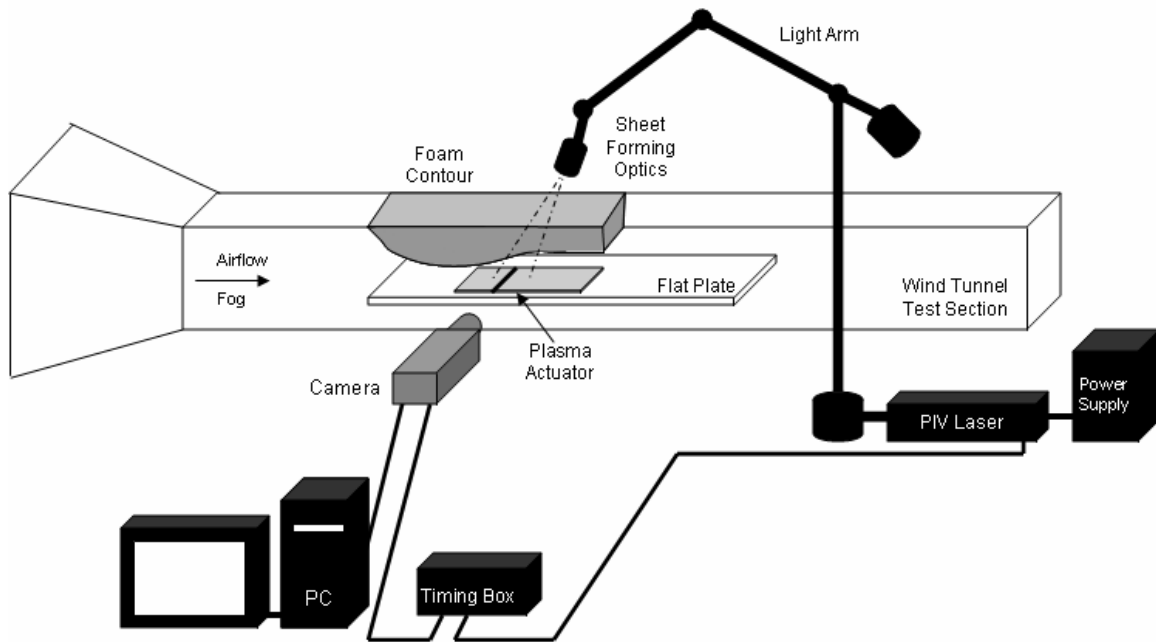


Figure 20. PIV setup.

Experimental Procedure

Table 1 shows the data collection test matrix that was completed for this experiment.

Table 1. Test matrix.

Run #	Reynolds Number	Frequency (kHz)	Voltage (V)	Power (W)	Laser Δt (μs)	Suction
1	10000	3	0	0	450	No
2	10000	3	100	15	450	No
3	10000	3	125	25	450	No
4	23500	3	0	0	150	No
5	23500	3	100	15	150	No
6	23500	3	110	20	150	No
7	23500	3	125	25	150	No
8	40000	3	0	0	80	Yes
9	40000	3	100	15	80	Yes
10	40000	3	110	20	80	Yes
11	40000	3	125	25	80	Yes
12	103000	3	0	0	30	Yes
13	103000	3	100	15	30	Yes
14	103000	3	110	20	30	Yes
15	103000	3	125	25	30	Yes

The four Reynolds numbers were chosen to examine the effects of the plasma on flow over a range of speeds. Additionally, all of the plasma was generated at a frequency of 3 kHz. This frequency was chosen to mimic that of Balcer [1]. Also, it is known that higher frequencies cause failure of FR4 boards, while much lower frequencies are unable to produce effective plasma.

Each data run began with setting the wind tunnel to the desired temperature using the chiller and verifying with a thermocouple placed in the freestream. Then, the throat velocity was measured. This was accomplished using the hot film probe and verified with a pitot probe. LabVIEW software gave real-time velocity data while the tunnel's

throttle crank was rotated. Next, the power supply was turned on and the voltage was set. The current and voltage traces were monitored on the oscilloscope and were recorded via LabVIEW for later analysis. The laser and camera were turned on and the timing was set for each flow velocity. Then, image pairs were taken and stored to disk. Depending on flow conditions, between 512 and 1024 image pairs were acquired for each run. Not all image pairs were usable, however, due to periodic seeding nonuniformity.

For cases 1-7, suction was not needed; for cases 8-15, suction was turned on to increase the boundary layer on the surface of the flat plate. It was very important, however, to follow a pattern when using the suction. If the suction was turned on before the plasma actuator, the plasma was not strong enough to reattach the flow. If the plasma actuator was turned on first, the plasma kept the flow attached even after the suction was turned on. After the image pairs were taken, the Rosco fogger was stopped, but the tunnel conditions were kept at their set points to acquire data for the other runs at the same Reynolds number.

IV. Results and Analysis

Boundary Layer Effects

One area for analysis involved using the averaged PIV data at discrete locations along the plasma actuator. Boundary layer profiles could be plotted at each location where data were acquired. The first step was to compare the PIV data to existing data acquired with hot film probes. Representative traces were taken at several Reynolds numbers with no plasma and they were compared to the PIV data at the same location and flow conditions. Figure 21 shows the results for $Re = 40,000$ and Figure 22 shows the results for $Re = 103,000$. Both plots include error bars for the dimensionless velocity component. The abscissas in Figures 21 and 22 are the normalized velocities, or the ratio of the local velocity (U) to the freestream velocity (U_∞). The ordinates are the ratio of the distance from the wall (y) to the boundary layer thickness (δ_{99}). The hot film and PIV profiles in Figures 21 and 22 show convergence far from the flat plate and reasonable convergence in the near wall region. The difference near the wall is attributed to the different forms of data acquisition, whereby the PIV lacked seed density at the wall due to the thermal effects of the plasma. Also note that the boundary layer is separated in Figure 21 due to the slow speed of the flow, but is not separated in Figure 22.

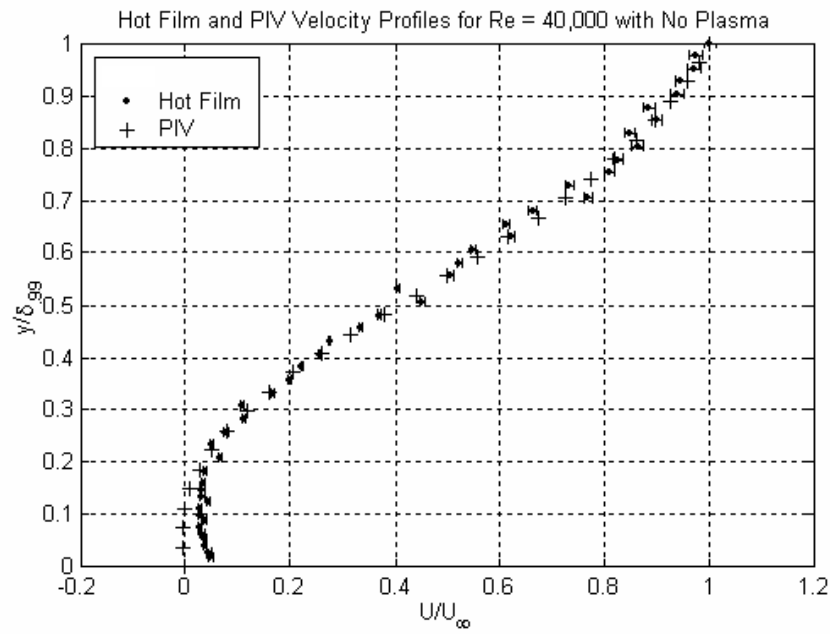


Figure 21. Boundary layer comparison for hot film and PIV at $Re = 40,000$.

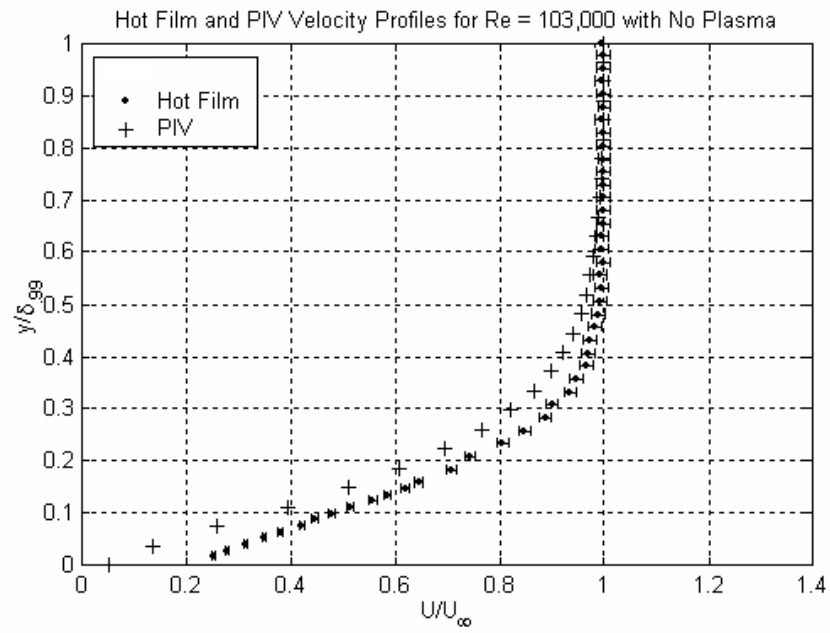


Figure 22. Boundary layer comparison for hot film and PIV at $Re = 103,000$.

Plotting multiple velocity profiles on one plot gave a general view of the effects of the plasma on the near wall flow conditions. Figure 23 shows one such plot for the $Re = 10,000$ case with no plasma. Note that no velocity scale for the profiles is present because each profile requires a unique scale, however, the profiles are dimensionless so that each is relative to the others.

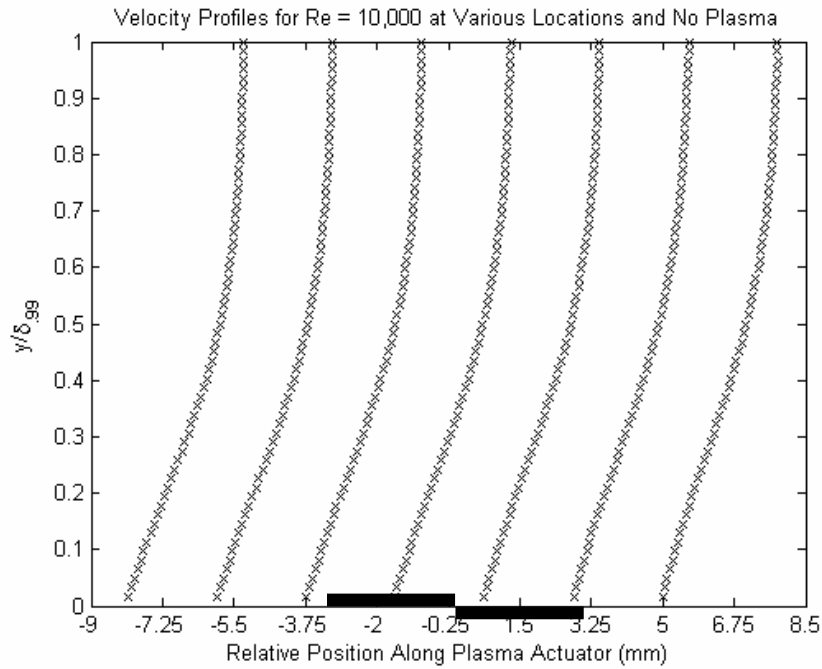


Figure 23. Seven boundary layer profiles with no plasma.

There is very little change in the boundary layer profiles from left to right, except for the slight change of the boundary layer growth with increasing downstream distance. Adding 15 W of plasma changed the profiles significantly, as shown in Figure 24. The near wall velocity is affected upstream and downstream of the electrodes with the greatest effects occurring at 7.1 mm downstream of the midpoint between the electrodes.

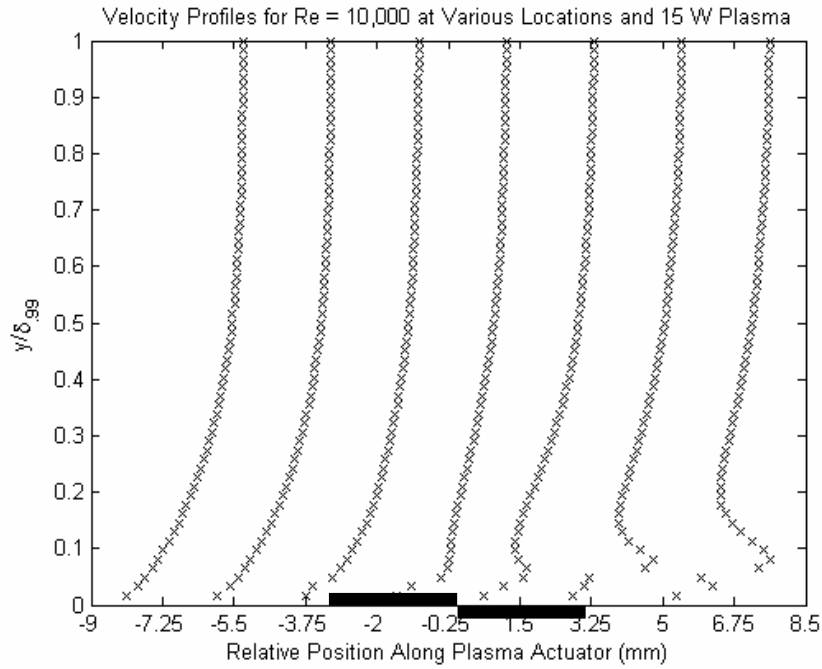


Figure 24. Seven boundary layer profiles with 15 W plasma.

It was also discovered that the plasma had an effect on the boundary layer profiles at the location 12.7 mm downstream of the midpoint between the electrodes. PIV generated boundary layer plots for both the 7.1 mm and the 12.7 mm locations are shown in Appendix C. Due to field of view restrictions, however, the $Re = 10,000$ case is plotted at 12.2 mm, not 12.7 mm.

Another phenomenon found during this research showed that the plasma actuator altered the freestream velocity aft of the actuator at all speeds. Figure 25 shows the velocity profiles for $Re = 103,000$ for four cases: no plasma, 15 W, 20 W and 25 W taken at a location 7.1 mm downstream. The freestream velocity for the no plasma case is normalized to unity. One may conclude that the cases using plasma exhibit a faster

freestream velocity due to the momentum imparted by the plasma. This is due to the local acceleration of the flow caused by the plasma. In Figure 26, the difference in the data is the location at which the profiles were recorded: 12.7 mm downstream. For example, note that the plasma no longer affects the freestream velocity and each case converges to unity at the top of the boundary layer. In Figures 25 and 26, the near wall velocities are increased with the use of plasma. For increasing the near wall boundary layer velocity, the optimum amount of power for the 7.1 mm location was 15 W. At 12.7 mm, the optimum power was 25 W. In particular, Figure 26 shows that while 25 W of power had a greater influence on the near wall velocity, the 15 W and 20 W plasma settings reduced the size of the separated region of flow. The optimum plasma power therefore depends on the desired impact, whether increased near wall velocity or reduced separation.

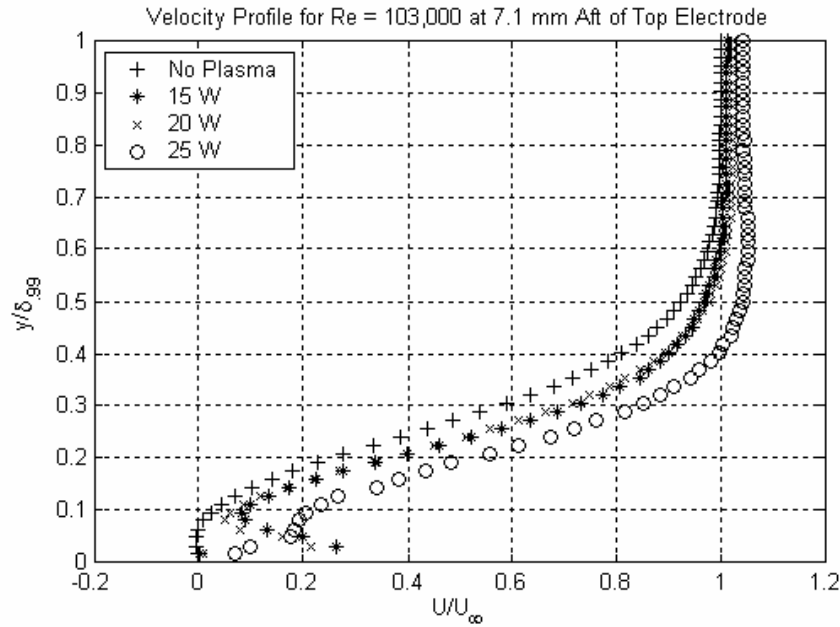


Figure 25. Plasma's influence on freestream velocity for 7.1 mm case.

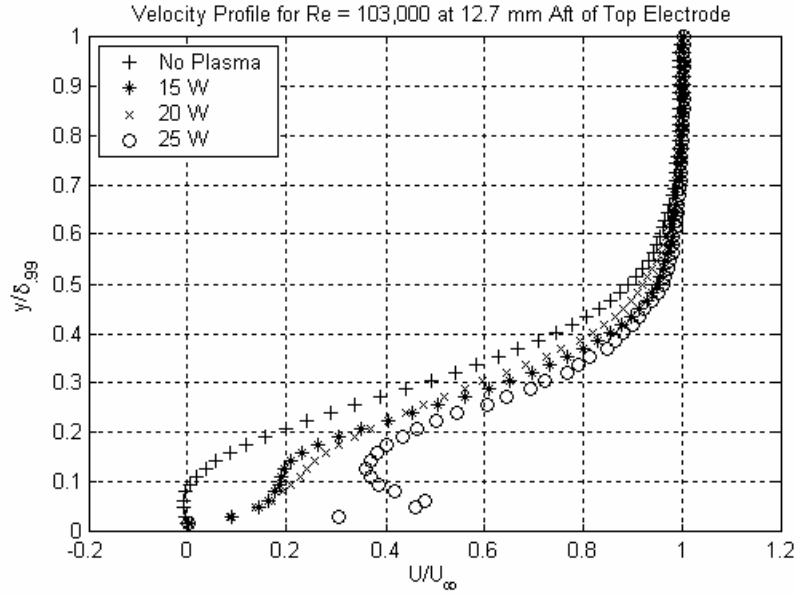


Figure 26. Plasma's influence on freestream velocity for 12.7 mm case.

Velocity Vectors

A disadvantage to the boundary layer plots was that they were confined to one location per plot. To see the larger picture, the PIV results were put into quiver plots to show the velocity vectors for the entire field of view of the digital camera. For each plot, the image pairs were averaged. Using this technique, the path of the air over the plasma actuator can be seen. The plots show that the plasma actuator accelerates the flow towards the wall and then jets it out into the boundary layer, similar to the phenomenon seen in the boundary layer traces. Since these plots were taken from averaging a large sample, the effects shown are steady. Figure 27 shows the velocity vectors for $Re = 10,000$ with 25 W of plasma. Only every third vector was plotted for clarity. The higher speed cases exhibit very similar results, but have less influence on the boundary layer.

Additionally, the plasma actuators at higher power settings had greater influence on the flow. Velocity vector plots are shown for all cases in Appendix D.

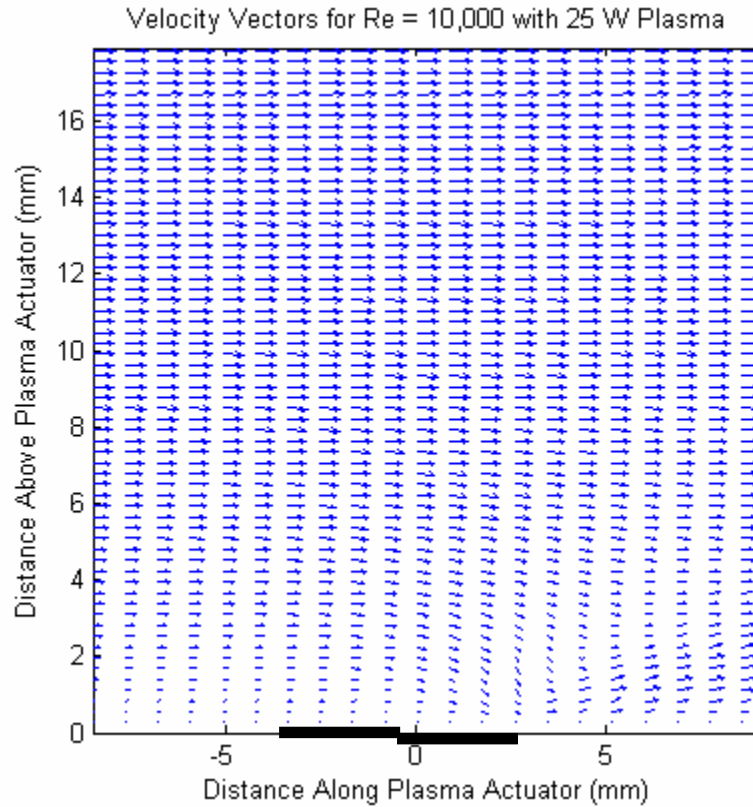


Figure 27. Velocity vectors for Re = 10,000 with 25 W plasma.

Vorticity Effects

Since plasma actuators alter the velocity of the flow near the actuator, they also alter the vorticity of the air around them. Vorticity is defined as the curl of the fluid velocity, or the degree of circulation of the fluid. Flow visualization software was used to determine this parameter and plots of vorticity in the region of the plasma actuator were produced. Each contains representative graphics of the location of the electrodes and is oriented with the flow direction from left to right. Figure 28 shows the baseline

case of vorticity as a contour plot for $Re = 10,000$ with no plasma. Figure 29 shows the same for 15 W of plasma. Figure 28 shows very little striation in the color bands used to plot the vorticity – the scale is an order of magnitude smaller than the plots shown with plasma. This was expected and validates the technique used for measuring vorticity. In Figure 29, there are several distinct features. First, a vortical structure is seen at the midpoint between the two electrodes. It is a negative color band, meaning that the flow is moving in a counterclockwise motion towards the aft electrode. The area immediately behind the aft electrode shows two sections of vorticity with opposite signs. Accordingly, the flow closer to the wall has positive vorticity and is being pushed clockwise toward the wall while the flow further from the wall has negative vorticity and is being jetted counterclockwise away from the wall. These phenomena were seen for each Reynolds number to varying degrees. Vorticity plots of each case are shown in Appendix E. For all cases studied, maximum vorticity in the flow field is increased with increasing plasma power.

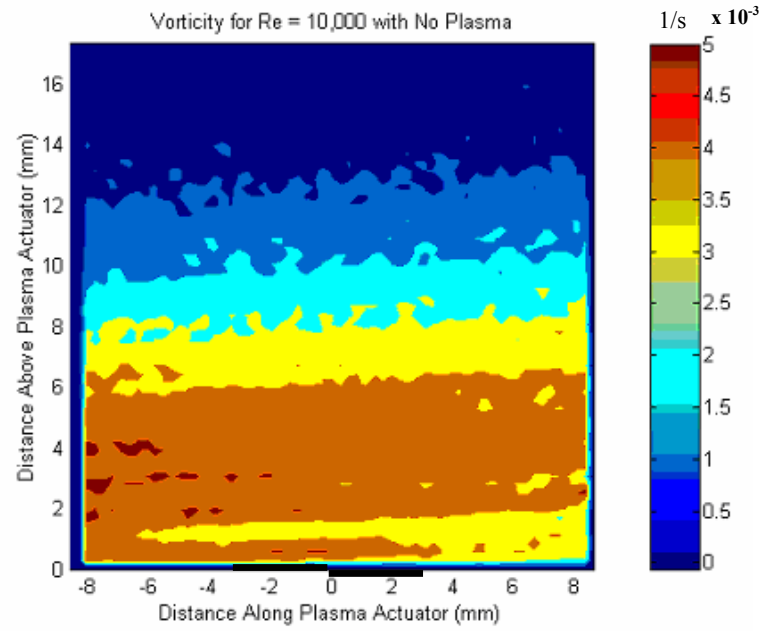


Figure 28. Vorticity plot for $Re = 10,000$ with no plasma.

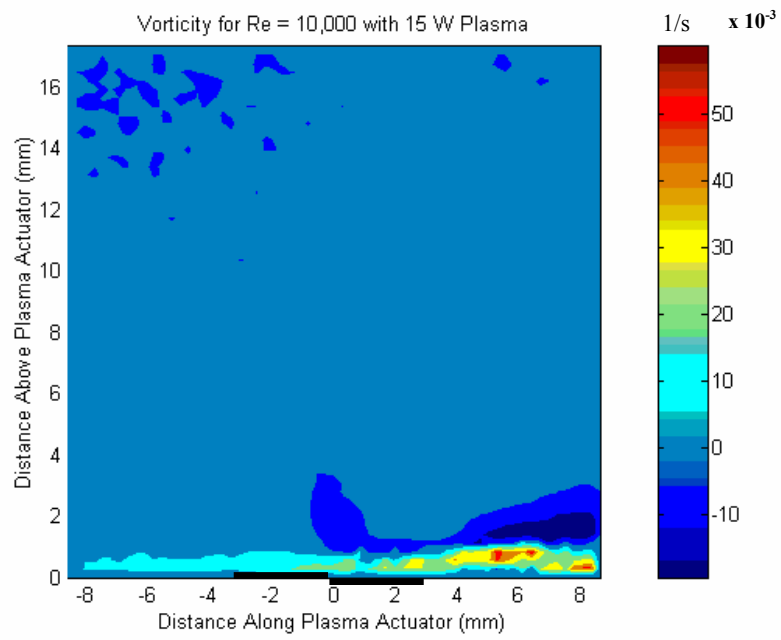


Figure 29. Vorticity plot for $Re = 10,000$ with 15 W plasma.

Figure 30 shows a magnified view of Figure 29 with velocity vectors added. This view shows better detail of the complicated vortical structures present in the flow field. Most prominently, acceleration of the flow in the direction of the aft electrode can be seen. Figures 31 and 32 show the case of $Re = 23,500$ with 15 W of plasma. Albeit a different flow speed, the same jetting and vortical acceleration can be seen. The flow is accelerated towards the wall aft of the front electrode. These flow effects occur in a small region approximately 4 mm from the wall. This region shrinks in higher speed cases and the overall vorticity increases.

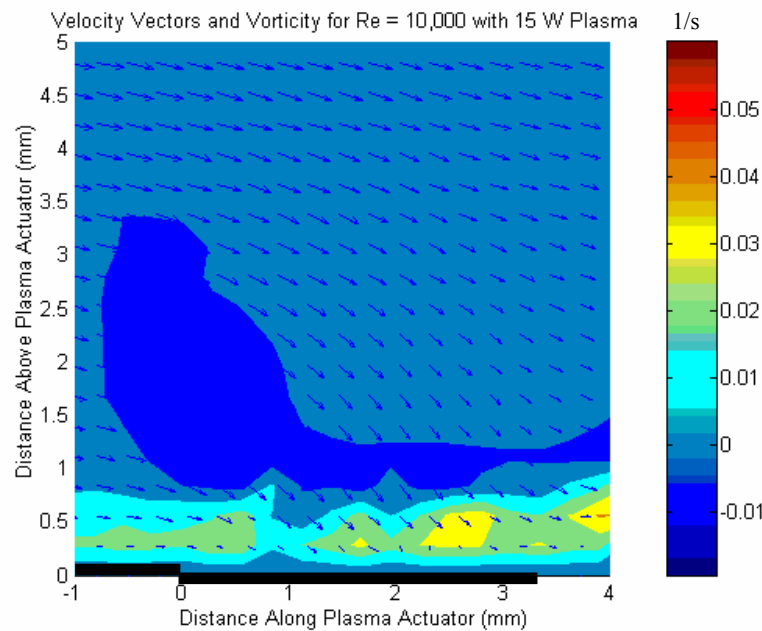


Figure 30. Magnified vorticity plot for $Re = 10,000$ with 15 W plasma.

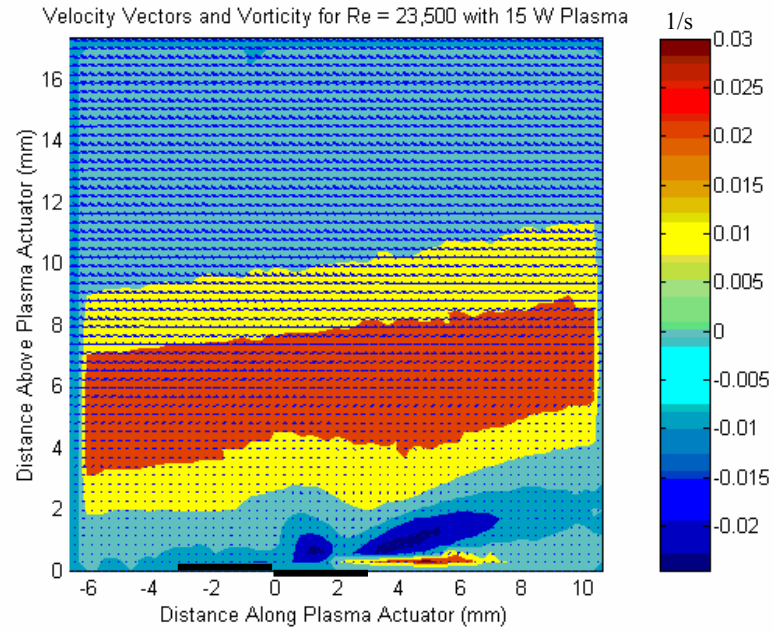


Figure 31. Vorticity plot with velocity vectors for $Re = 23,500$ with 15 W plasma.

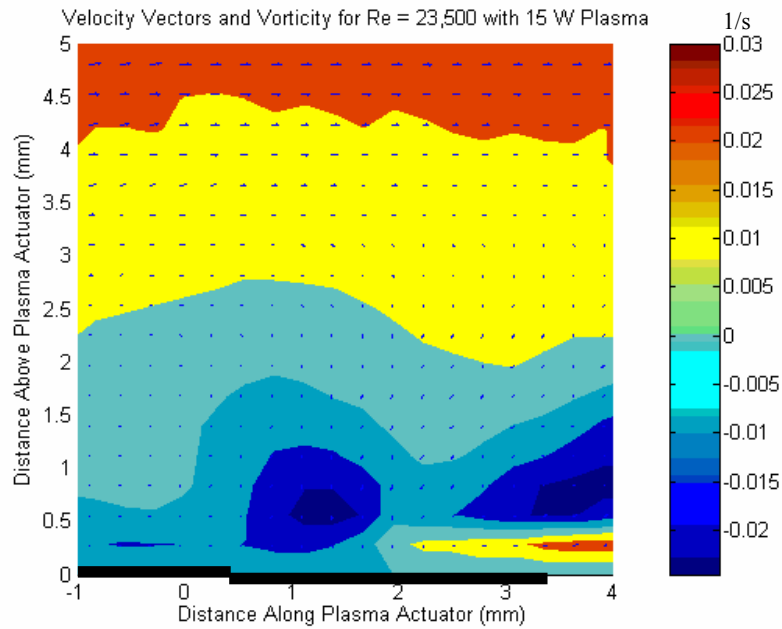


Figure 32. Magnified vorticity plot for $Re = 23,500$ with 15 W plasma.

Plasma Generated Vortices

The plasma actuator generated vortices that were seen in low speed PIV runs. This phenomenon was not seen in higher speed cases due to the inability of the plasma to significantly alter the flow conditions far from the wall. Figure 33 is a raw image from the PIV acquisition at a Reynolds number of 10,000 and a power setting of 25 W. Note the fairly prominent vortex above the top electrode. After computing the vectors for this image and its mate, Figure 34 resulted. Note that the axes have been magnified because the vortical behavior is better seen at full scale. This vortical behavior is concealed when more images are averaged, further, the occurrences were not seen to follow any readily identifiable trends. Rather, they were seen at random times during the PIV acquisition time and disappeared after several frames. Such vortices could be used, especially if shed downstream, for flow control or vortex generation applications. Unfortunately, these vortices did not propagate downstream and were of short duration.

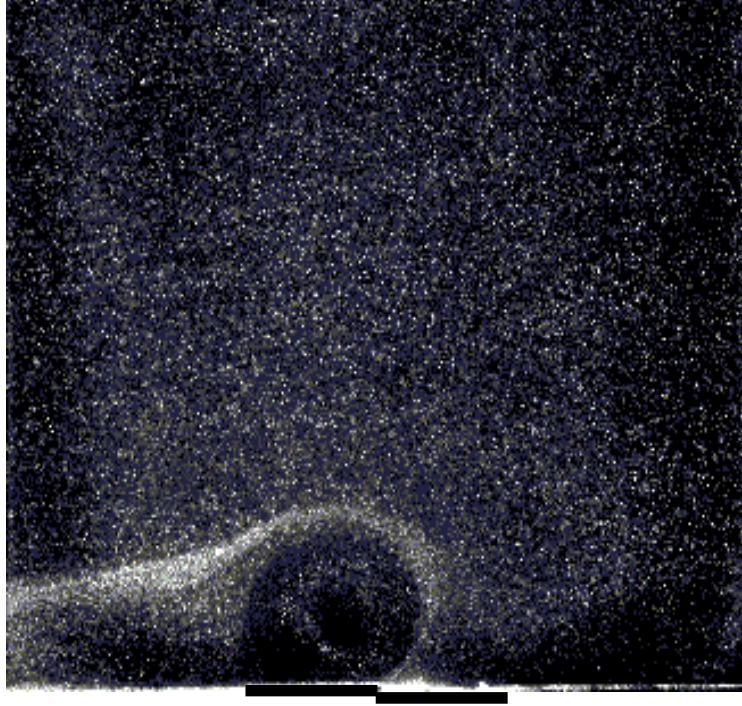


Figure 33. Vortex above top electrode for $Re = 10,000$ and 25 W plasma.

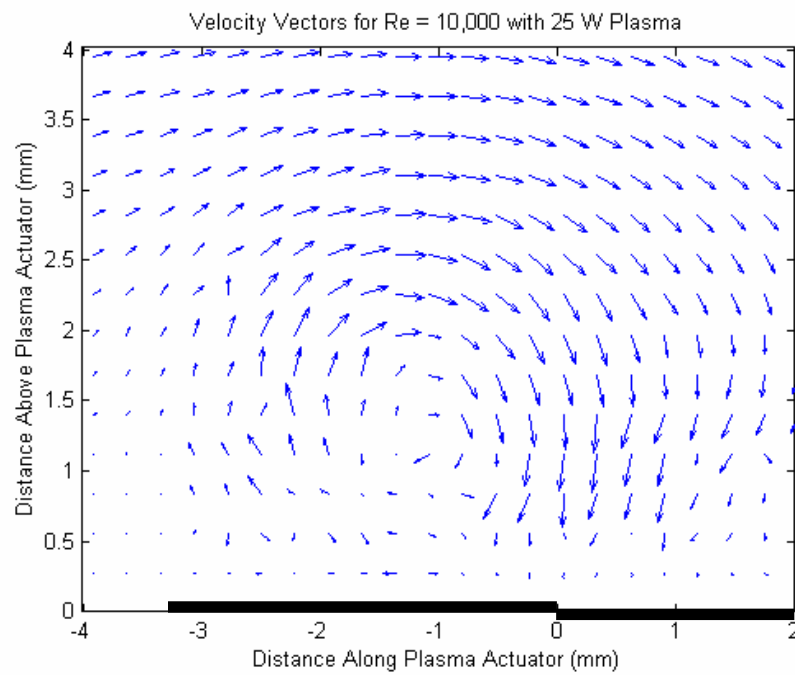


Figure 34. Instantaneous vortex associated with plasma generation; magnified.

Plasma Actuator Durability

Records were kept tracking the total usage of the FR4 plasma actuators used during this study. The objective was to understand the lifespan of the boards currently manufactured using photofabrication. The first board began to exhibit undesirable plasma emission characteristics after six hours of total plasma time. At this point, the plasma began to emit in all directions around the top electrode, indicating that the dielectric barrier had been weakened to the point where the current began traveling through the board. Additionally, scoring of the FR4 became evident around the top electrode, suggesting that the high temperature of the plasma melted the resin contained in the FR4, therefore locally thinning the circuit board. A profilometer (Taylor Hobson) trace of this phenomenon is shown in Figure 35. The top electrode can be seen as a spike in the surface height of the board, but the second electrode (downstream to the right) cannot be seen.

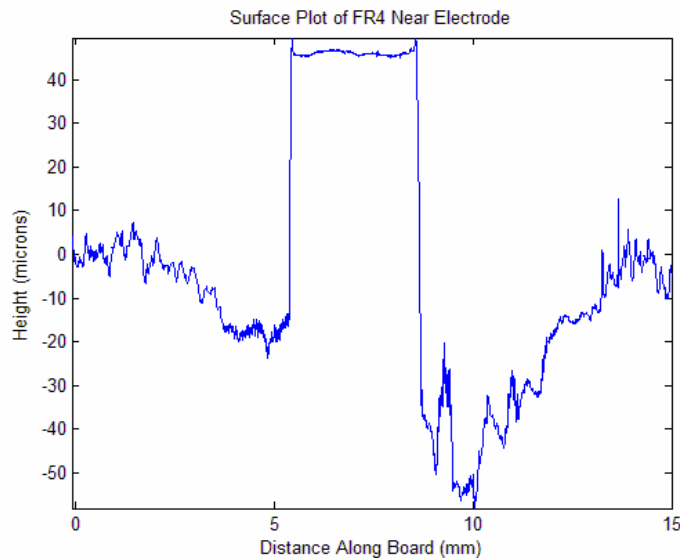


Figure 35. Surface plot of FR4 near electrode.

This profile was taken normal to the electrode, thus showing a side view with the upstream to the left. The height of the electrode above the surrounding FR4 is 45 μm , but there are two noticeable regions of roughness and pitting on either side of the electrode. Continued use of an electrode appears to weaken the FR4 and cause an arc. The current travels through the path of least resistance from the top electrode, through the circuit board and to the bottom electrode. Figure 36 shows a magnified view of a board that arced.



Figure 36. Arcing on an FR4 plasma actuator.

Also visible in this image, one can see the scoring around the edges of the top electrode. The line running left to right near the bottom of this image is a result of the ablative

nature of the laser sheet. Each pulse of the laser ablates both photoresist and the blacking, but the integrity of the FR4 and copper electrode remain unharmed. These effects are among the impetus for investigating new electrode manufacturing techniques.

On one FR4 circuit board, blacking paint was airbrushed on top of the exposed top electrode. This retarded the ability of the plasma actuator to produce plasma due to an altered dielectric strength. Therefore, blacking could only be done up to the electrodes and not over them, as shown in Figure 36.

V. Conclusions and Recommendations

Research Objectives

During the course of this research, the objectives listed in the Introduction were a constant driver. The experimental setup already in place was validated and the results shown by Balcer [1] were proven reasonable. Improvements included a larger camera lens, which provided better imaging capability. A new laser enabled greater power per pulse to be used, which required less seeding. These improvements doubled the resolution of the PIV images and vectors, allowing twice as many vectors to be computed per millimeter of the field of view.

This study showed evidence of large vortical structures present above the electrodes at low speeds as well as significant jetting of flow away from the wall aft of the electrodes. The plasma actuator, therefore, is a valuable tool in affecting the boundary layer flow conditions. It can be used to direct flow and to energize a boundary layer.

Another objective of this research was to investigate new materials and manufacturing methods for plasma actuators. It was concluded that FR4 and Kapton electrodes are sufficient, but that sputtering technology provides better substrate, dielectric and electrode options.

Research Improvements

Photofabrication is a useful technique for studying plasma actuators, but it is a labor-intensive process and has little in common with future technologies that have the

ability to produce durable electrodes. Photofabricated electrodes are incapable of being put to use on actual turbine blades. Additional effort should be invested in new manufacturing processes. One possibility is to begin with a ceramic substrate and electroplate or sputter electrodes onto its surface. This would move the actuators in the direction of being able to construct them onto actual turbine blades.

The polystyrene insert used to mimic the Pak-B pressure profile was an approximate geometry and produced satisfactory results. However, a more accurate method for matching the experimental setup's pressure distribution to that of a Pak-B blade should be sought. A machined insert firmly affixed to the wind tunnel would be a significant improvement. The experiment could be conducted in a linear cascade on actual Pak-B blades to better model flow conditions, allowing the investigation of curvature effects as well as pressure gradients. Research should also be conducted at pressures greater than sea level atmospheric conditions to investigate whether the plasma actuator has similar effects.

Appendix A: Plasma Generation Plots

For each case studied, the voltage and current for each electrode were recorded using a LabVIEW program. The electrode's wires were connected through inductance coils to obtain the current and there were voltage probes attached to the transformer to give a real-time view of the voltage going into and out of the plasma actuator. The LabVIEW program recorded the time, along with the voltage and current values, which could then be plotted. The plots show the sinusoidal nature of each component as well as the breakdown of the current trace during the plasma ignition and quenching phases. Differences in the voltage and current plots for the same power setting, but different Reynolds numbers, indicate that there is inherent variation in the plasma production due to the location of the ignition and quenching phases of the ac input. Following the voltage and current plots are power plots. Each power plot shows the power as calculated both ways described in the Theory section. The peak-to-peak amplitude of these curves is a measure of the power of the plasma actuator discharge, in watts. The two methods of power calculation show similar results, but the method using equation (3) results in greater power than equation (4) in each case.

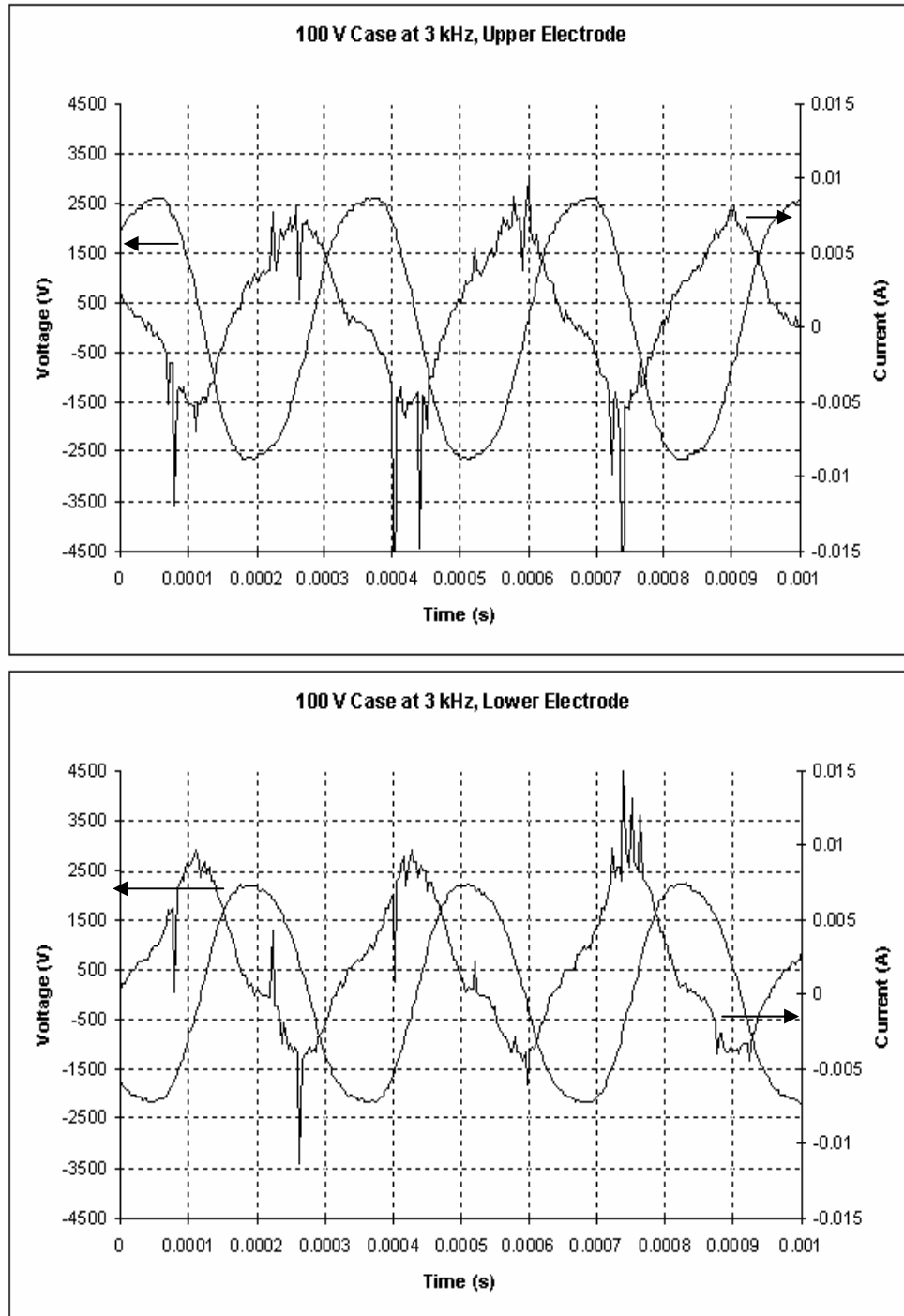


Figure 37. Voltage and current plots for $Re = 10,000$ and 15 W plasma.

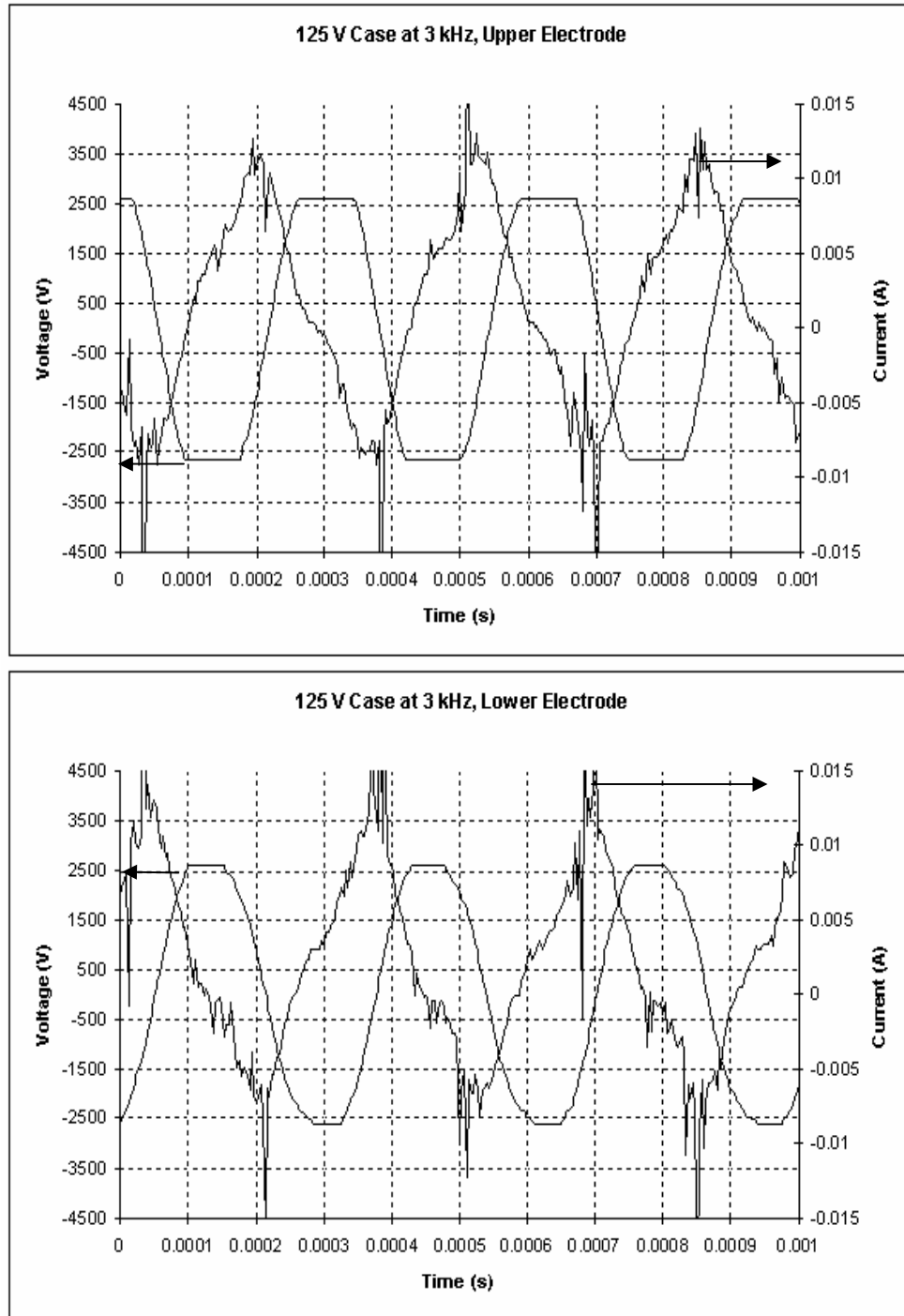


Figure 38. Voltage and current plots for $Re = 10,000$ and 25 W plasma.

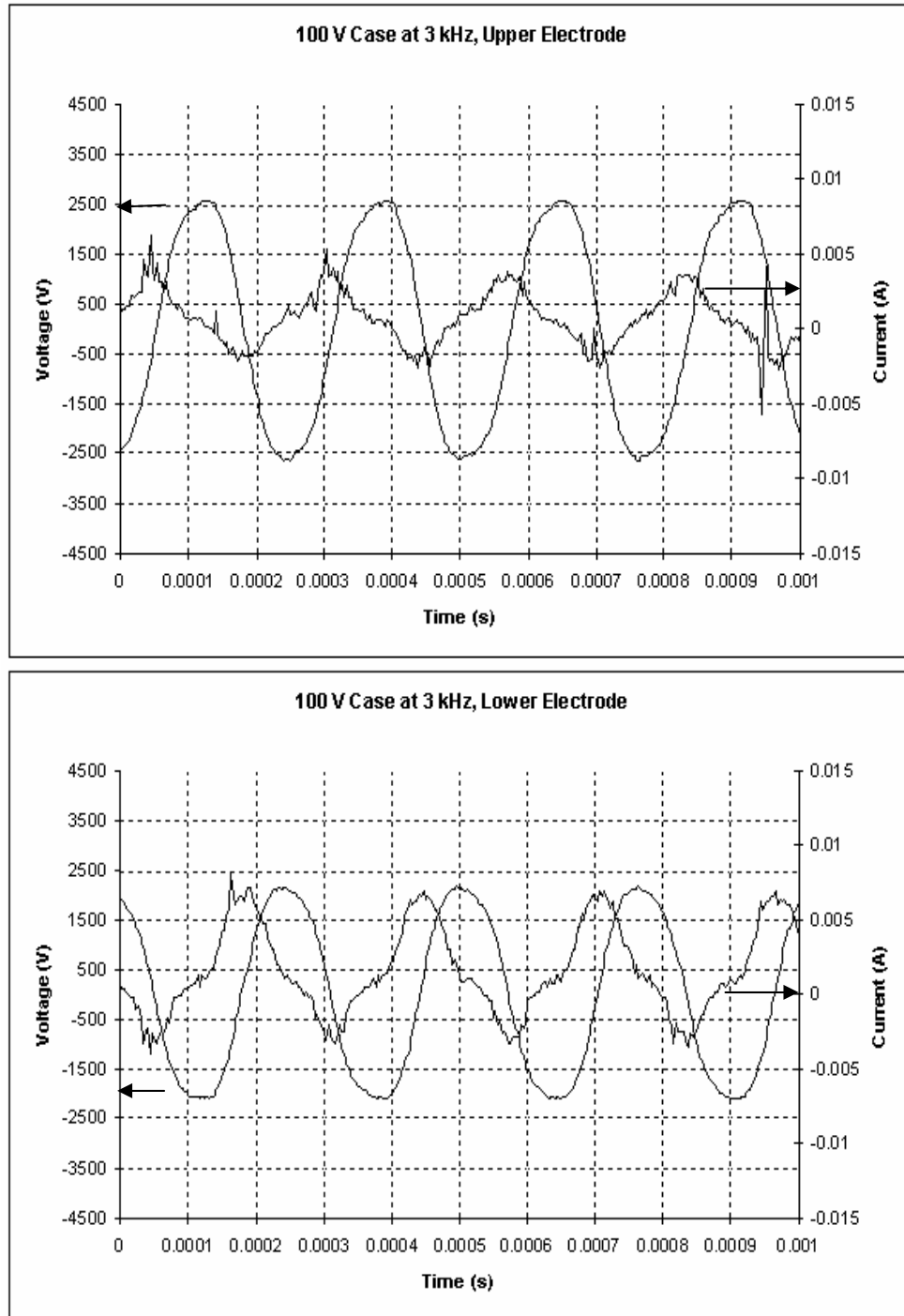


Figure 39. Voltage and current plots for $Re = 23,500$ and 15 W plasma.

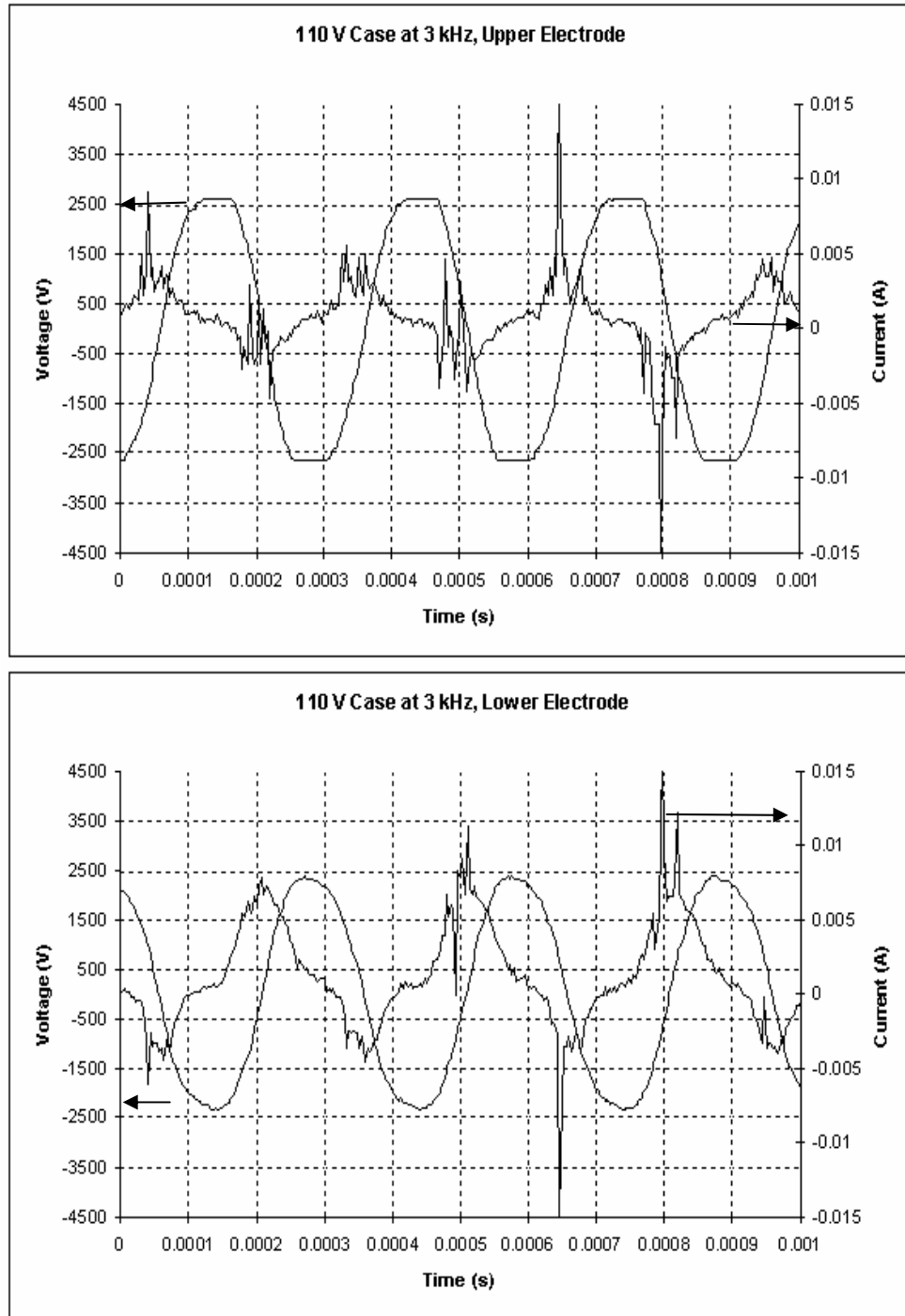


Figure 40. Voltage and current plots for $Re = 23,500$ and 20 W plasma.

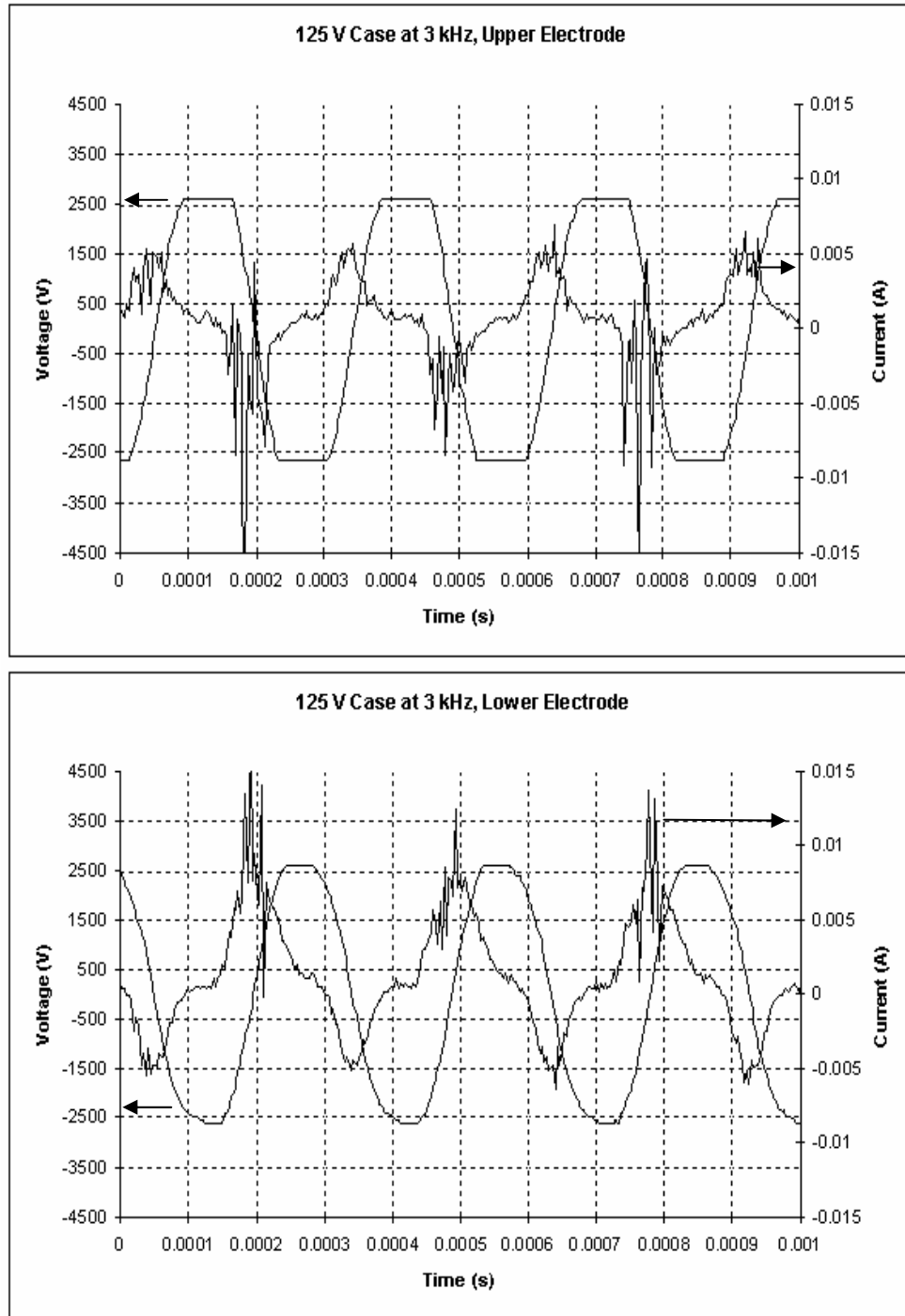


Figure 41. Voltage and current plots for $Re = 23,500$ and 25 W plasma.

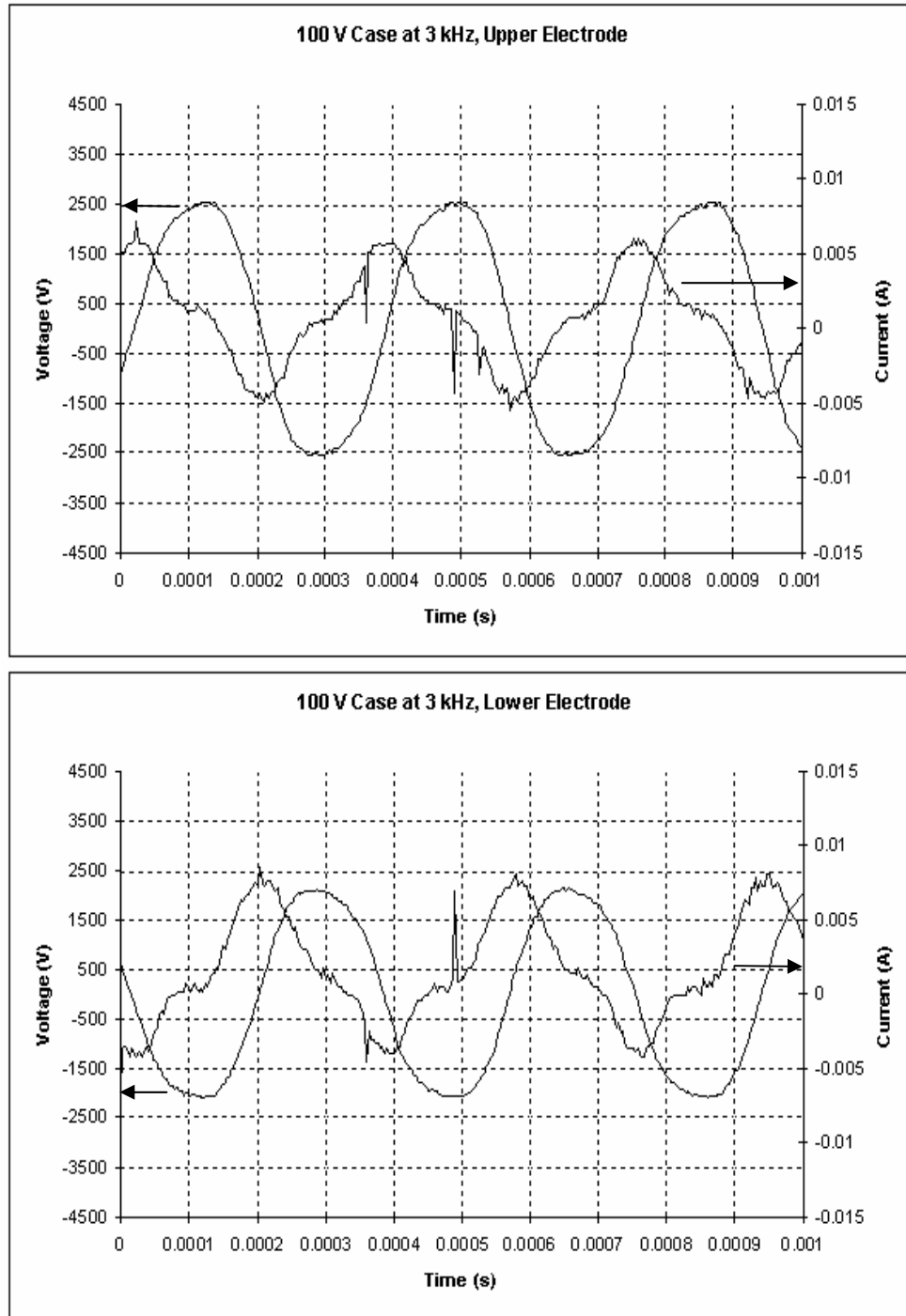


Figure 42. Voltage and current plots for $Re = 40,000$ and 15 W plasma.

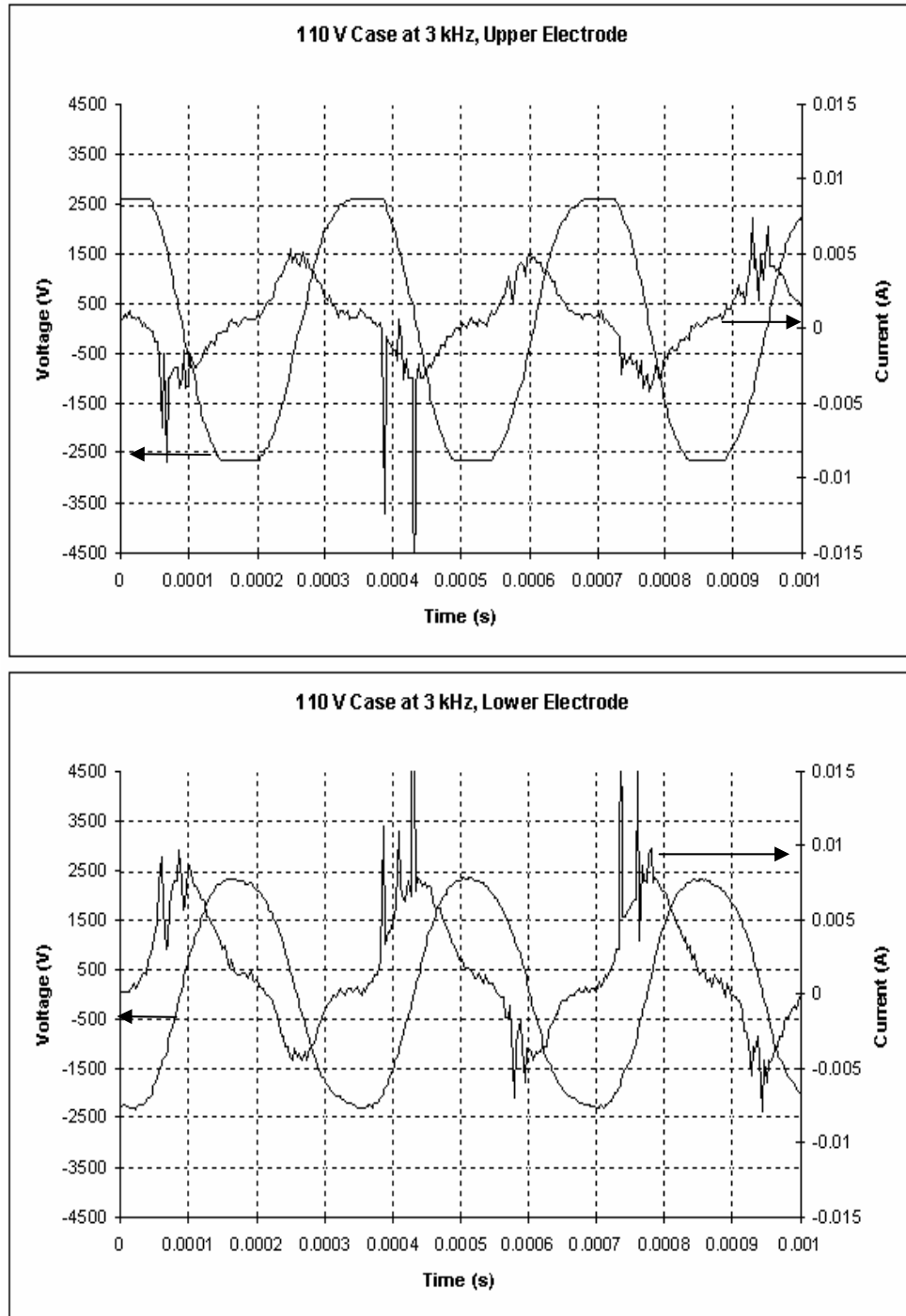


Figure 43. Voltage and current plots for $Re = 40,000$ and 20 W plasma.

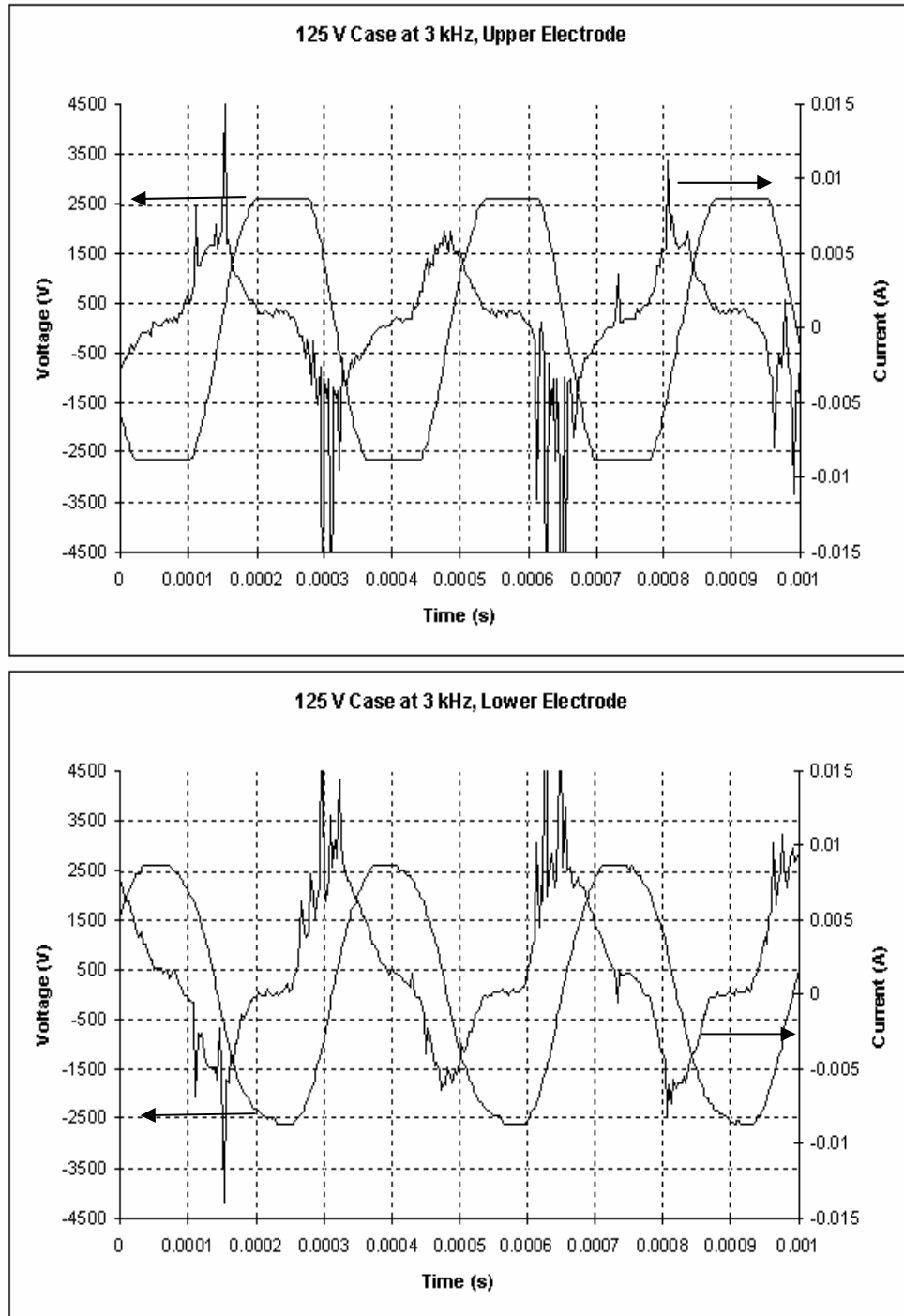


Figure 44. Voltage and current plots for $Re = 40,000$ and 25 W plasma.

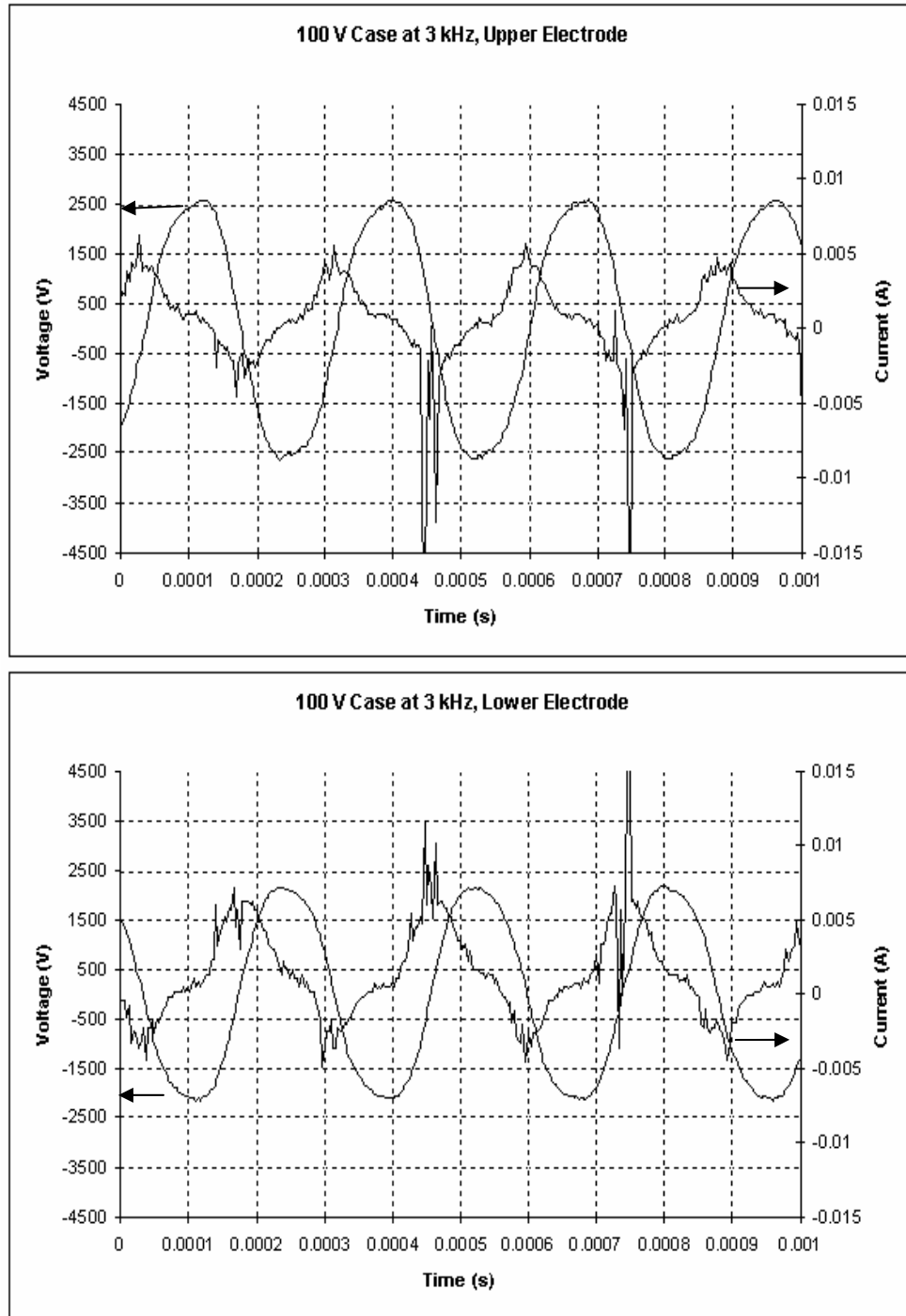


Figure 45. Voltage and current plots for $Re = 103,000$ and 15 W plasma.

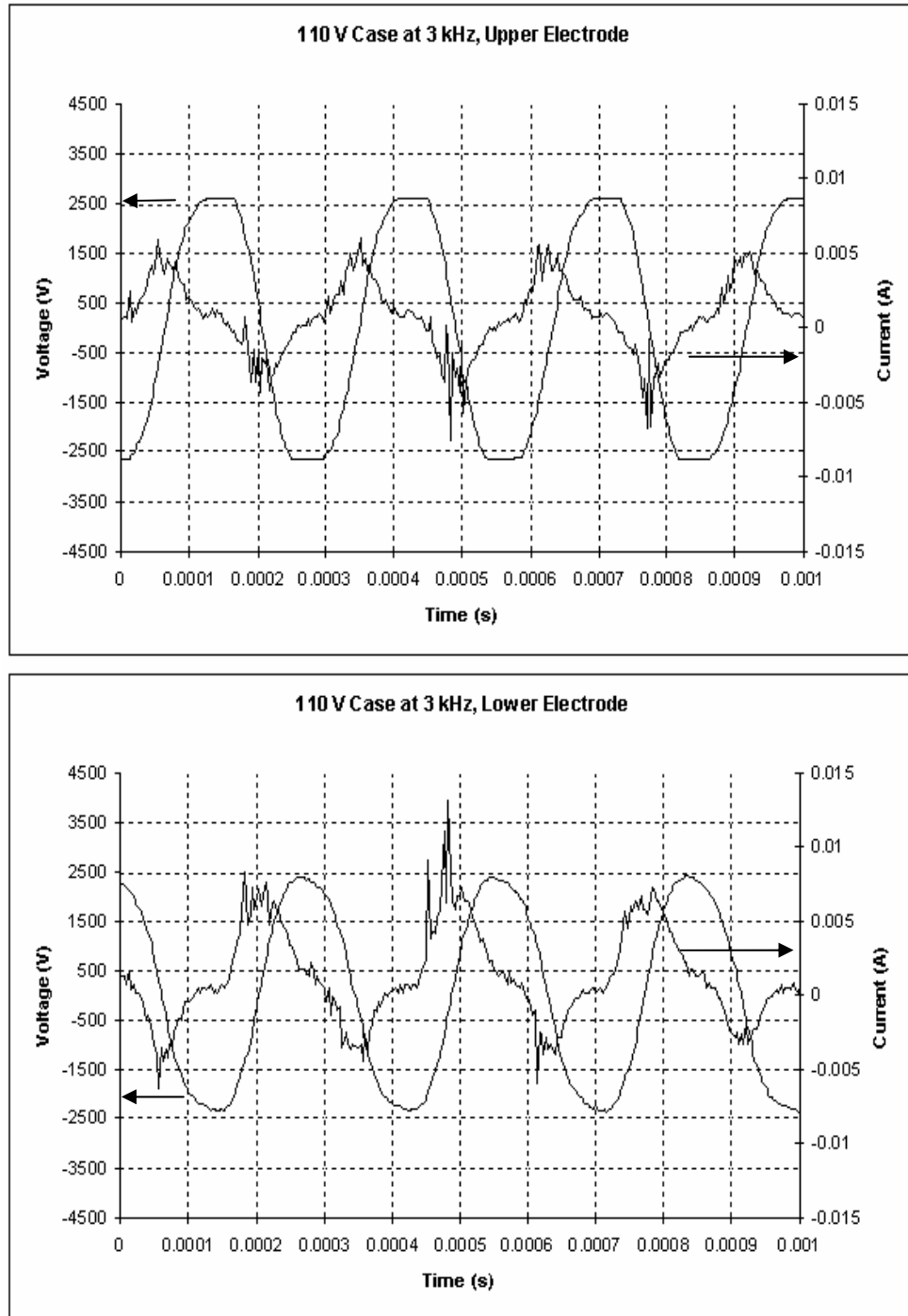


Figure 46. Voltage and current plots for $Re = 103,000$ and 20 W plasma.

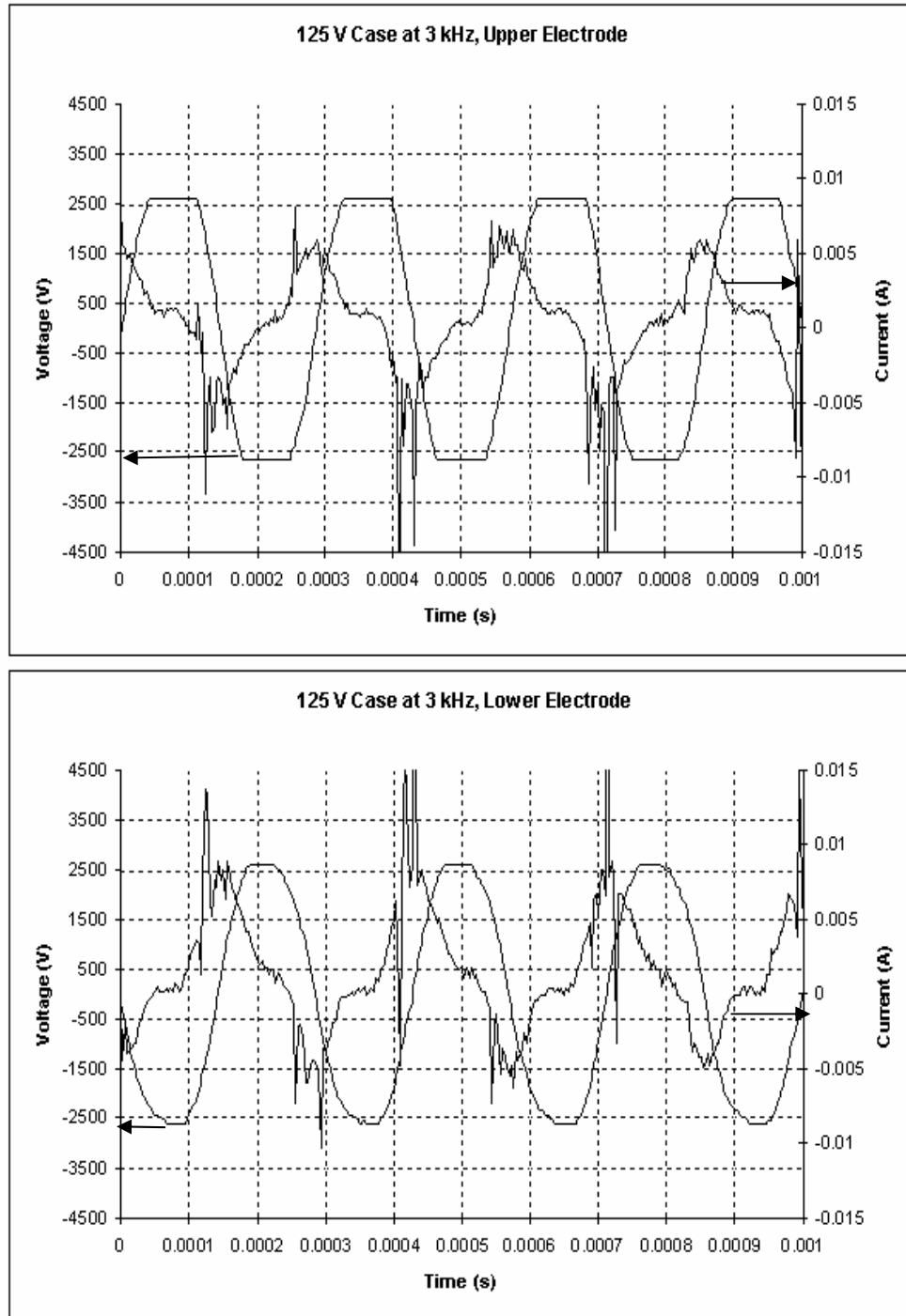


Figure 47. Voltage and current plots for $Re = 103,000$ and 25 W plasma.

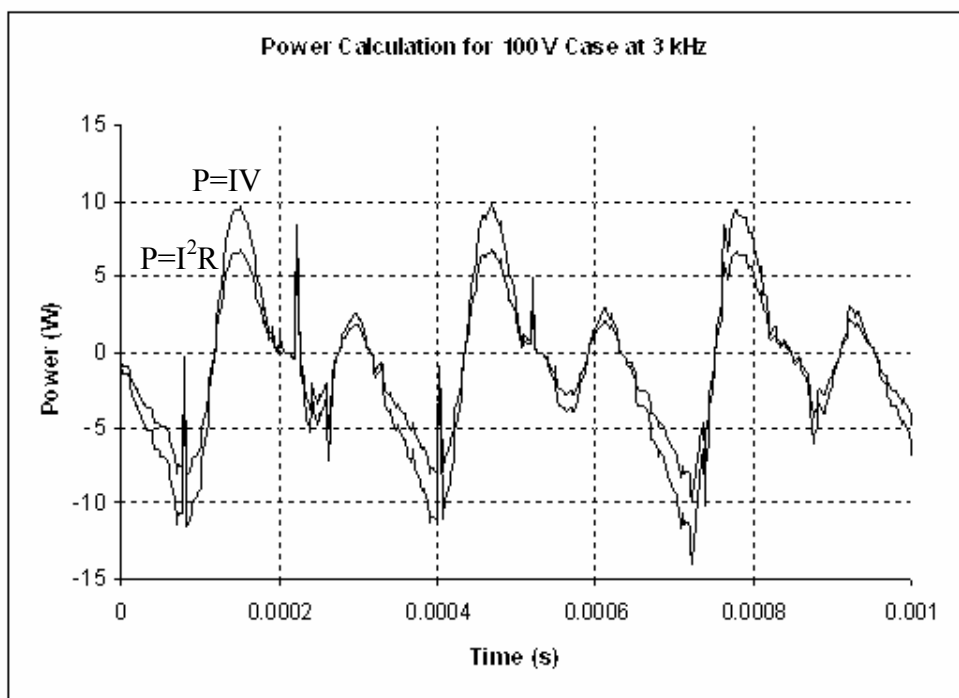


Figure 48. Power plot for $Re = 10,000$ and 15 W plasma.

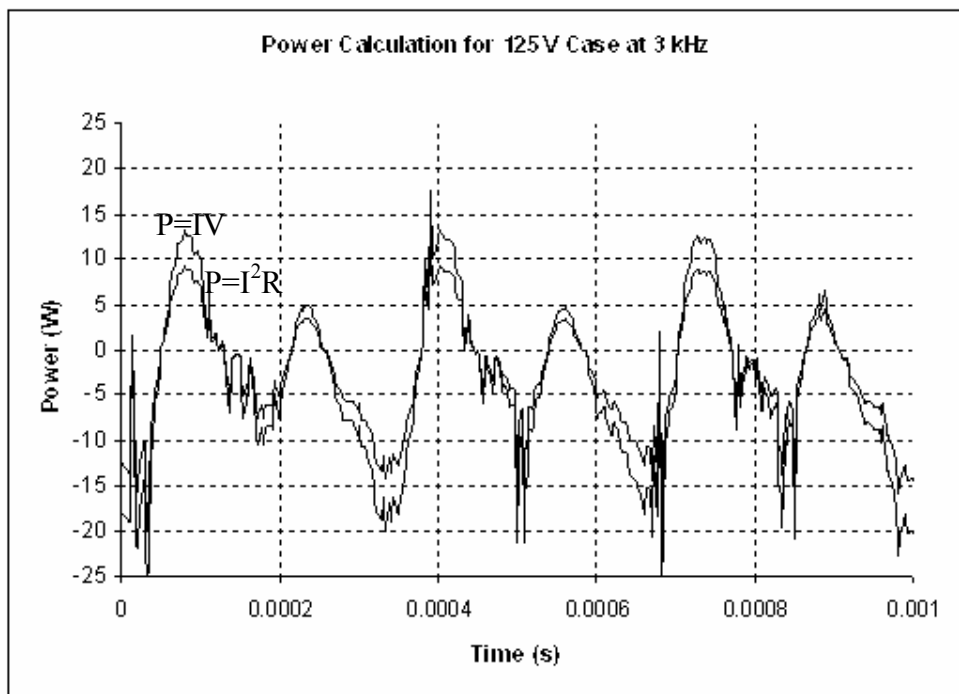


Figure 49. Power plot for $Re = 10,000$ and 25 W plasma.

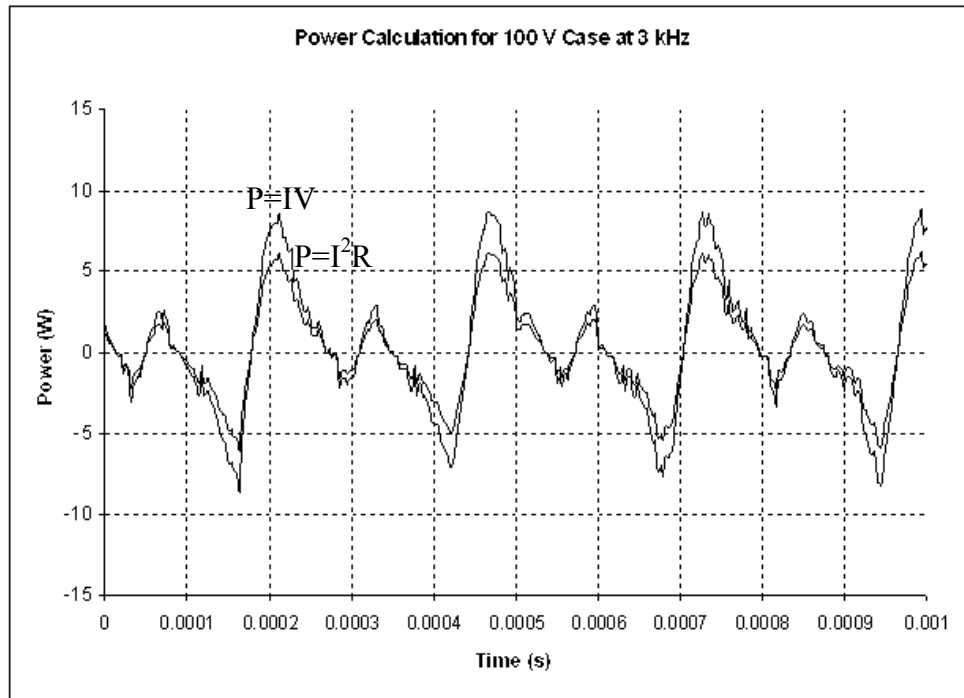


Figure 50. Power plot for $Re = 23,500$ and 15 W plasma.

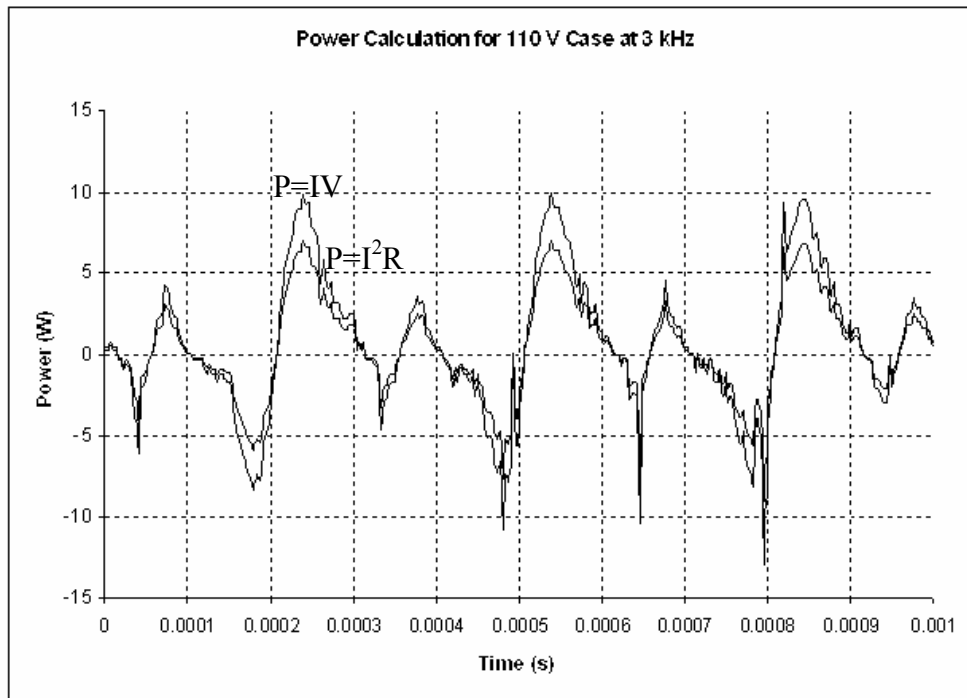


Figure 51. Power plot for $Re = 23,500$ and 20 W plasma.

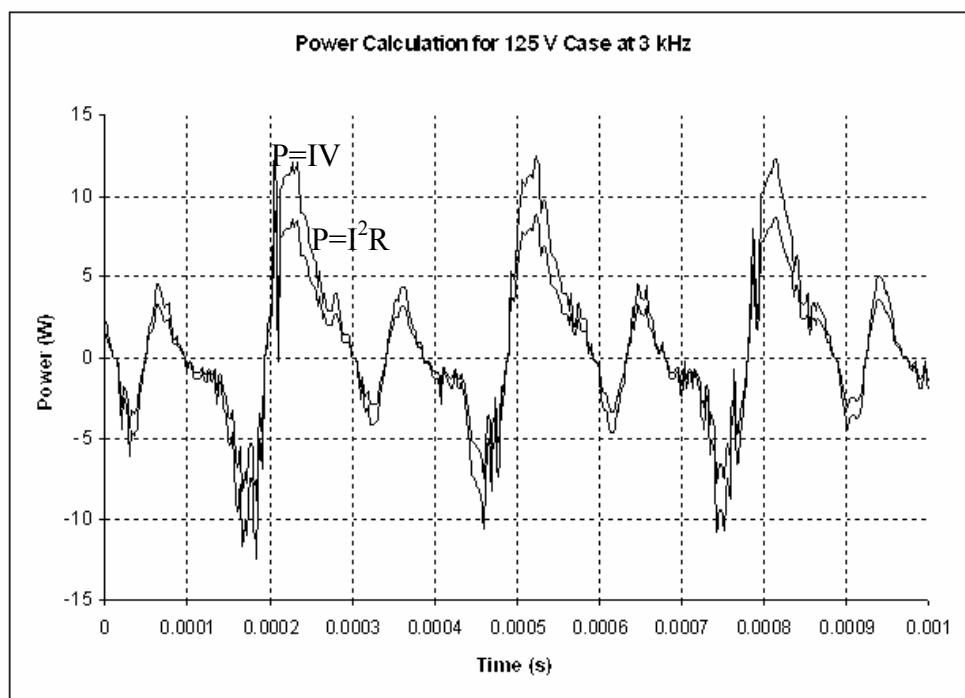


Figure 52. Power plot for $Re = 23,500$ and 25 W plasma.

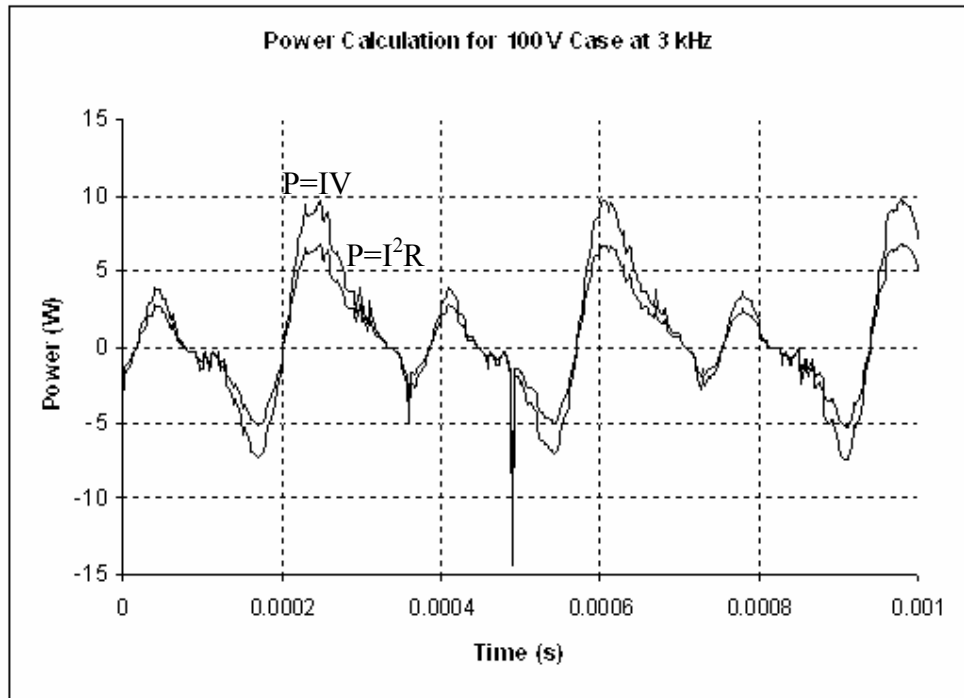


Figure 53. Power plot for $Re = 40,000$ and 15 W plasma.

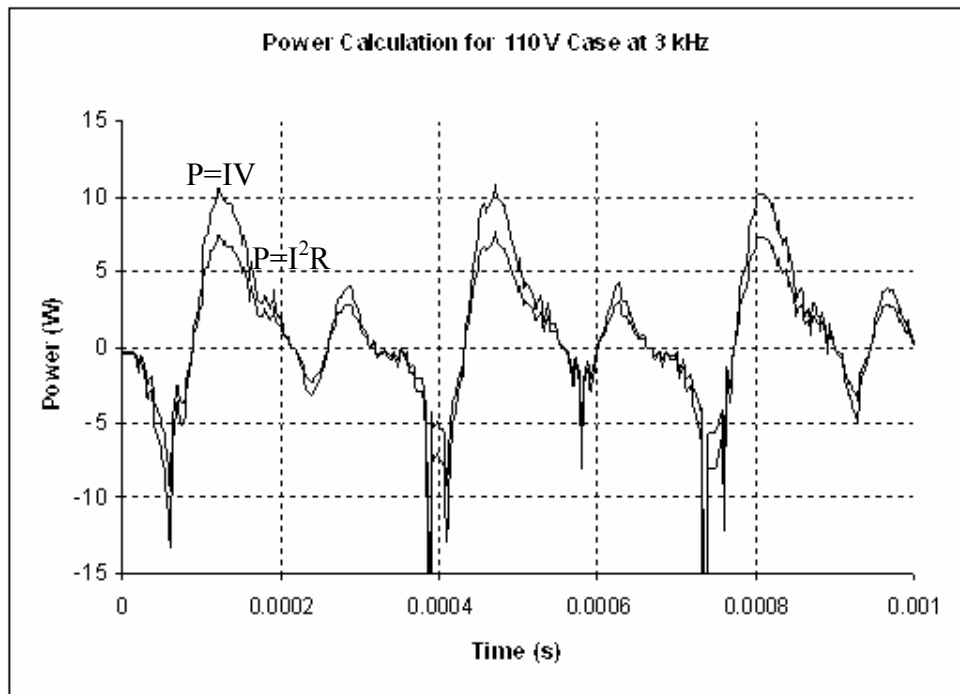


Figure 54. Power plot for $Re = 40,000$ and 20 W plasma.

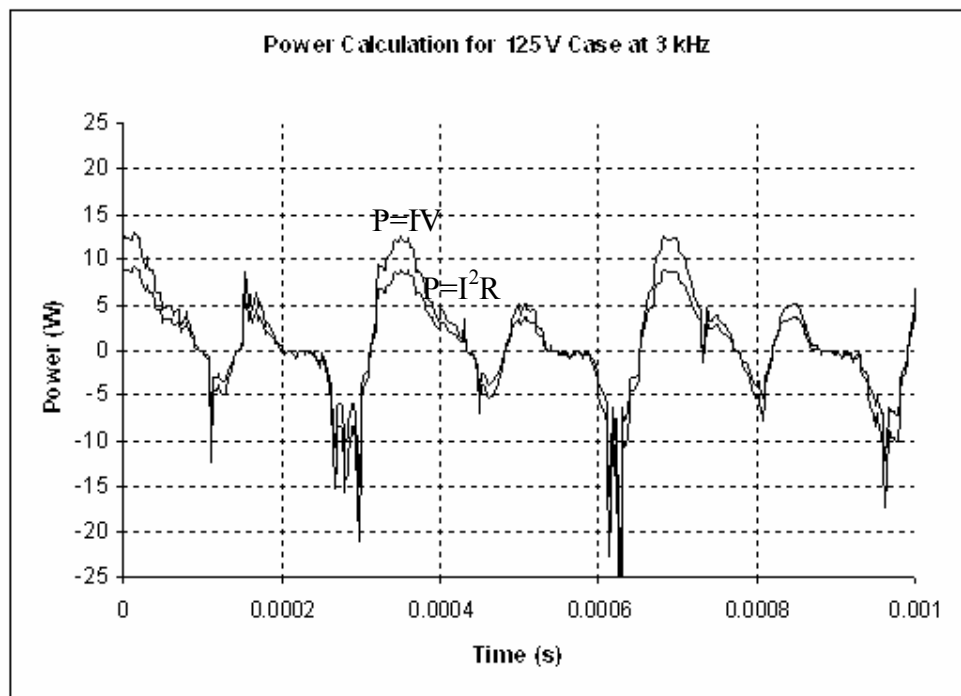


Figure 55. Power plot for $Re = 40,000$ and 25 W plasma.

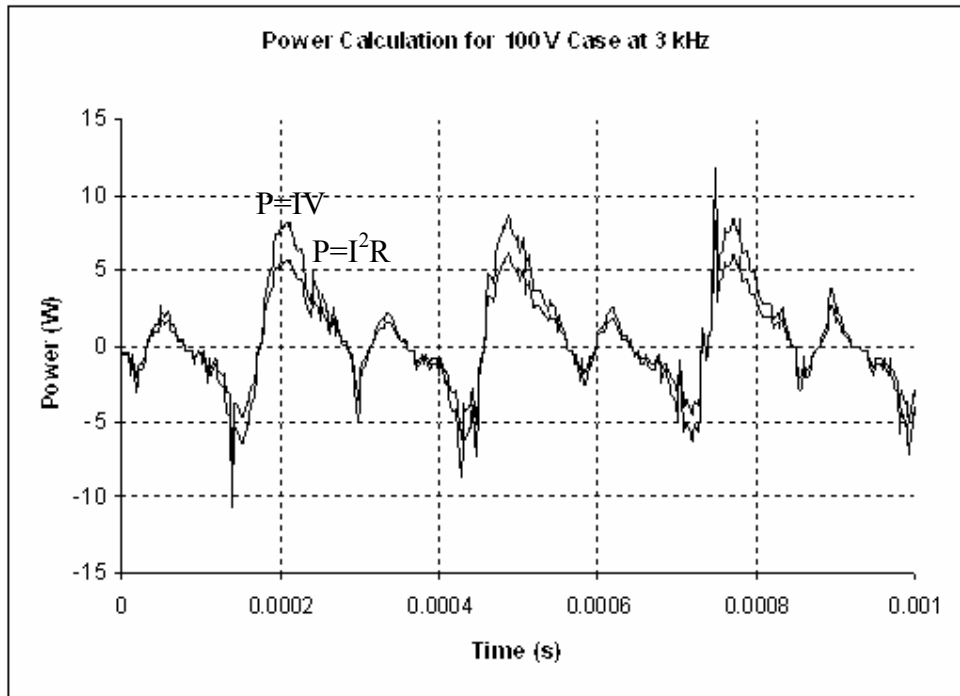


Figure 56. Power plot for $Re = 103,000$ and 15 W plasma.

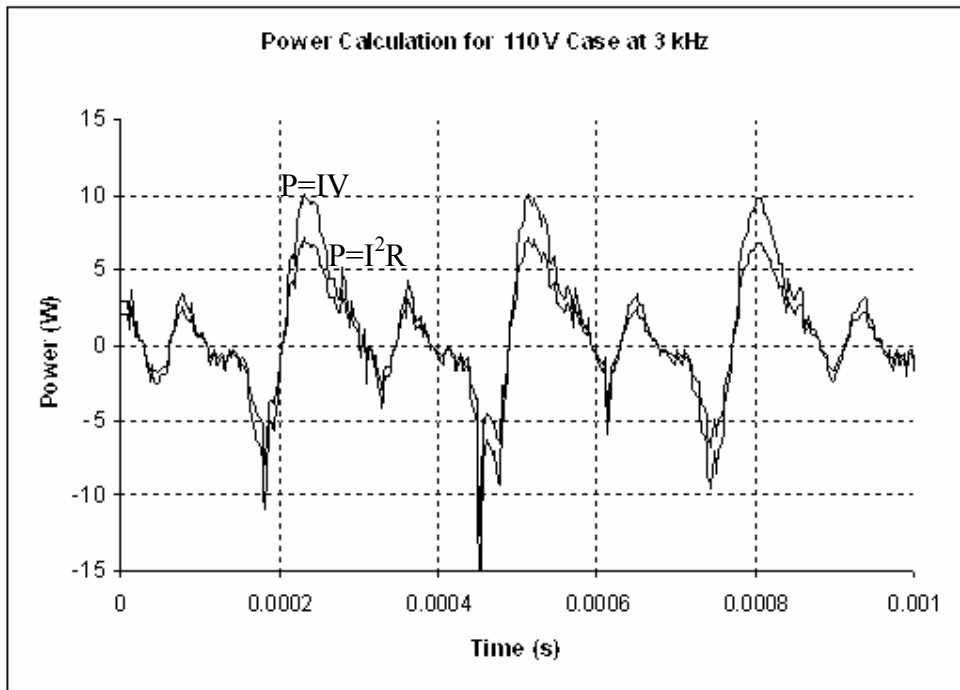


Figure 57. Power plot for $Re = 103,000$ and 20 W plasma.

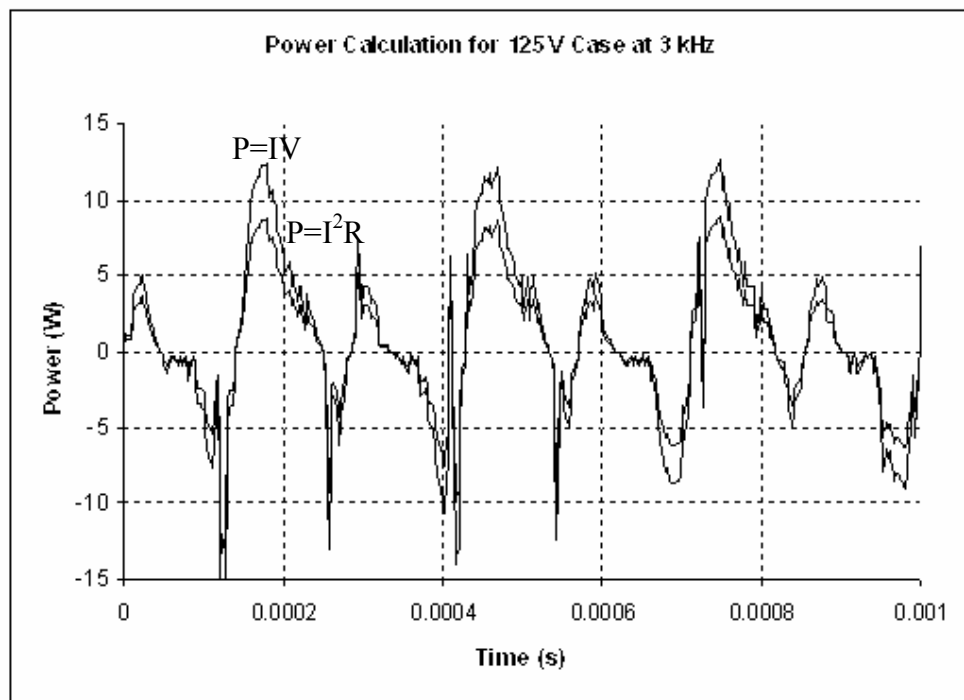


Figure 58. Power plot for $Re = 103,000$ and 25 W plasma.

Appendix B: Procedure for Calibrating a Hot Film Anemometer

The following procedure outlines the steps to calibrate a hot film for use with the IFA-100. Begin by turning on the IFA-100 and allow it to stabilize. Also, eliminate any unnecessary drafts in the locale of the calibration as they will alter the calibration results.

Calibrating the IFA-100

1. Attach a TSI cable (as short a cable as possible) to the hot film probe holder on one end and to the STANDARD PROBE receptacle on the rear of the IFA-100.
2. Adjust the BRIDGE COMP knob on the IFA-100 to a value of 139, which is the documented setting for hot films.
3. Insert the shorting plug into the hot film probe holder.
4. Press the RES MEAS button and balance the bridge to 0 using the OPERATE RES knob.
5. Press the RES MEAS button again so that the DISPL RES light is lit and press ENTER. This will store the cable resistance in the IFA-100's memory.
6. Replace the shorting plug with the hot film.
7. Press the RES MEAS button and balance the bridge to 0 using the OPERATE RES knob.
8. Press the RES MEAS button again so that the DISPL RES light is lit and press ENTER. This will store the probe resistance in the IFA-100's memory.
9. Now, the Operating Resistance (OR) of the setup can be calculated using the Probe Resistance, Internal Probe Resistance (R_{int}), and the overheat ratio (OHR). The Internal Probe Resistance (R_{int}) can be found in the hot film's individual documentation and the OHR is 1.5 for a hot film and 1.8 for a hot wire. $OR = ((\text{Probe Resistance} - R_{int}) \cdot OHR) + R_{int}$.
10. Press the OPERATE RES button and adjust the OPERATE RES knob until it matches the Operating Resistance calculated in step 9.
11. Press the RUN button and then the TEST SIGNAL button.
12. Connect a short TSI cable from the IFA-100's OUTPUT port to an oscilloscope.
13. Adjust the oscilloscope settings to best view the waveform.
14. Adjust the BRIDGE COMP knob until the waveform on the oscilloscope is appears like a crisp square wave. Oscillations may be damped using the FREQ COMP knob.

Obtaining a Calibration Curve for the Hot Film

1. Connect a hot film calibration jet to an air supply and open the valve to allow air to flow freely through the jet – this will ensure all particles are ejected from the calibration column.
2. Position the hot film in the probe holder so that the film is no more than 0.25 in above the exit of the jet nozzle.
3. Connect the hot film to the IFA-100 box as before.
4. Using the thermocouple affixed to the calibration column, record and monitor the temperature of the air jet throughout the calibration.
5. Attach the calibrator's pressure transducer to a data acquisition program to record the pressure at each calibration point.
6. Throttle the air jet up to the maximum anticipated wind tunnel velocity. Record the pressure of the column of air as well as the hot film readings for each calibration point.
7. Develop a calibration curve for the hot film for use in data acquisition software.

Appendix C: Boundary Layer Profiles

The PIV data contained large insights into the near wall boundary conditions. Boundary layer velocity profiles derived from the PIV results are contained in this appendix for two locations with respect to the top electrode: located 7.1 mm and 12.7 mm aft of the leading edge of the top electrode. Due to the field of view of cases 1-3 ($Re = 10,000$), the second profile was taken at 12.2 mm aft of the leading edge of the top electrode. The images are arranged from case 1 to case 15, by increasing Reynolds number. Note that the highest power setting did not always have the largest effect on the boundary layer at all locations. One trend shows that the lower speed cases were affected most by the plasma actuator.

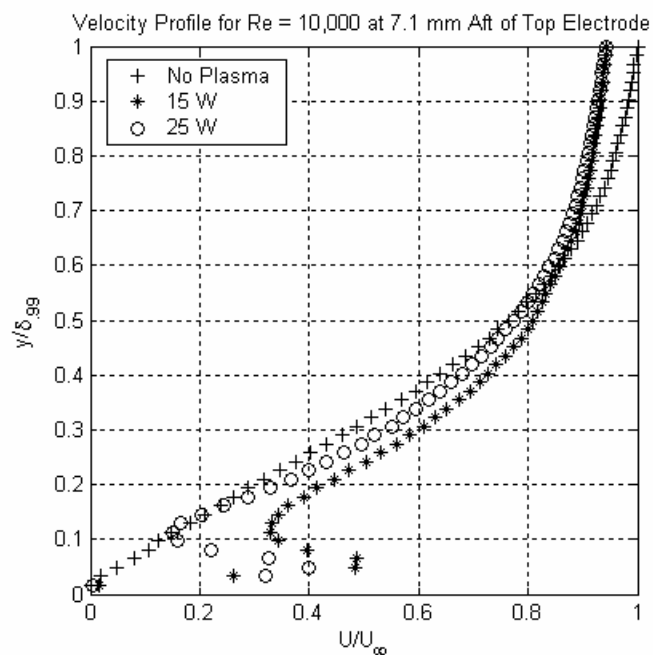


Figure 59. Velocity profile for $Re = 10,000$ at 7.1 mm aft of the top electrode.

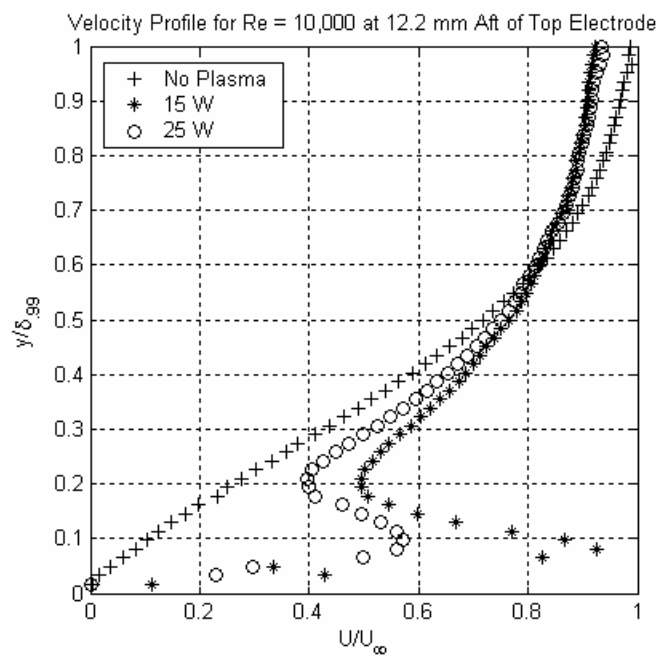


Figure 60. Velocity profile for $Re = 10,000$ at 12.2 mm aft of the top electrode.

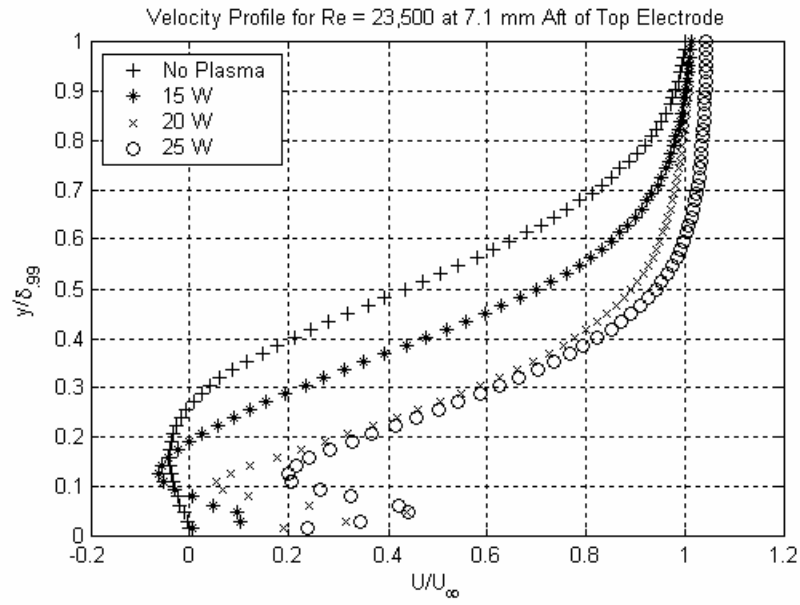


Figure 61. Velocity profile for $Re = 23,500$ at 7.1 mm aft of the top electrode.

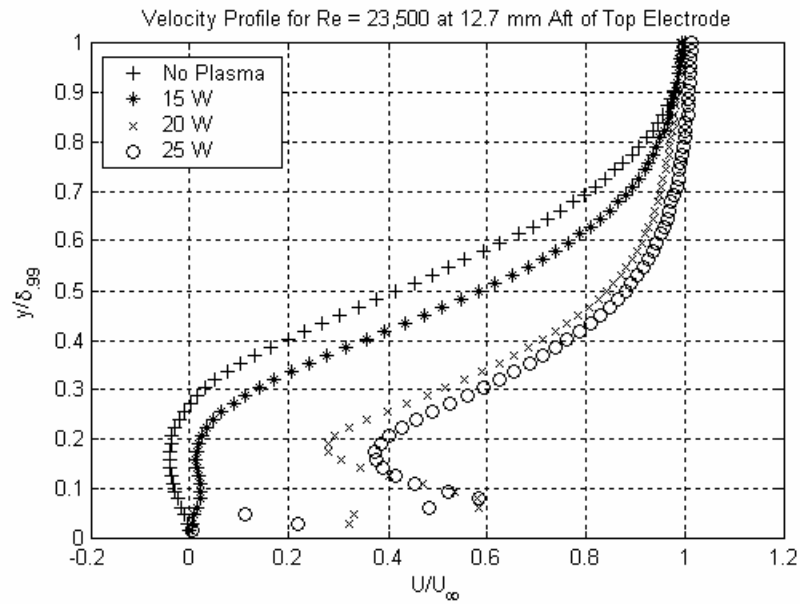


Figure 62. Velocity profile for $Re = 23,500$ at 12.7 mm aft of the top electrode.

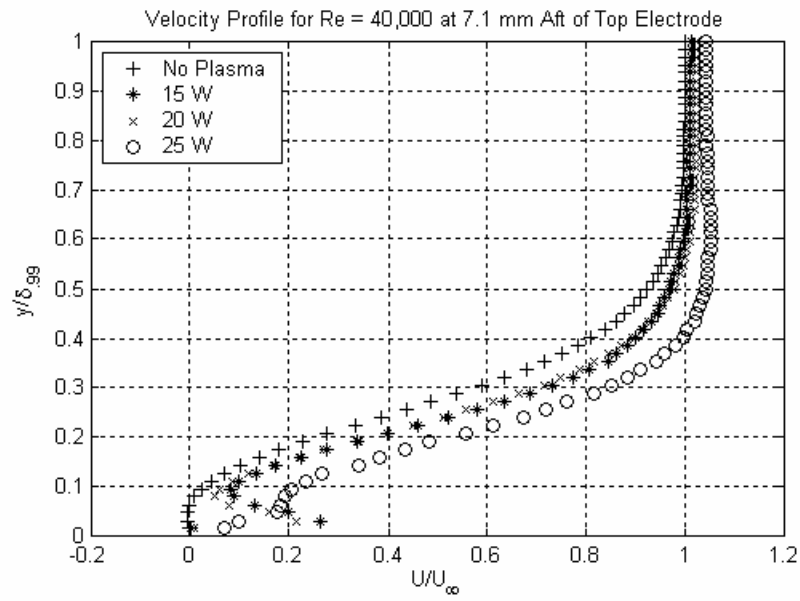


Figure 63. Velocity profile for $Re = 40,000$ at 7.1 mm aft of the top electrode.

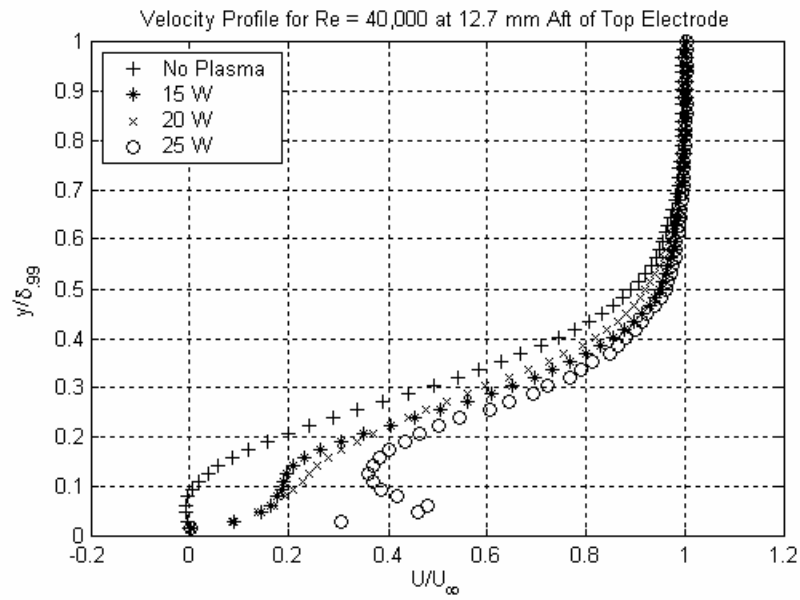


Figure 64. Velocity profile for $Re = 40,000$ at 12.7 mm aft of the top electrode.

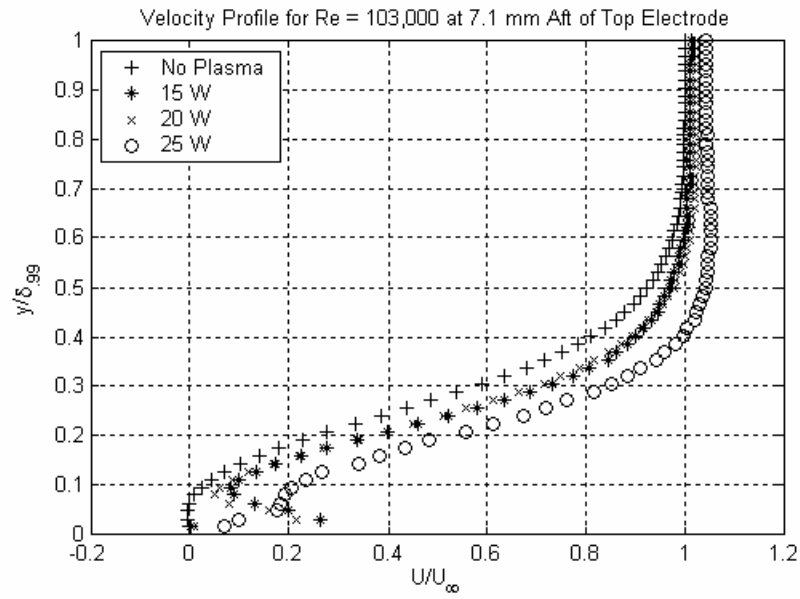


Figure 65. Velocity profile for $Re = 103,000$ at 7.1 mm aft of the top electrode.

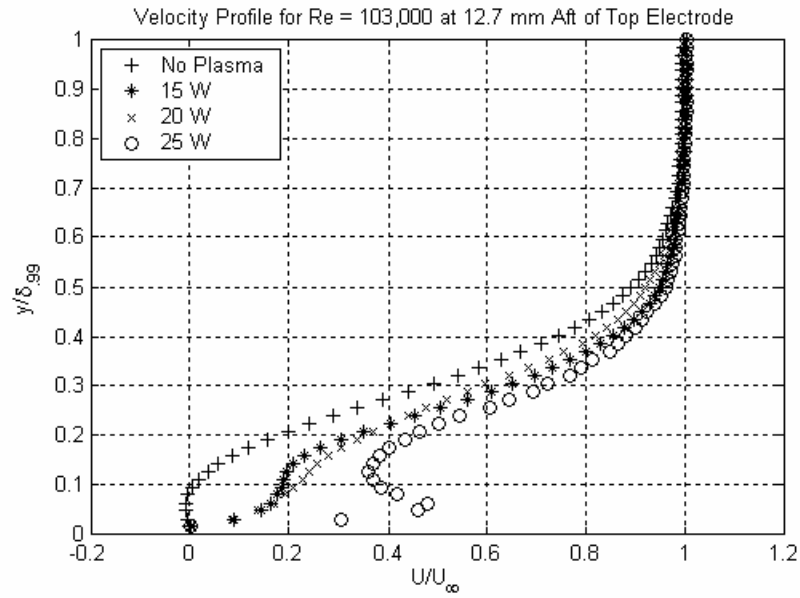


Figure 66. Velocity profile for $Re = 103,000$ at 12.7 mm aft of the top electrode.

Appendix D: Velocity Vector Plots

This appendix contains the velocity vector plots for the 15 cases shown in Table 1. The plots are ordered from low Reynolds number to high, beginning with the no plasma cases, followed by 15 W of plasma, 20 W of plasma and 25 W of plasma. In each flow field, the freestream velocity is traveling from the left to the right while the origin of the plot is located at the midpoint between the two electrodes. Therefore, to the left of the zero-point is the exposed electrode and to the right of the zero-point is the buried electrode. A digital rendering of the electrodes was added to the plots to show the relative size of the electrodes, however, the height of the electrodes has been dramatized. The first row of vectors above the electrodes is shown offset by 16 pixels, or the location where the first seeding particles could be discerned.

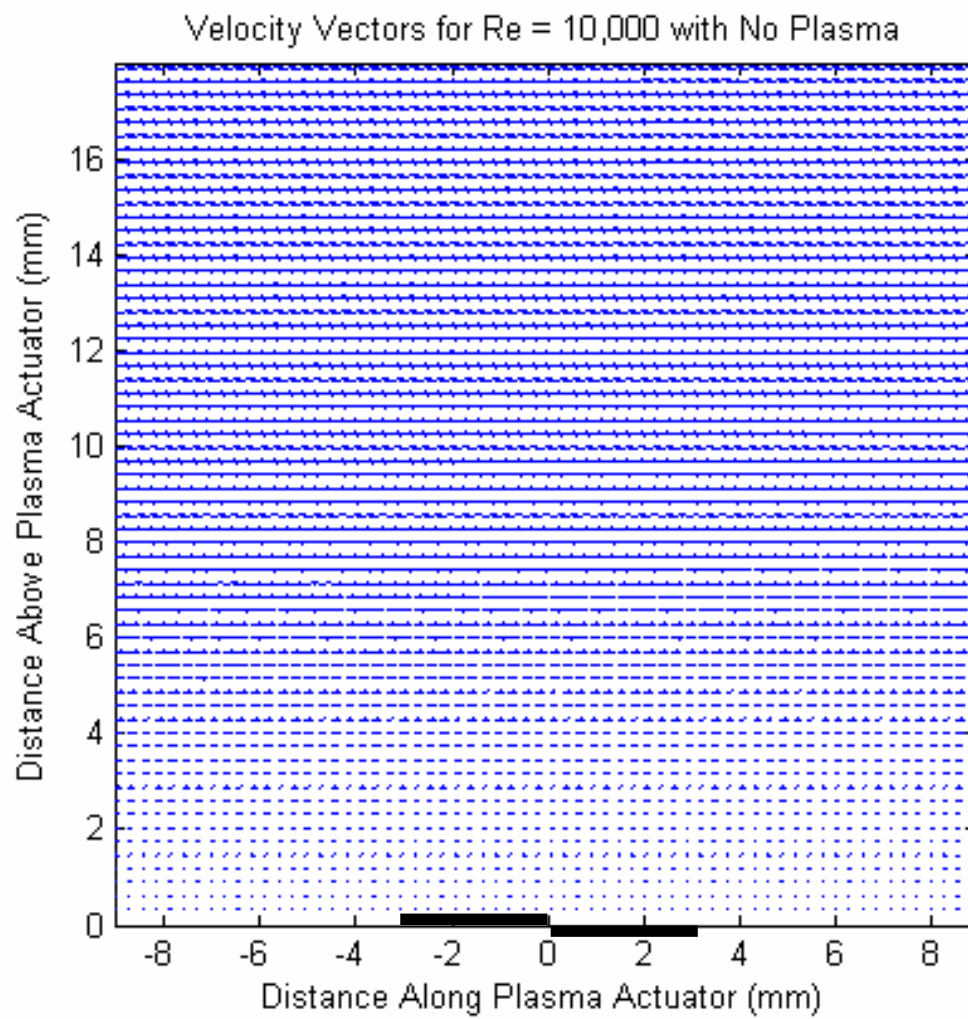


Figure 67. Velocity vectors for $Re = 10,000$ with no plasma.

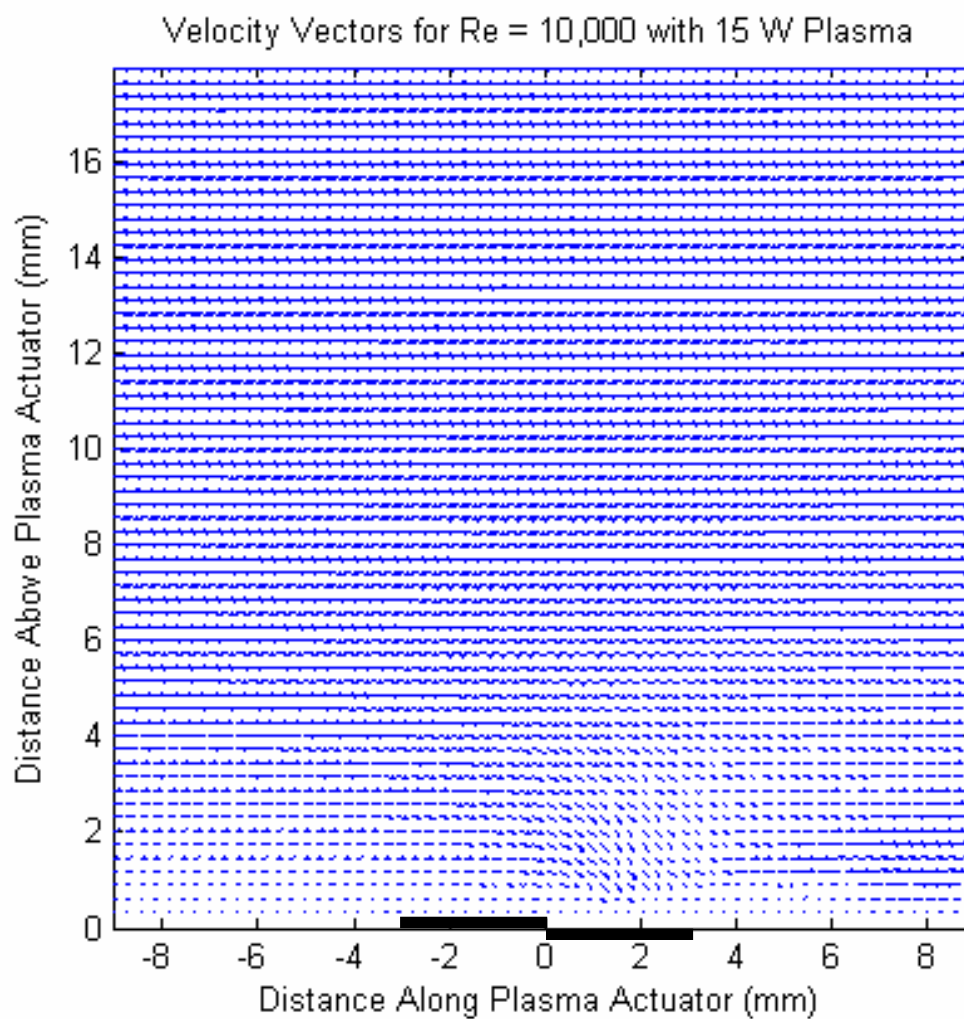


Figure 68. Velocity vectors for $Re = 10,000$ with 15 W plasma.

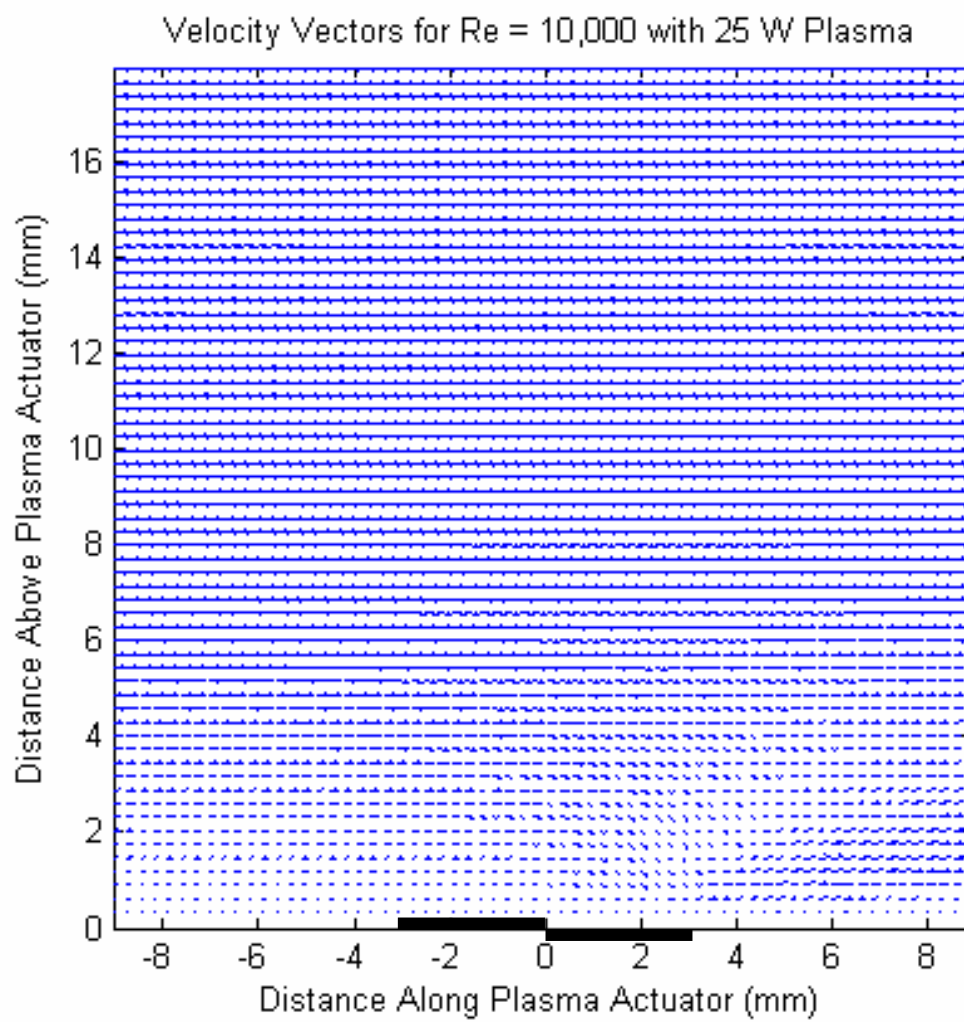


Figure 69. Velocity vectors for $Re = 10,000$ with 25 W plasma.

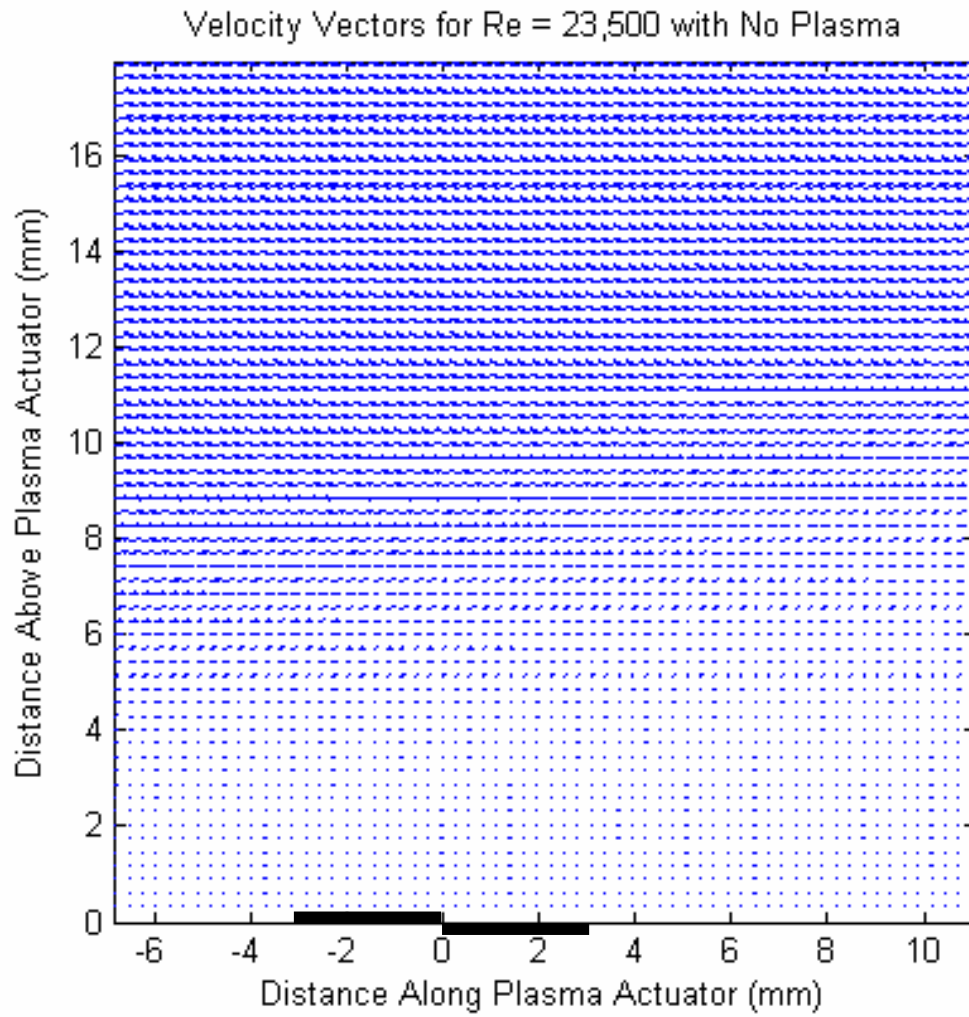


Figure 70. Velocity vectors for $Re = 23,500$ with no plasma.

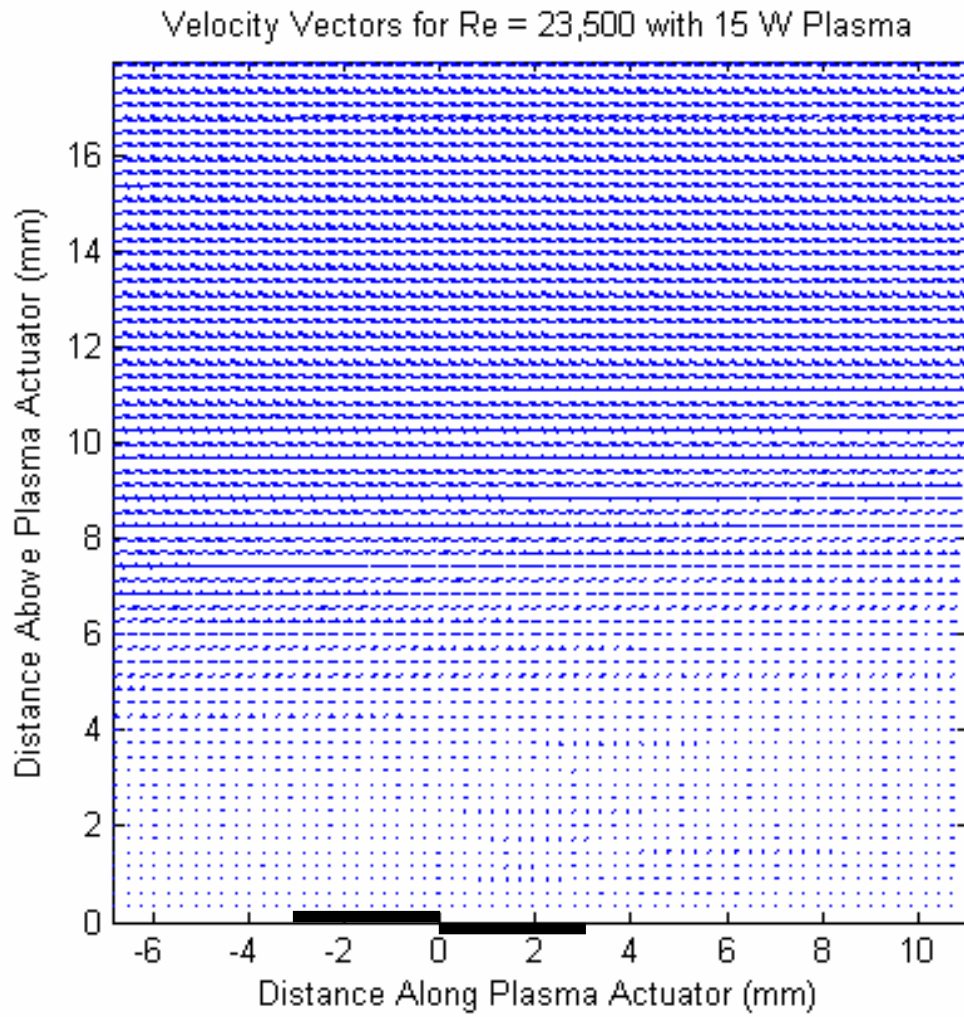


Figure 71. Velocity vectors for $Re = 23,500$ with 15 W plasma.

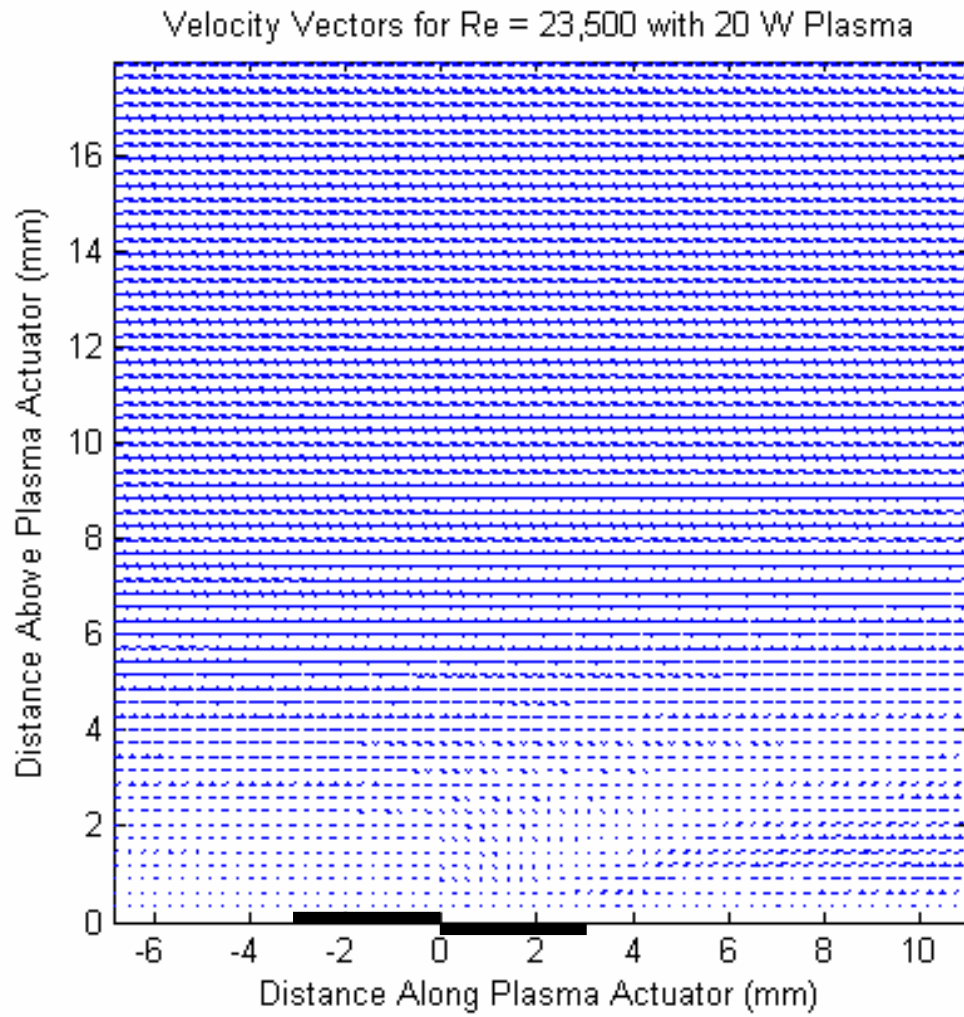


Figure 72. Velocity vectors for $Re = 23,500$ with 20 W plasma.

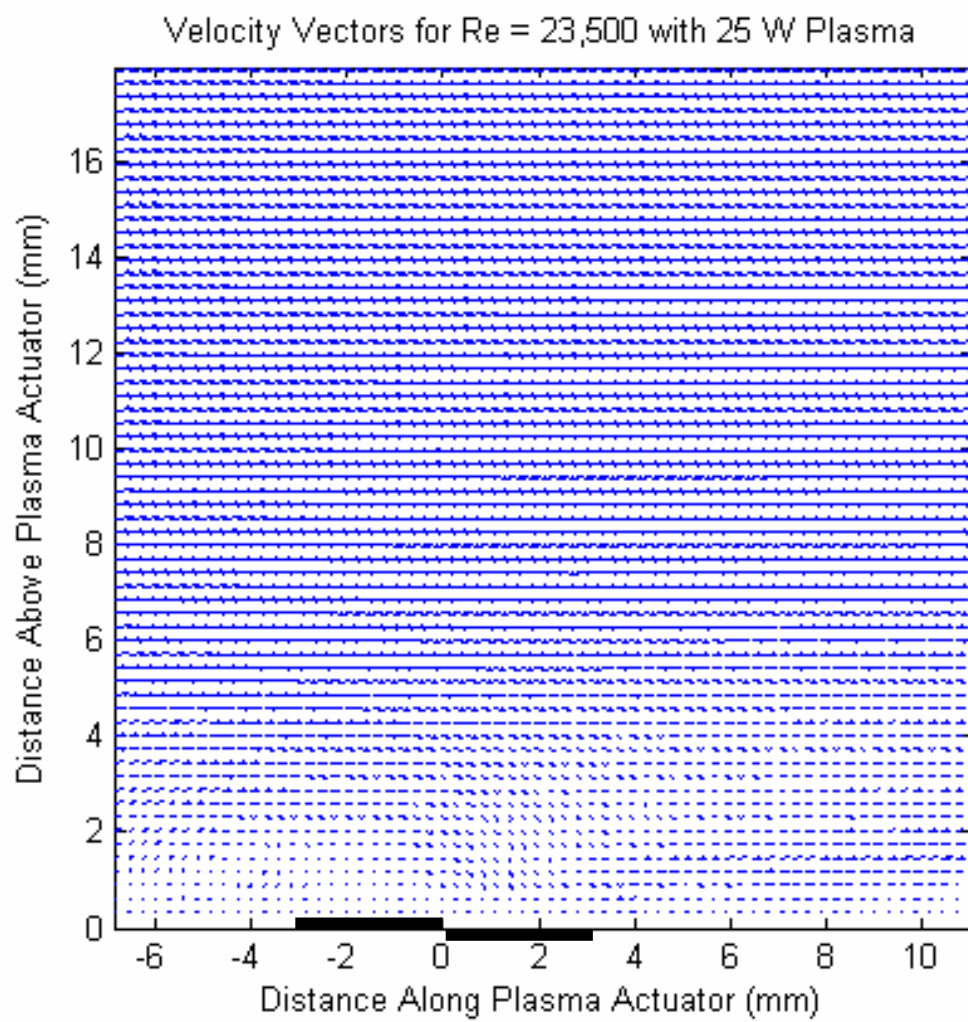


Figure 73. Velocity vectors for $Re = 23,500$ with 25 W plasma.

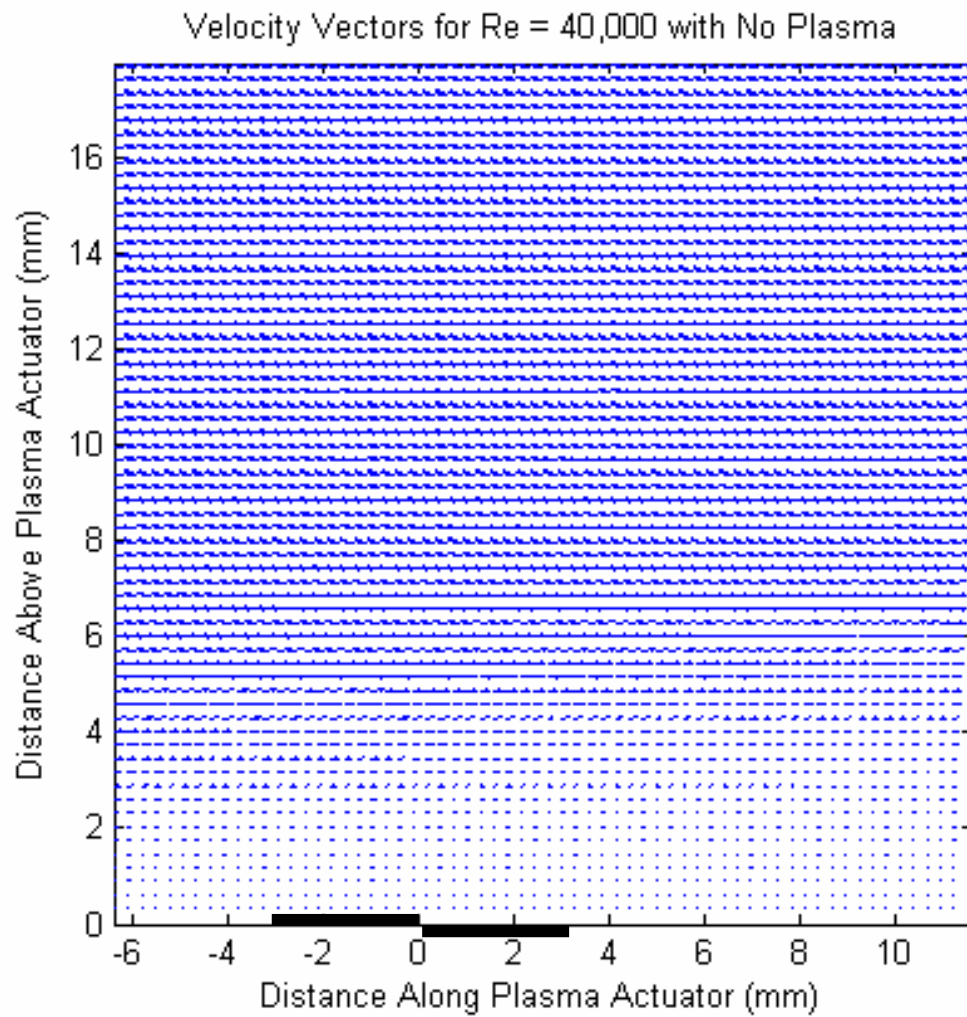


Figure 74. Velocity vectors for $Re = 40,000$ with no plasma.

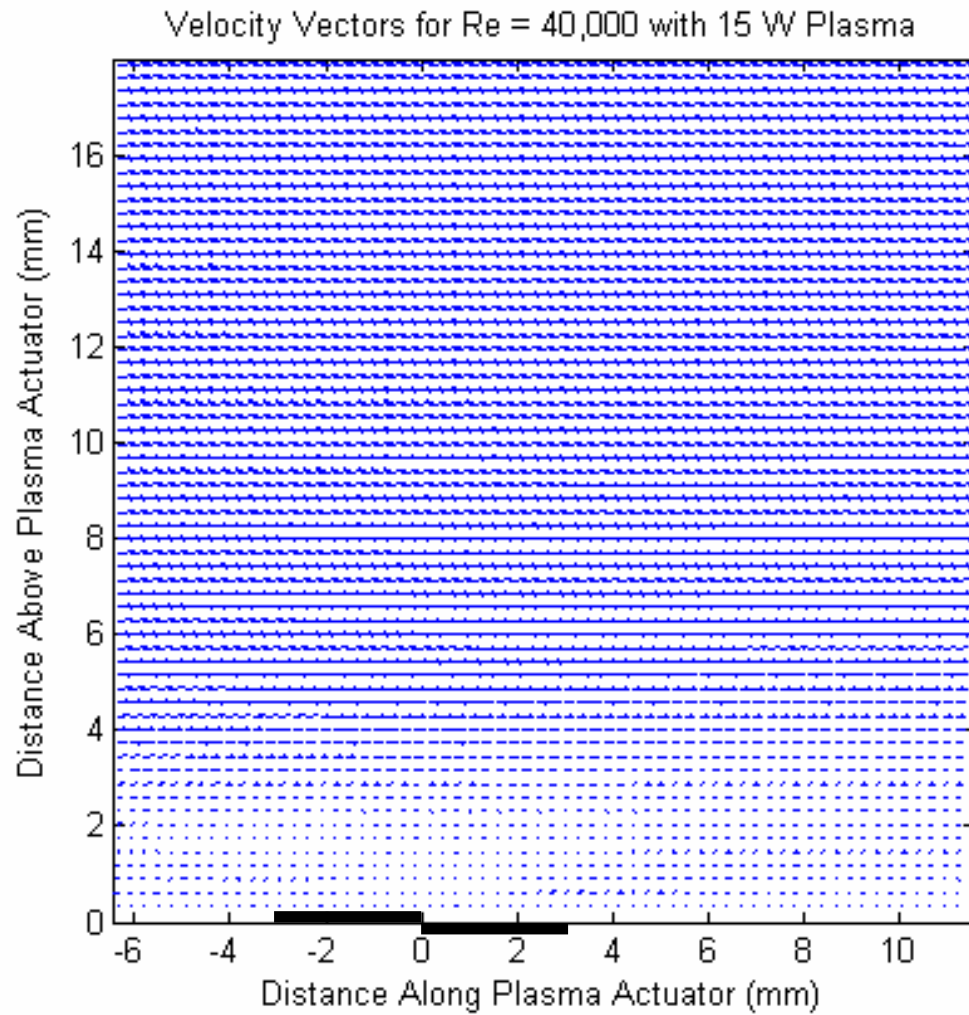


Figure 75. Velocity vectors for $Re = 40,000$ with 15 W plasma.

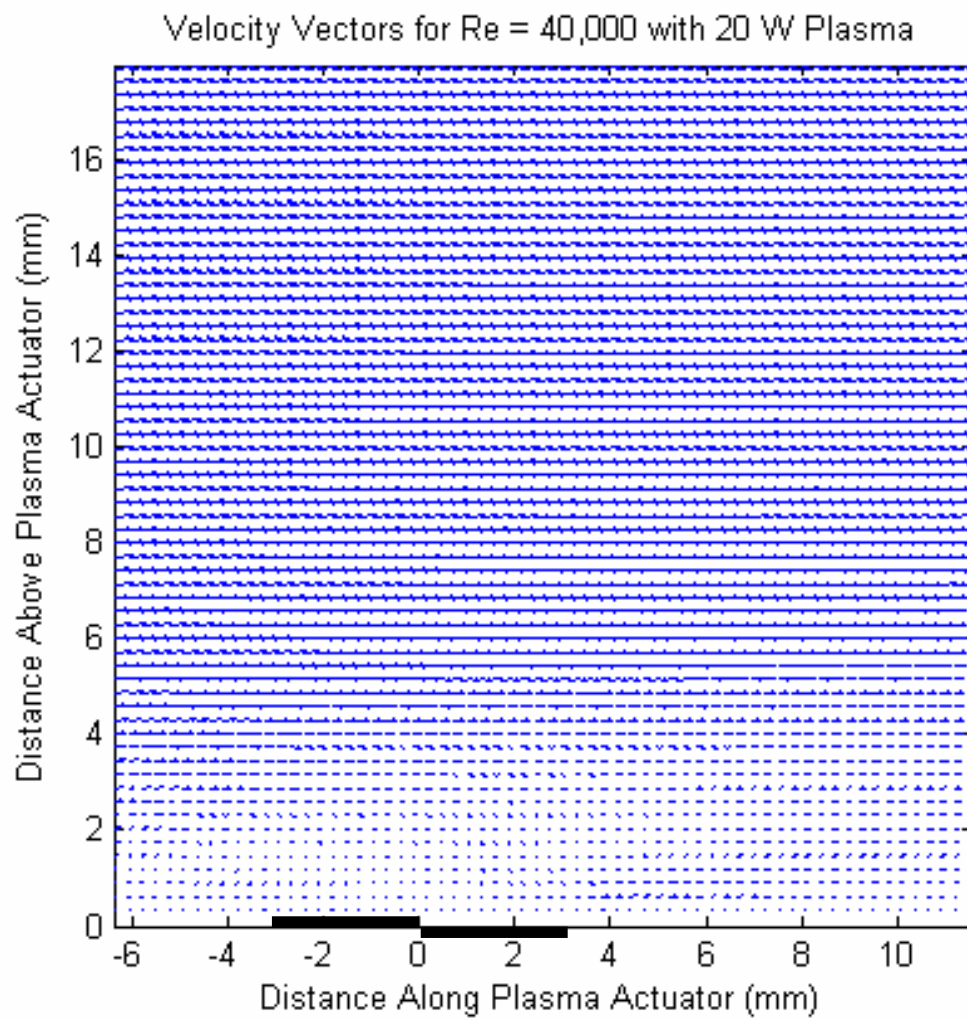


Figure 76. Velocity vectors for $Re = 40,000$ with 20 W plasma.

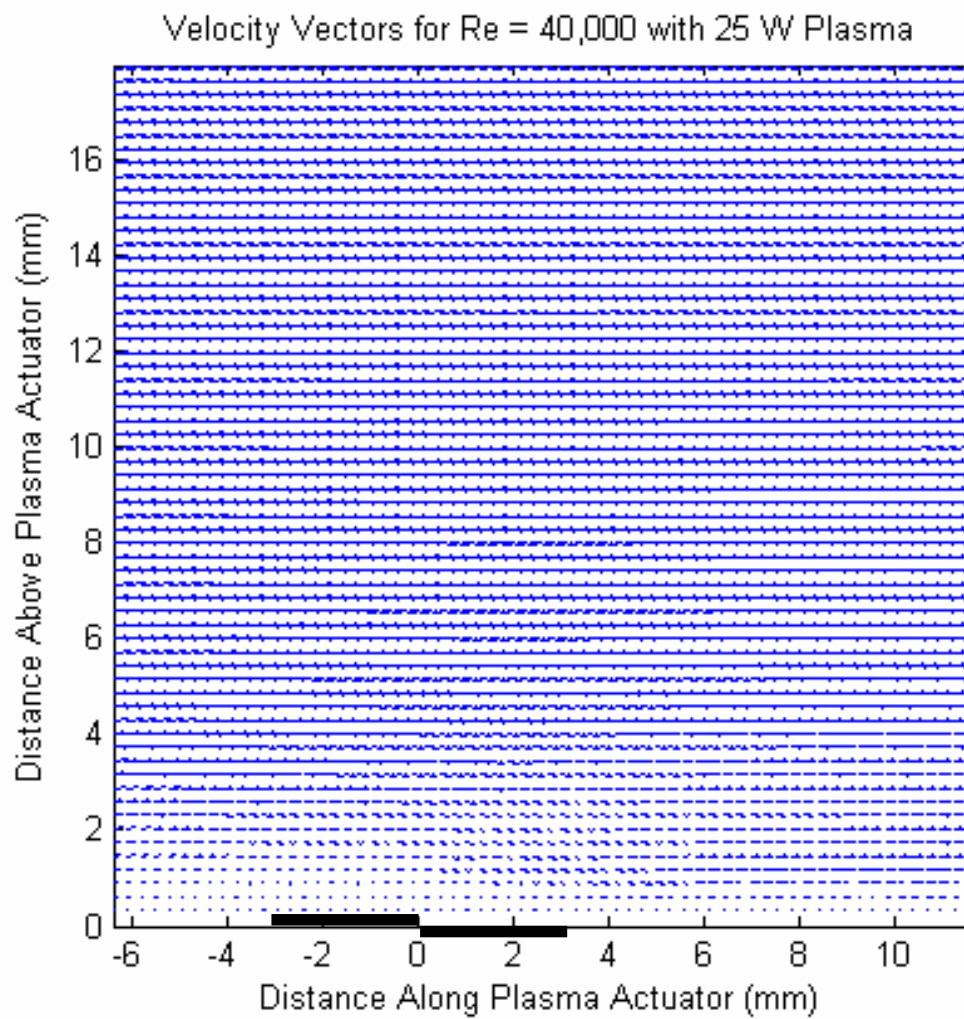


Figure 77. Velocity vectors for $Re = 40,000$ with 25 W plasma.

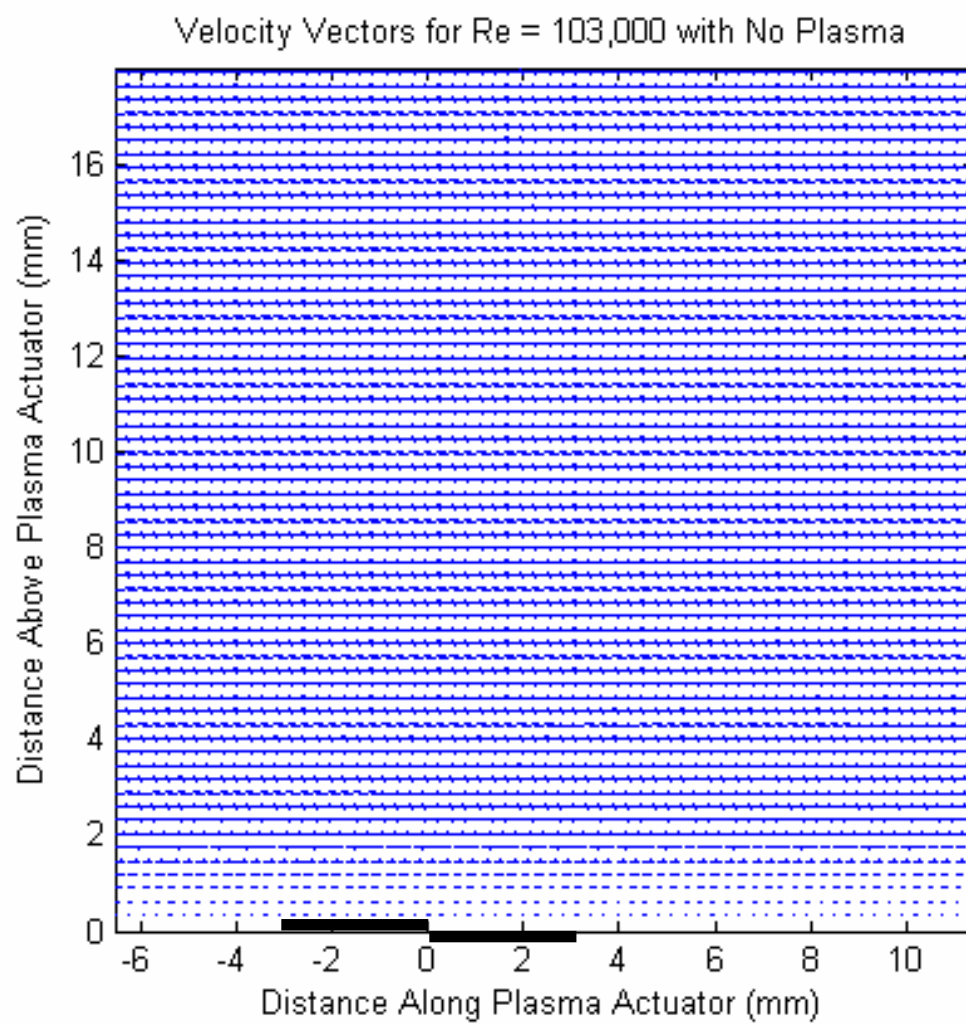


Figure 78. Velocity vectors for $Re = 103,000$ with no plasma.

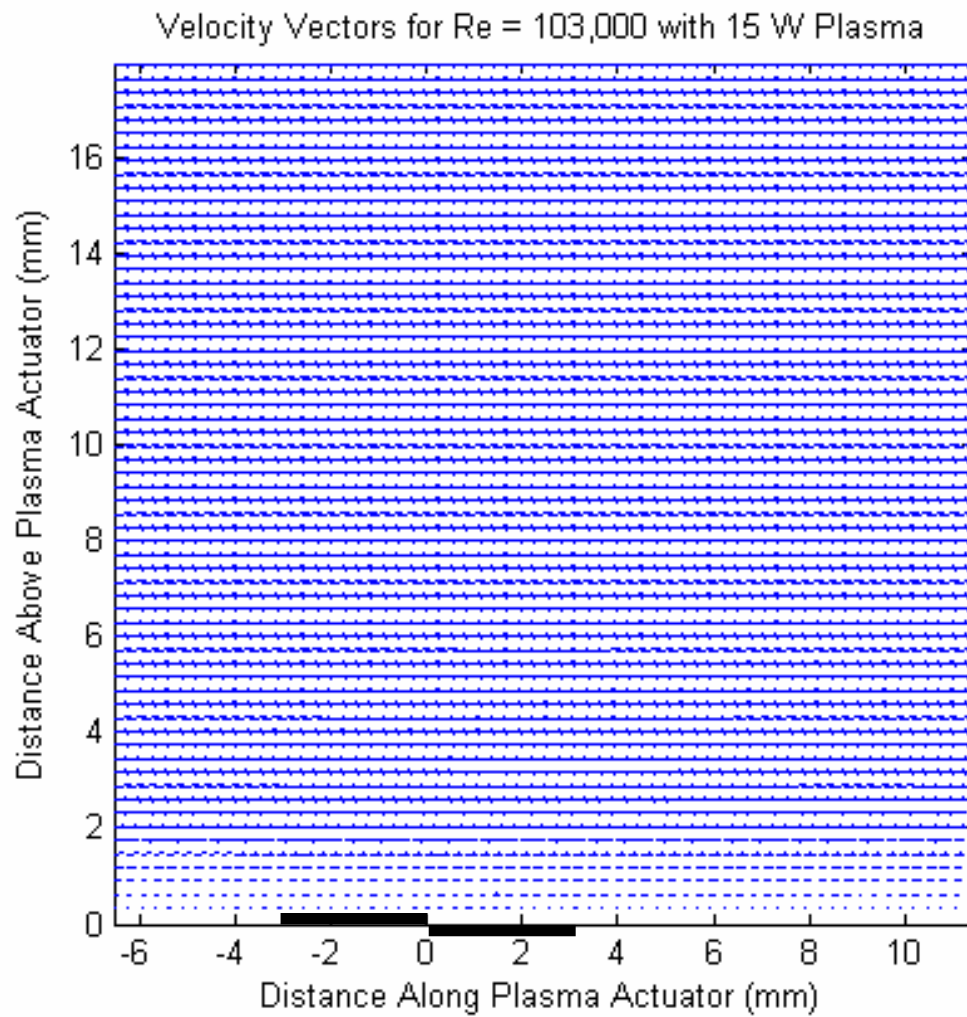


Figure 79. Velocity vectors for $Re = 103,000$ with 15 W plasma.

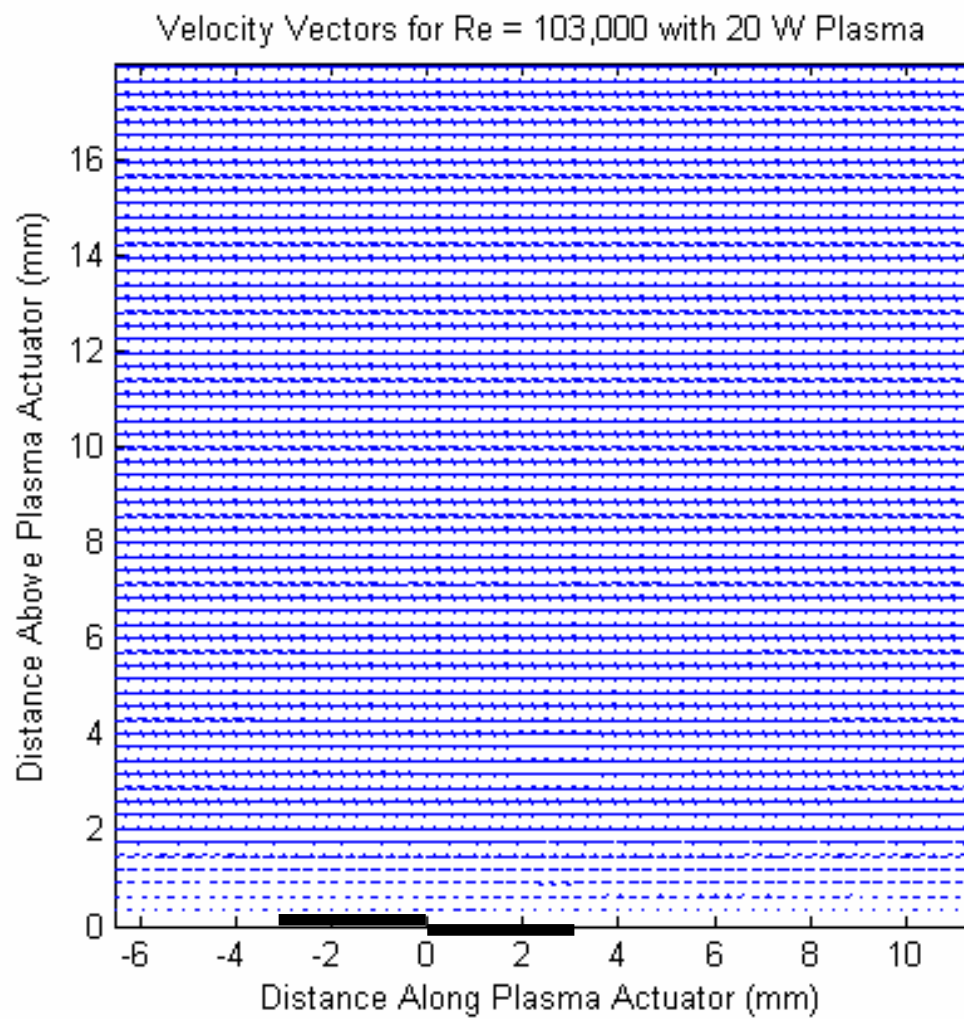


Figure 80. Velocity vectors for $Re = 103,000$ with 20 W plasma.

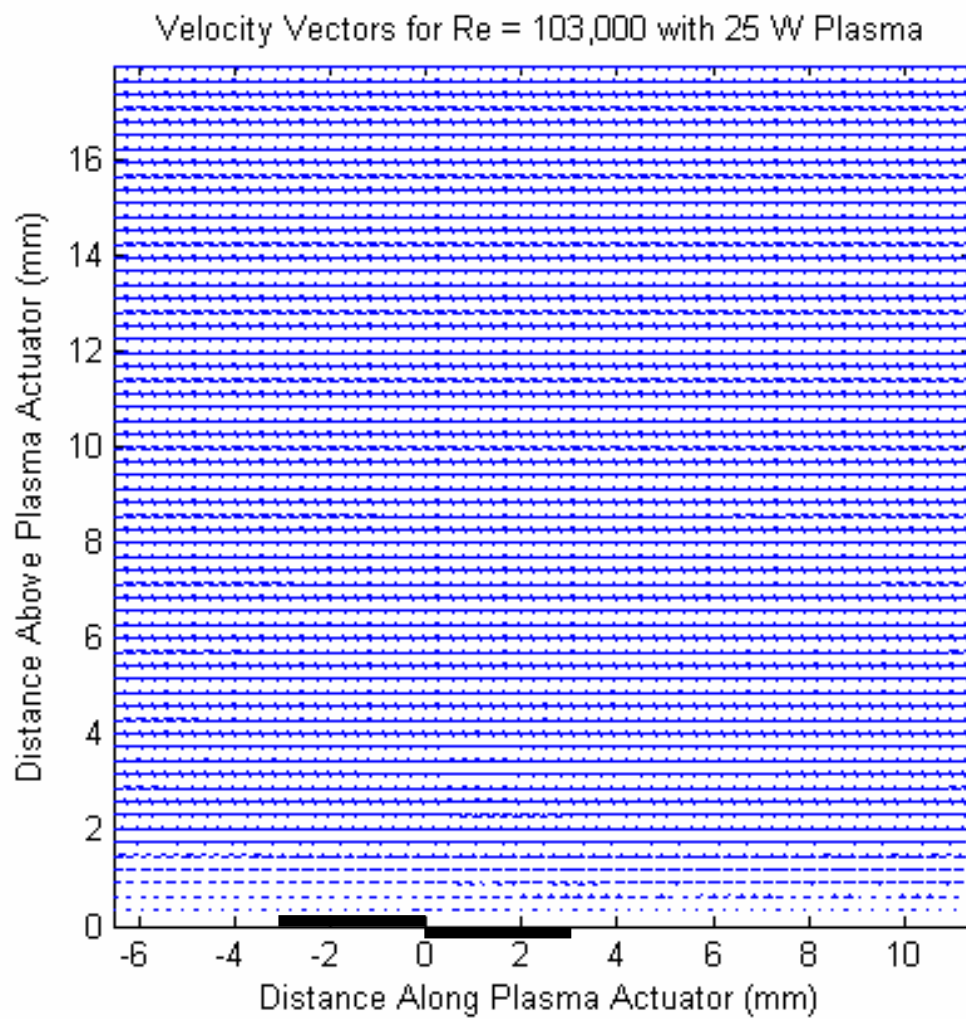


Figure 81. Velocity vectors for $Re = 103,000$ with 25 W plasma.

Appendix E: Vorticity Contour Plots

The vorticity contour plots contained in this appendix are averages. The flow direction is left to right and the location of the origin on the plots is the midpoint between the two electrodes. Digital renderings of the electrodes have not been added to allow easier viewing of the near wall phenomena. A color bar scale has been added to each plot for clarity and it is calibrated in radians per second. All fifteen cases are shown, but note that the color bar scales vary throughout in order to give better vorticity resolution.

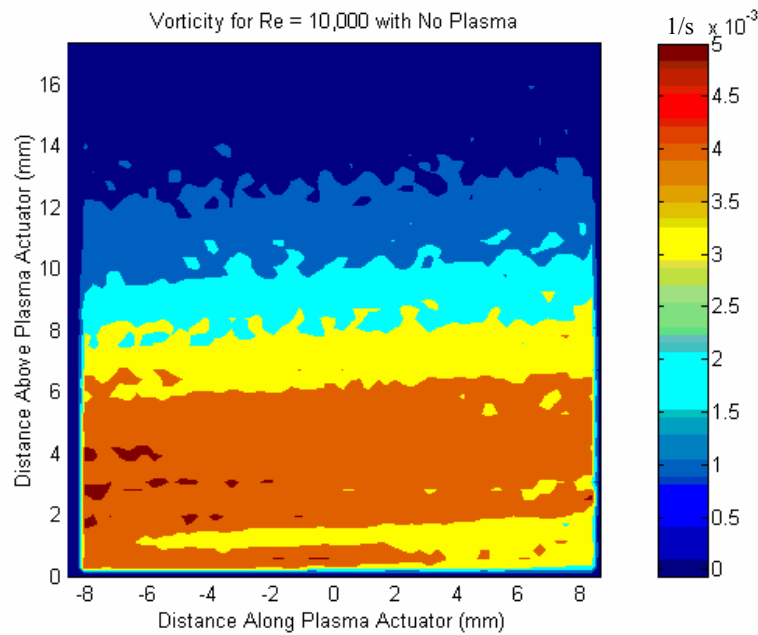


Figure 82. Contour plot of vorticity for Re = 10,000 with no plasma.

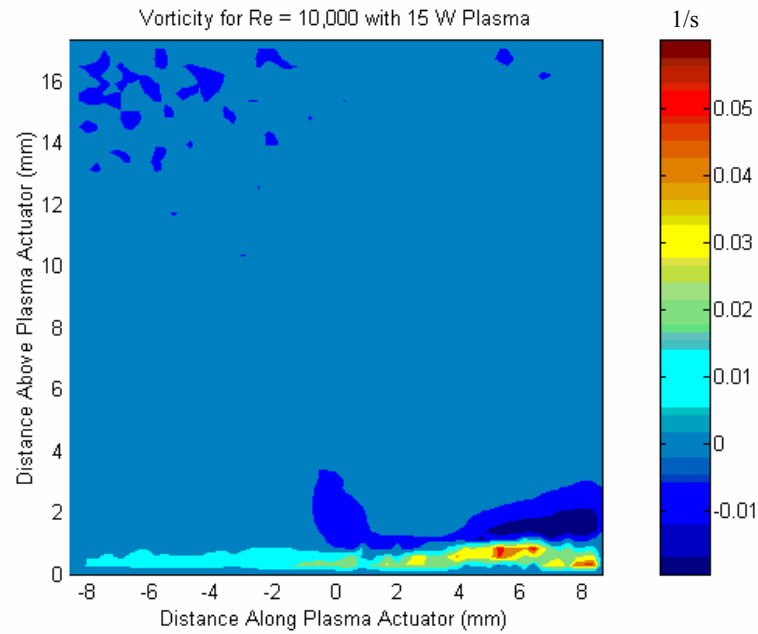


Figure 83. Contour plot of vorticity for $Re = 10,000$ with 15 W plasma.

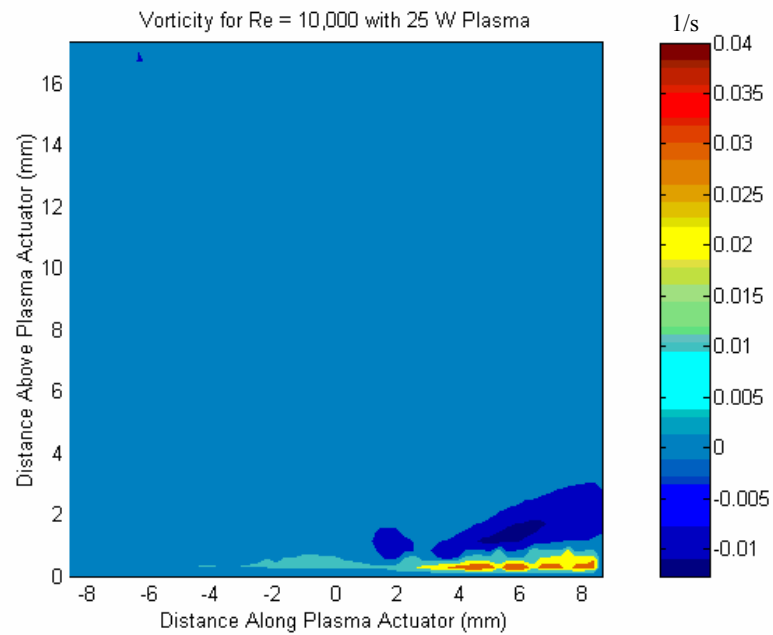


Figure 84. Contour plot of vorticity for $Re = 10,000$ with 25 W plasma.

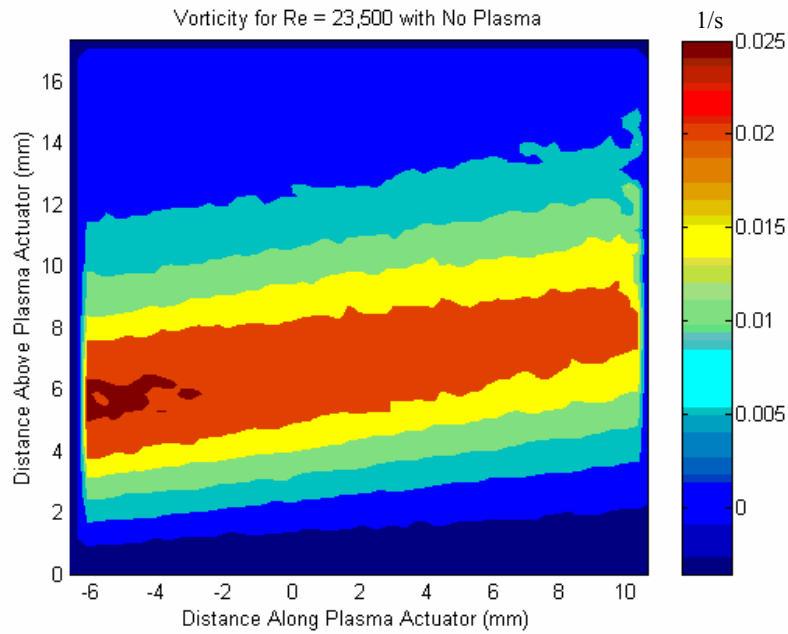


Figure 85. Contour plot of vorticity for $Re = 23,500$ with no plasma.

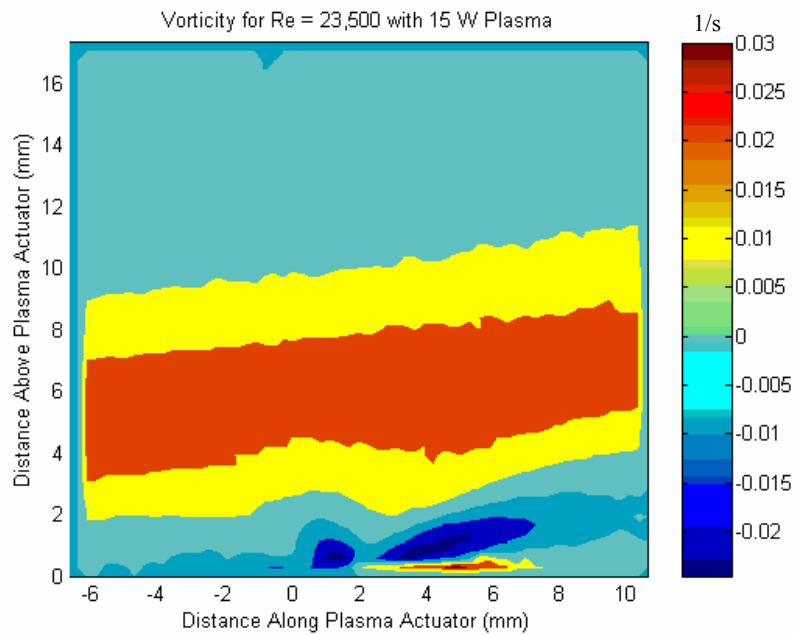


Figure 86. Contour plot of vorticity for $Re = 23,500$ with 15 W plasma.

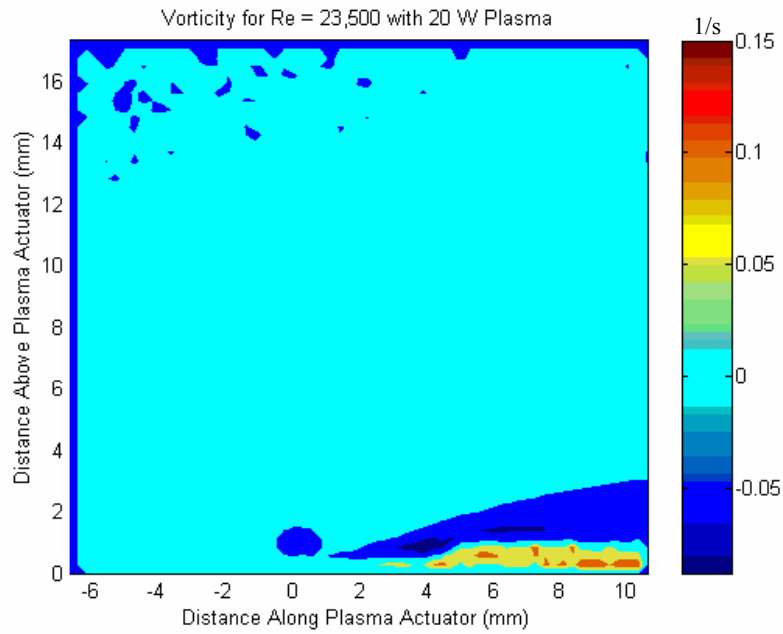


Figure 87. Contour plot of vorticity for $Re = 23,500$ with 20 W plasma.

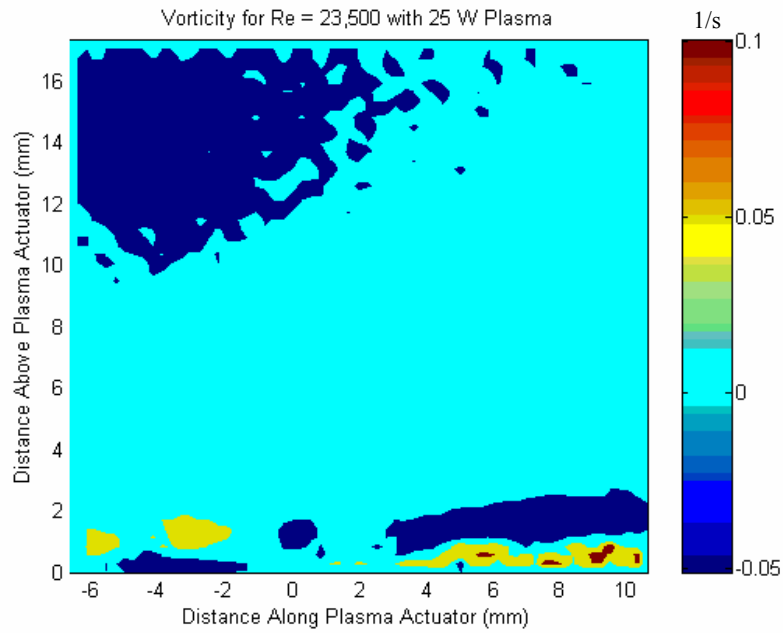


Figure 88. Contour plot of vorticity for $Re = 23,500$ with 25 W plasma.

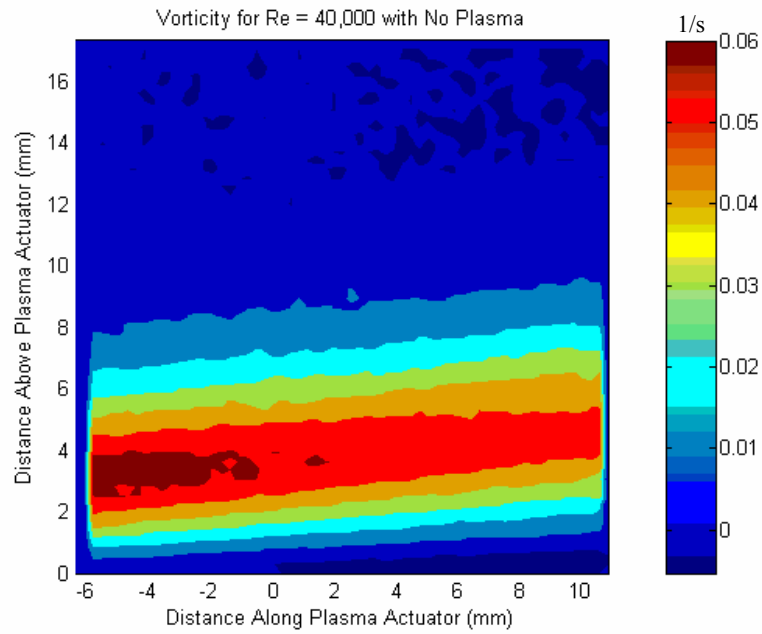


Figure 89. Contour plot of vorticity for Re 40,000 with no plasma.

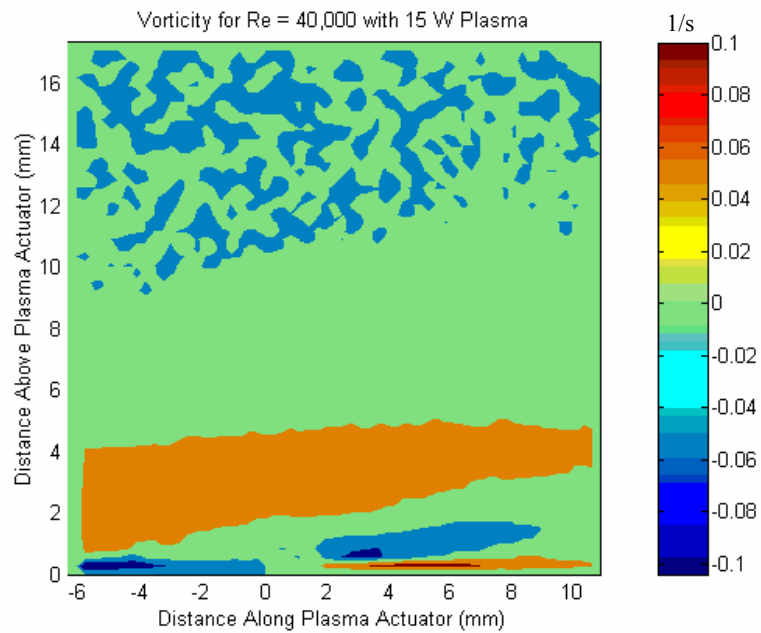


Figure 90. Contour plot of vorticity for $Re = 40,000$ with 15 W plasma.

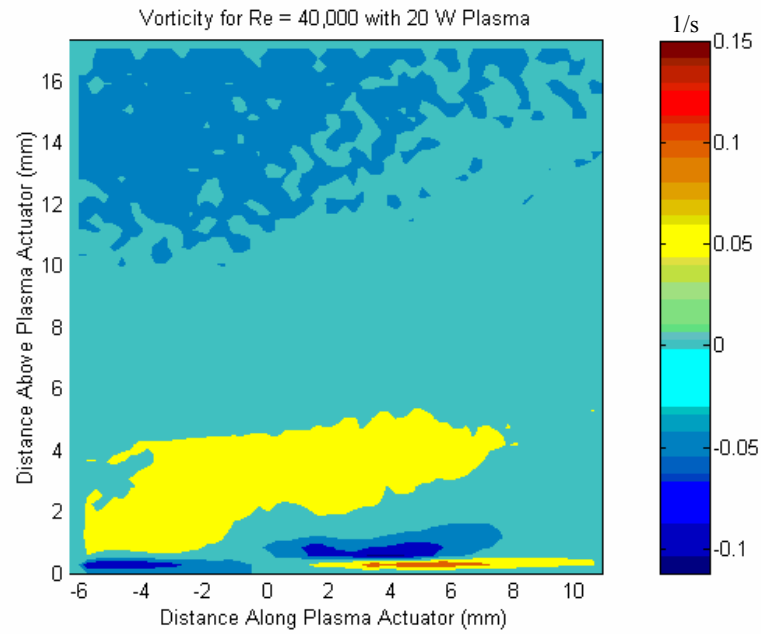


Figure 91. Contour plot of vorticity for $Re = 40,000$ with 20 W plasma.

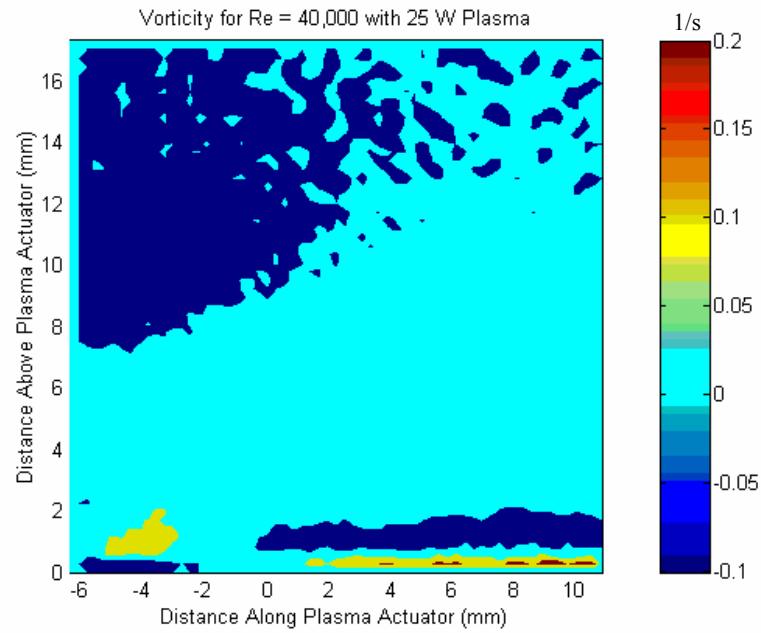


Figure 92. Contour plot of vorticity for $Re = 40,000$ with 25 W plasma.

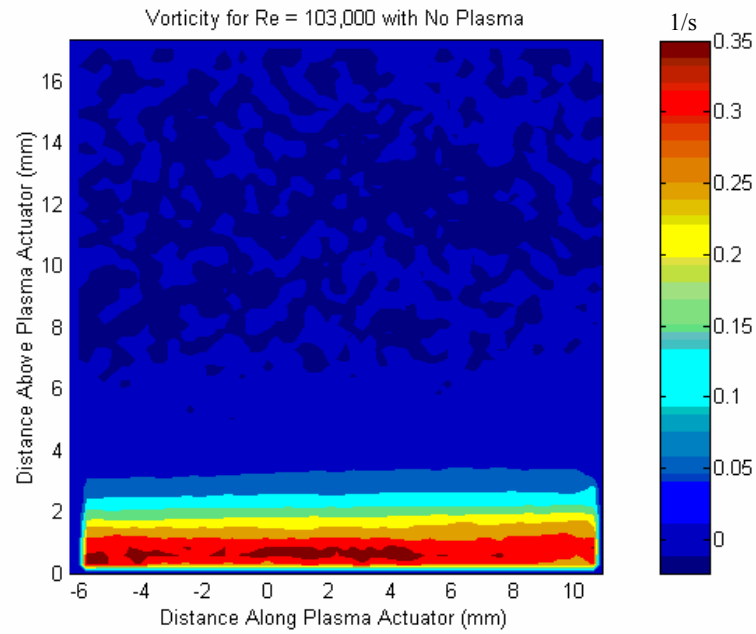


Figure 93. Contour plot of vorticity for $Re = 103,000$ with no plasma.

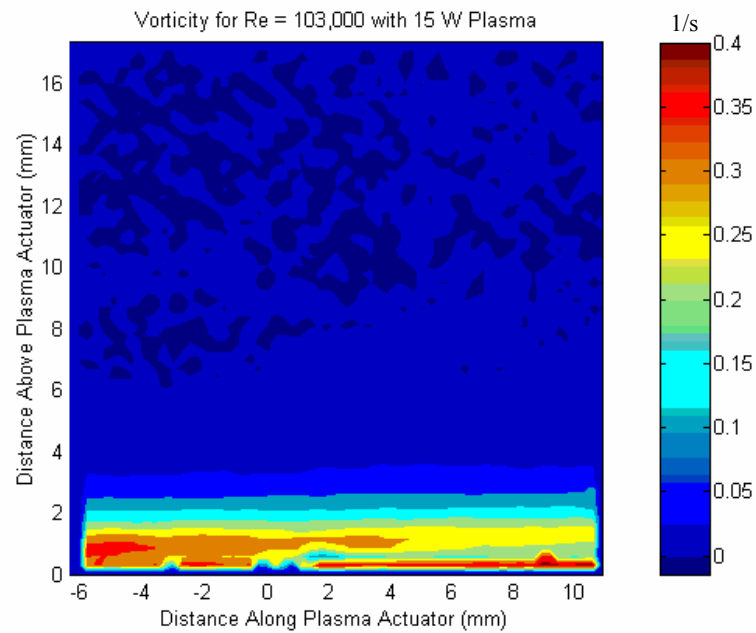


Figure 94. Contour plot of vorticity for $Re = 103,000$ with 15 W plasma.

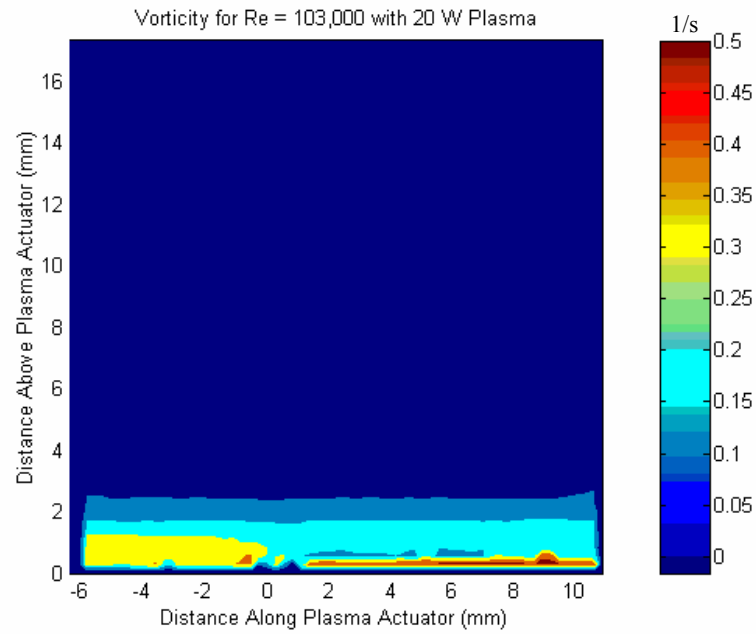


Figure 95. Contour plot of vorticity for $Re = 103,000$ with 20 W plasma.

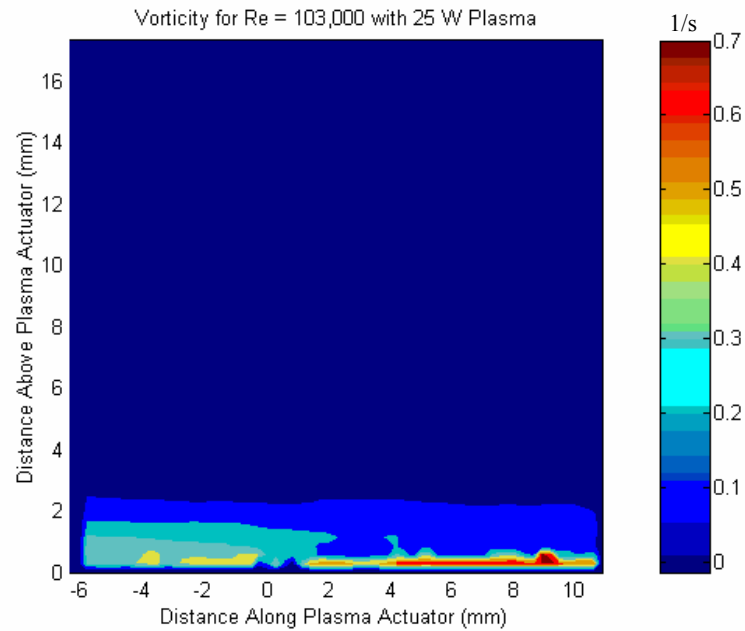


Figure 96. Contour plot of vorticity for $Re = 103,000$ with 25 W plasma.

Bibliography

1. Balcer B., "Boundary Layer Flow Control Topics Using Plasma Induced Velocity," M.S. Thesis, AFIT/GAE/ENY/05-M03, Air Force Institute of Technology (AU), Wright-Patterson AFB OH, 2005.
2. Enloe C., McLaughlin T., VanDyken R., and Fischer J., "Plasma Structure in the Aerodynamic Plasma Actuator," American Institute of Aeronautics and Astronautics, AIAA Paper 2004-0844, 2004.
3. Font G., and Morgan W., "Plasma Discharges in Atmospheric Pressure Oxygen for Boundary Layer Separation Control," American Institute of Aeronautics and Astronautics, AIAA Paper 2005-4632, 2005.
4. Hultgren L., and Ashpis D., "Demonstration of Separation Delay with Glow Discharge Plasma Actuators," American Institute of Aeronautics and Astronautics, AIAA Paper 2003-1025, 2003.
5. McLaughlin T., Munska M., Vaeth J., Dauwalter T., Goode J., and Siegel S., "Plasma-Based Actuators for Cylinder Wake Vortex Control," American Institute of Aeronautics and Astronautics, AIAA Paper 2004-2129, 2004.
6. Post M., and Corke T., "Flow Control with Single Dielectric Barrier Plasma Actuators," American Institute of Aeronautics and Astronautics, AIAA Paper 2005-4630, 2005.
7. Post M., and Corke T., "Separation Control Using Plasma Actuators – Stationary & Oscillating Airfoils," American Institute of Aeronautics and Astronautics, AIAA Paper 2004-0841, 2004.
8. Raffel M., Willert C., and Kompenhans J., *Particle Image Velocimetry, A Practical Guide*. Germany: Springer, 1998.
9. Ramakumar K., and Jacob J., "Flow Control and Lift Enhancement Using Plasma Actuators," American Institute of Aeronautics and Astronautics, AIAA Paper 2005-4635, 2005.
10. Roth J., and Sherman D., "Boundary Layer Flow Control with a One Atmosphere Uniform Glow Discharge Surface Plasma," American Institute of Aeronautics and Astronautics, AIAA Paper 98-0328, 1998.
11. Schlichting H., and Gersten K., *Boundary Layer Theory, Eighth Revised and Enlarged Edition*. Germany: Springer, 2003.

12. Suzen Y., Huang P., and Jacob J., "Numerical Simulations of Plasma Based Flow Control Applications," American Institute of Aeronautics and Astronautics, AIAA Paper 2005-4633, 2005.
13. VanDyken R., McLaughlin T., and Enloe C., "Parametric Investigations of a Single Dielectric Barrier Plasma Actuator," American Institute of Aeronautics and Astronautics, AIAA Paper 2004-0846, 2004.
14. Volino R., and Hulgren L., "Measurements in Separated and Transitional Boundary Layers Under Low-Pressure Turbine Conditions," *Journal of Turbomachinery*, Vol. 123, 2001, pp. 189-197.

Vita

Jeffrey M. Newcamp was born in Erie, Pennsylvania. He graduated from Cathedral Preparatory High School in Erie, Pennsylvania in 2000, having also attended classes at Gannon University. Jeffrey graduated from the University of Notre Dame in 2004 with a Bachelor of Science degree in Aerospace Engineering and a commission as a second lieutenant in the United States Air Force. He earned the honors of Distinguished Graduate and a Blue Chip from the Air Force Reserve Officer Training Corps for his dedication to the ROTC program and academic distinction, respectively. In addition, he was an instructor for an advanced aviation ground school for two semesters, teaching ninety ROTC cadets, midshipmen and civilians the science of flight.

In September 2004, Lieutenant Newcamp entered the Graduate School of Engineering and Management, Air Force Institute of Technology, Wright Patterson AFB, OH. He was a direct accession to earn his Master's of Science degree in Aeronautical Engineering. His follow-on assignment was to the Air Logistics Center at Robins AFB, GA as an aeronautical engineer.

REPORT DOCUMENTATION PAGE				Form Approved OMB No. 074-0188	
<p>The public reporting burden for this collection of information is estimated to average 1 hour per response, including the time for reviewing instructions, searching existing data sources, gathering and maintaining the data needed, and completing and reviewing the collection of information. Send comments regarding this burden estimate or any other aspect of the collection of information, including suggestions for reducing this burden to Department of Defense, Washington Headquarters Services, Directorate for Information Operations and Reports (0704-0188), 1215 Jefferson Davis Highway, Suite 1204, Arlington, VA 22202-4302. Respondents should be aware that notwithstanding any other provision of law, no person shall be subject to a penalty for failing to comply with a collection of information if it does not display a currently valid OMB control number.</p> <p>PLEASE DO NOT RETURN YOUR FORM TO THE ABOVE ADDRESS.</p>					
1. REPORT DATE (DD-MM-YYYY) 13-09-2005		2. REPORT TYPE Master's Thesis		3. DATES COVERED (From – To) Mar 2005 - Sept 2005	
4. TITLE AND SUBTITLE Effects of Boundary Layer Flow Control Using Plasma Actuator Discharges				5a. CONTRACT NUMBER	
				5b. GRANT NUMBER	
				5c. PROGRAM ELEMENT NUMBER	
6. AUTHOR(S) Newcamp, Jeffrey, M., 2d Lt, USAF				5d. PROJECT NUMBER	
				5e. TASK NUMBER	
				5f. WORK UNIT NUMBER	
7. PERFORMING ORGANIZATION NAMES(S) AND ADDRESS(S) Air Force Institute of Technology Graduate School of Engineering and Management (AFIT/ENY) 2950 Hobson Way WPAFB OH 45433-7765				8. PERFORMING ORGANIZATION REPORT NUMBER AFIT/GAE/ENY/05-S05	
9. SPONSORING/MONITORING AGENCY NAME(S) AND ADDRESS(ES) Air Force Research Labs, AFRL/PRTT Attn: Dr. Richard Rivir 1950 W. 5th St. WPAFB OH 45433-7251 937-255-2744 DSN: 785-2744				10. SPONSOR/MONITOR'S ACRONYM(S)	
				11. SPONSOR/MONITOR'S REPORT NUMBER(S)	
12. DISTRIBUTION/AVAILABILITY STATEMENT APPROVED FOR PUBLIC RELEASE; DISTRIBUTION UNLIMITED.					
13. SUPPLEMENTARY NOTES					
14. ABSTRACT <p>This study addresses the usage and effects of atmospheric plasma discharges on the near wall flow conditions for a Pak-B low-pressure turbine blade. A plasma actuator was built normal to the freestream flow in a low-speed wind tunnel. The test section of the wind tunnel had a contoured upper wall geometry designed to mimic the suction side of a Pak-B turbine blade. A high frequency ac voltage source supplied three voltages in the kilovolt range at four Reynolds numbers in the experiment, between 10,000 and 103,000. The effect of the plasma on the near-wall boundary layer conditions was evaluated at each of the Reynolds numbers and each of the three voltage levels. Particle image velocimetry (PIV) was used to determine the 2D boundary layer characteristics of the flow. This research showed that the plasma discharges were able to dramatically increase the flow velocity near the wall; however, the plasma was unable to reattach an already detached boundary layer. Additionally, multiple manufacturing techniques were evaluated in an effort to make the electrodes more usable in turbine blade applications.</p>					
15. SUBJECT TERMS plasma generators, low pressure, turbine blades, glow discharges, particle image velocimetry					
16. SECURITY CLASSIFICATION OF:			17. LIMITATION OF ABSTRACT	18. NUMBER OF PAGES	19a. NAME OF RESPONSIBLE PERSON
a. REPORT	ABSTRACT	THIS PAGE			Dr. Milton Franke, AFIT/ENY
U	U	U	UU	125	19b. TELEPHONE NUMBER (Include area code) 937-255-3636 x4720